Measurements and Simulation of Drift Gas Properties for the Time Projection Chambers of the T2K Experiment and for Future Neutrino Experiments

Von der Fakultät für Mathematik, Informatik und Naturwissenschaften
der RWTH Aachen University zur Erlangung des akademischen Grades
eines Doktors der Naturwissenschaften genehmigte Dissertation

vorgelegt von

Thomas Radermacher, M.Sc. RWTH

aus Würselen

Berichter: apl.-Prof. Dr. rer. nat. Stefan Roth
Univ.-Prof. Dr. rer. nat. Alexander Schmidt

Tag der mündlichen Prüfung 30.08.2019

Zusammenfassung

Zeitprojektionskammern, TPCs, werden in der Teilchenphysik häufig eingesetzt, da sie neben ihrer Fähigkeit, verlässlich Teilchenspuren zu rekonstruieren, eine gute Auflösung des Energieverlustes von Teilchen liefern. Beides sind Vorraussetzungen für eine zuverlässige Teilchenidentifikation. Um TPCs zu entwickeln und zu bauen, ist die Kenntnis der Eigenschaften des Driftgases essentiell, weil diese die räumliche Auflösung bestimmen und die Trennung der Teilchenspuren limitieren.

In modernen Experimenten der Neutrinophysik werden TPCs als Spurdetektoren für sekundäre Teilchen verwendet, die bei den Neutrinowechselwirkungen entstehen. Bei Neutrinowechselwirkungen sind die Effekte im Innern des Atomkerns, insbesondere die Wechselwirkung der Teilchen des Endzustandes der Reaktion mit der Kernmaterie, nicht vollständig verstanden. Daher ist eine hohe Effizienz bei der Rekonstruktion des Endzustands wichtig, die eine TPC bietet. Damit werden die systematischen Unsicherheiten der Messungen in der Neutrinophysik begrenzt, die von den Endzustandswechselwirkungen dominiert sind. Aufgrund der hohen Strahlintensitäten können heutzutage auch Neutrinowechselwirkungen im Gasvolumen der TPCs untersucht werden, was bisher wegen der extrem niedrigen Wirkungsquerschnitte nicht möglich war. Hier beeinflussen die Eigenschaften des gewählten Driftgases naturgemäß die Messungen noch stärker.

Ein Teil der in dieser Arbeit gezeigten Messungen wurde mit den TPCs des Nahdetektors ND280 des T2K-Experiments, einem Long-Baseline-Neutrinoexperiment in Japan, durchgeführt. Obwohl diese TPCs urspünglich nicht entwickelt worden sind, um die Eigenschaften der Driftgase zu vermessen, gelang es in dieser Arbeit, Messungen des longitudinalen und des transversalen Diffusionskoeffizienten durchzuführen. Zusammen mit der Messung der Driftgeschwindigkeit kann die Zusammensetzung des Driftgases analysiert werden. Die Ergebnisse zeigen gute Übereinstimmung mit `MAGBOLTZ`-Simulationen für die T2K-Gasmischung bei den vorgegebenen Betriebsparametern. Sie können dazu beitragen, Simulationen für Neutrinowechselwirkungen zu verbessern.

Mit den Gasmonitorkammern, GMCs, im Labor in Aachen wurden zusätzliche Messungen durchgeführt, um Simulationen und Messungen zu vergleichen. Diese GMCs sind baugleich zu denen, die bei ND280 im Einsatz sind. Die in dieser Analyse neu etablierten Methoden für die Messungen der Diffusionskoeffizienten können genutzt werden, um diese in einem Parameterraum verschiedener Gasmischungverhältnisse in

Abhängigkeit vom reduzierten elektrischen Feld zu bestimmen. Die Messungen mit den GMCs wurden verwendet, um die `MAGBOLTZ`-Simulation zu validieren. Es ist beabsichtigt, diese in einer open-access Datenbank zur Verfügung zu stellen.
Da die longitudinale und transversale Diffusion die räumliche Auflösung und die Effizienz der Spurtrennung beeinflussen, sind deren genaue Kenntnis bei der Entwicklung von neuen Gasdetektoren hilfreich. Die eingeführten Methoden und Messungen unterstützen die Auswahl des Gasgemisches bei zukünftigen Projekten. Die Eigenschaften des Gasgemischs bestimmen die Padgröße und die Signalformung der Elektronik und sollten in Übereinstimmung mit der gewünschten Auflösung des geplanten Gasdetektors gewählt werden.

Abstract

In particle physics time projection chambers, TPCs, are commonly used due to their good track reconstruction ability and energy loss resolution, which is required for reliable particle identification. In order to design and construct a TPC, the knowledge of the drift gas properties is essential, because they define the spatial resolution and also set the limitation of track separation.

In modern neutrino physics experiments TPCs are used as tracker for secondary particles coming from neutrino interactions. In neutrino interactions the effects inside the nuclei are not fully understood, especially the interaction between final state particles of the reaction with the nuclei. As consequence, it is important to have a good efficiency for the reconstruction of the final state that a TPC can provide. This limits the systematic uncertainties of neutrino physics measurements which are dominated by the final state interaction. Nowadays, also the neutrino interactions inside the gas volume of a TPC can be studied because of high intense neutrino beams. This was not possible before due to the extremely low cross-sections. These measurements are even more sensitive to the properties of the used drift gases.

A part of the measurements presented in this thesis are done with the TPCs in the near detector ND280 of the T2K experiment, a long baseline neutrino experiment located in Japan. Although the TPCs were not originally built to measure the properties of drift gases, measurements of the longitudinal and transverse diffusion coefficients were performed. Together with the measurement of the drift velocity the composition of the gas mixture can be analyzed. The results are in good agreement with `MAGBOLTZ` simulations of the T2K gas mixture for the operating parameters. They can help to improve the simulations needed for the analysis of neutrino interactions.

Measurements were also done in gas monitoring chambers, GMCs, in the laboratory in Aachen to compare simulations and measurements. These GMCs are similar to those used at ND280. The newly established methods for the measurement of the diffusion coefficients can be used to determine them in a variable parameter of various gas mixture fractions in dependence on the reduced electric field. Measurements performed with the GMCs were used to validate the `MAGBOLTZ` simulation and it is planned to publish the results in an open-access data base.

Since longitudinal and transverse diffusion are affecting the spatial resolution and the efficiency to separate tracks from each other, an accurate knowledge of them is helpful

to develop new gaseous detectors. The established methods and measurements provide an opportunity to choose the drift gas mixture for future projects. The properties of the gas mixture prescribe the pad size and the limitations for the shaping of the electronics and should be chosen according to the desired resolution for the investigated gaseous detector.

Contents

CHAPTER 1

Long Baseline Neutrino Experiments

Neutrinos are presumably the most extraordinary particles in the Standard Model of particle physics. Since they were proposed by Wolfgang Pauli in the 1930s to describe the β^- decay their theoretical description underwent some revisions in their history.

Neutrinos are electrically neutral spin-1/2 particles and are only able to interact via weak force and gravity. In the beginning, they were assumed to be massless and since the discovery of the three generations of fermions they were supposed to occur in three different flavors. Measurements of the Z-Boson decay width confirm that there are three neutrino flavors with a mass of less than half of the Z-Boson mass [1, pp. 629-630].

Nevertheless, theories exist that a fourth generation of neutrinos could exist. These proposed sterile neutrinos would not interact via weak force but only via gravity. In addition, they can be much heavier than the other neutrinos.

Nowadays, we know from the discovery of neutrino oscillation that neutrinos are not massless. Neutrino oscillation also means that each flavour eigenstate of a neutrino is a superposition of different mass eigenstates whereas these mass eigenstates are not the same as the flavor eigenstates.

The absolute masses of the neutrinos have still not been measured, because they are less than one millionth of the mass of the lightest charged lepton, the electron. This absolute mass scale can not be measured in neutrino oscillation experiments since they are only able to measure the difference of the squared masses $\Delta m_{ij}^2 = m_i^2 - m_j^2$. However, the absolute mass of neutrinos could be measured directly, for instance by measuring the spectrum of β-decays with a high precision, which is currently attempted by the KATRIN experiment [2].

In addition, the sign of Δm_{32}^2 is unknown which leads to the problem of mass ordering, often also referred to as the mass hierarchy. Due to the sign of Δm_{32}^2, two orders

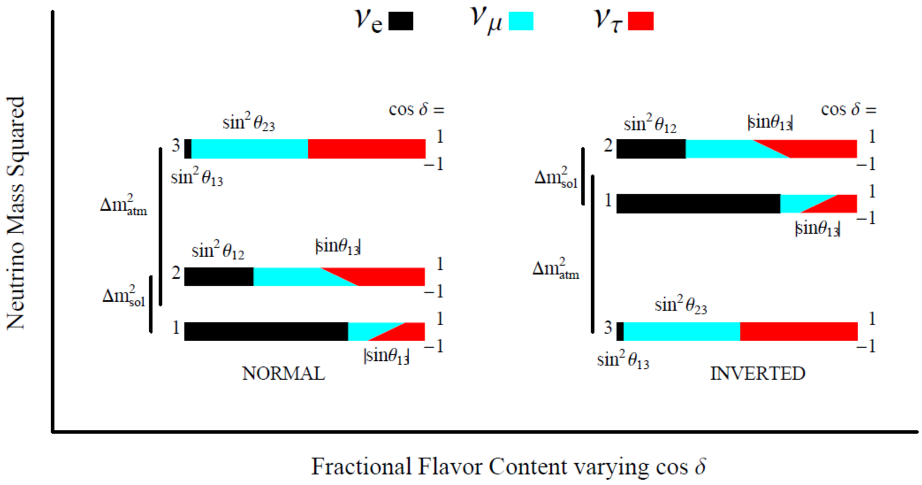

Figure 1.1.: Patterns of neutrino masses for the normal and the inverted mass hierarchy. The content of a neutrino flavour in a mass eigenstate is shown. It also depends on the value of the CP violating phase δ. [3]

are possible. In the normal hierarchy the mass eigenstate ν_1 is the lightest and the eigenstate ν_3 is the heaviest. In the inverted hierarchy the mass eigenstate ν_1 is still lighter than ν_2 but the eigenstate ν_3 is the lightest of them all. Figure 1.1 shows the patterns of the masses. In addition to the mass hierarchy the ratio of flavor contents depending on a CP-violating phase are depicted.

Introducing neutrino oscillation also provides a complex phase which could violate CP-symmetry. Recently the T2K collaboration published that a hint of favoring CP-violation is found in the data [4]. The evidence of a CP-violating phase in the mixing of neutrinos would mean that neutrinos oscillate unlike their antiparticles. This might have caused an matter-antimatter asymmetry in the forming of the universe.

Another possibility is that neutrinos are their own antiparticles. Therefore, they would be Majorana-fermions instead of Dirac-fermions. In this case two additional phases would be introduced to the neutrino oscillation.

Summarized, there are some interesting unanswered questions to be solved in neutrino physics besides determining all parameters as precisely as possible:

- Is there a *CP-violating phase* which is non-zero?
- What is the mass ordering for neutrinos? Is it *normal* or *inverted*?
- What is the *absolute mass* scale for neutrinos?
- Are neutrinos *Dirac*-fermions or rather *Majorana*-fermions?
- Do more than the three *active* neutrinos exist, e.g. *sterile* neutrinos?

All of these questions can be addressed with neutrino oscillation experiments except for the determination of the absolute mass scale. The most promising types of experiments measuring the neutrino properties in the future are long baseline neutrino experiments using either man-made accelerator or reactor neutrinos.

This thesis focuses on the accelerator neutrino experiment T2K (Tokai-to-Kamioka) and its usage of gaseous detectors.

1.1. Neutrino experiments

The detection of neutrinos is challenging for experiments, because neutrinos only interact weakly with other particles in matter. This entails the necessity of large detectors to measure a significant number of neutrino interactions. Neutrinos can interact in the detector in two ways. In a neutral current interaction, the neutrino deposits part of its energy in the detector by Z-Boson exchange and leaves the detector afterwards. Therefore, no flavor information from the through-going neutrino is gained. If the neutrino interacts via charged-current interaction, it transforms into its charged lepton partner. Hence, the neutrino needs enough energy to produce its lepton partner. By measuring the produced lepton, the flavor information is preserved.

To measure neutrino oscillation, experiments need detectors placed in a certain distance to the neutrino source, so that the neutrinos have the possibility to oscillate. In general, the measurements in these experiments can be classified in two categories:

- **Disappearance measurements:** In these measurements the number of produced neutrinos is compared to the number of detected neutrinos. The deficit which is measured gives the oscillation signal corrected for detector efficiencies. The detected neutrino type in these experiments is of the same type as the one of the produced neutrinos.

- **Appearance measurements:** Neutrinos of one type are produced and the experiment detects another type of neutrinos. The signal is the number of detected neutrinos which would not be there without oscillation.

Reactor neutrino experiments are disappearance experiments because the energy of the antineutrinos coming from reactors is too low to produce muons or tauons. The challenge is to know the flux of the neutrinos produced in nuclear reactor and the efficiency of the detector. Calculating the flux is quite challenging for nuclear reactors, therefore, experiments are designed with two detectors. The first one is positioned near the reactor in a distance where the neutrinos did not yet have the chance to oscillate. The second detector is placed further away and measures the neutrinos that had the oppertunity to oscillate. The overall flux is cancelled out from taking the ratio of both signals. In addition, systematic uncertainties of the efficiency mostly cancel out, too. One example of these experiments is the Double Chooz experiment [5].

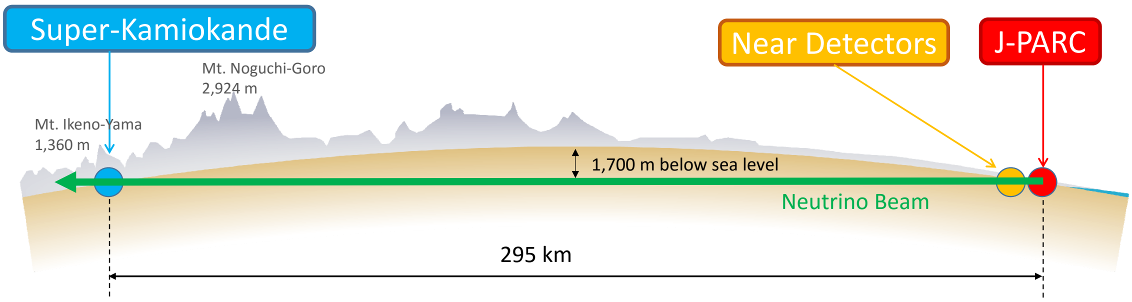

Figure 1.2.: Schematic layout of the T2K experiment. [6]

Appearance experiments benefit from the fact that a neutrino type, which was not the one that was produced at the neutrino source, is measured. For that, usually accelerator neutrinos, which create beams of muon (anti-)neutrinos with a certain energy, are being used. Unfortunately, these beams are not purely made of muon neutrinos but also contain a low fraction of electron neutrinos. For a better understanding of the neutrino beam, accelerator neutrino experiments also consist of a near and a far detector. If both detectors are similar enough, it is possible to compare the results of the near and the far detector to cancel out some systematic uncertainties on the efficiency as done in reactor neutrino experiments.

Experiments using accelerator neutrino beams are always capable of measuring muon neutrino disappearance as well. Detectors which are designed to measure electron neutrino appearance need to have the ability to distinguish between electron and muon neutrinos. Due to the muon neutrino flux measured with the near detector and the number of muon neutrinos in the far detector, the disappearance can be determined.

1.2. The T2K Experiment

The T2K (Tokai-to-Kamioka) experiment is a long baseline neutrino oscillation experiment in Japan which was mainly designed to measure the mixing angle Θ_{13} via electron neutrino appearance. Precision measurements of Δm^2_{23} and $\sin^2(2\Theta_{23})$ are also performed by measuring the muon neutrino disappearance.

T2K uses Super-Kamiokande as a far detector which is located 295 km from the accelerator at J-PARC in Tokai, Japan. The experiment also consists of a near detector complex with an on-axis and an off-axis detector in 280 m distance to the beam target. A schematic view of the T2K experiment is shown in figure 1.2.

T2K makes use of the off-axis method in which the neutrino beam is directed at an angle with respect to the far detector. This off-axis angle is 2.5° and the beam towards the far detector has a peak energy of 600 MeV. This method has the advantage of generating a narrow energy band of the muon neutrinos and also reducing the background of electron neutrino contamination in the beam.

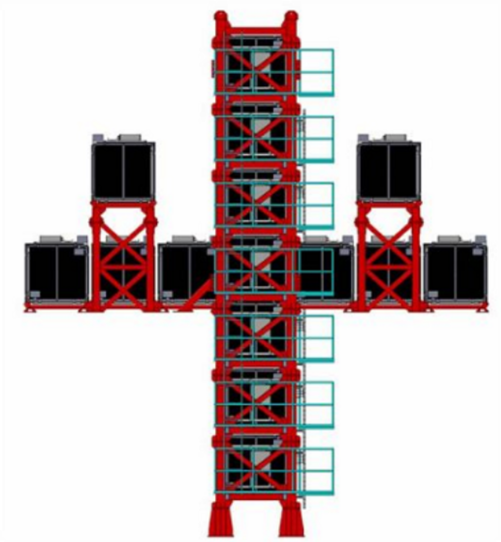

Figure 1.3.: The INGRID on-axis detector. [6]

The beam is produced at the Japan Proton Accelerator Research Complex, J-PARC [7], by protons, which were accelerated in a synchrotron to 30 GeV, impinging on a graphite target. The thereby produced secondary pions are focussed by magnetic horns and decay into neutrinos. Depending on the sign of the current in the magnetic horns a muon or antimuon neutrino beam is produced.
The far detector, Super-Kamiokande is located in the Mozumi mine under the peak of Mount Ikenoyama, in the prefecture Gifu, Japan. Super-Kamiokande is a water Cherenkov detector filled with 50 kt of pure water in a stainless steel tank with a diameter of 39 m and a height of 42 m. The detector consists of 13, 000 photo multiplier tubes to detect the Cherenkov light of secondary particles produced by neutrino interactions.
The near detector complex, which is located 280 m from the target, consists of two detectors. The on-axis detector INGRID is built to monitor the neutrino beam direction and intensity. It is composed of 14 identical modules arranged in a cross as shown in figure 1.3. Two additional modules are positioned outside of this cross. All modules are built in a sandwich structure of iron plates and scintillators that are read out by SiPMs.
The off-axis near detector ND280 is constructed from several subdetectors to characterize the signals and backgrounds for the far detector. It serves to measure the muon neutrino flux and energy spectrum of the beam as well as the electron neutrino contamination. In addition it measures rates for exclusive neutrino reactions and needs to be capable of distinguishing between event types like charged current quasi-elastic, charged current inelastic and neutral current events.
Figure 1.4 shows an exploded view of the ND280 off-axis detector. The detector is built inside the former UA1/NOMAD magnet which provides a magnetic field of 0.2 T

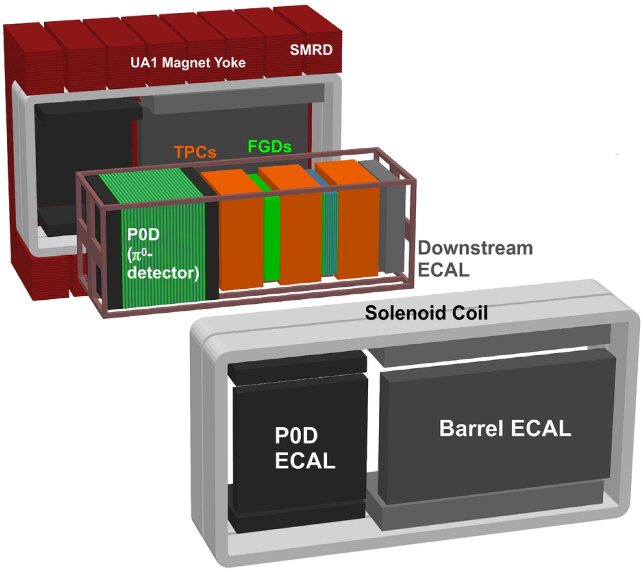

Figure 1.4.: An exploded view of the ND280 off-axis detector. [6]

in order to measure the momenta of the secondary charged particles with a good resolution and also determine the sign of the charged particles. Inside of the magnet the neutrinos first reach the Pi-Zero detector P0D which measures the neutral current interaction $\nu_\mu + N \rightarrow \nu_\mu + N + \pi^0 + X$ on a water target. Therefore, bags of water are interleaved between bars of scintillators in the x- and y-plane perpendicular to the beam direction. These bars are read out by wavelength shifting fibres, WLS, and SiPMs.

Downstream of the P0D, the tracker detectors follow. These consist of three time projection chambers, TPCs, and two fine grained detectors, FGDs. The FGDs are not only used for tracking, but also provide a target mass for neutrino interactions. They are again constructed from scintillator-bars perpendicular to the neutrino beam in x- and y-direction, which are read out by fibres and SiPMs. These scintillator-bars are arranged in layers. The first FGD uses the scintillator as neutrino target mass. The second FGD is water enriched and uses bars of plastic scintillators and layers of water as neutrino target.

Both FGDs are surrounded by the TPCs. They are not only used for tracking the particles and determine their momenta in the magnetic field. They are also capable of distinguishing between particle types by combining the momenta and the amount of ionization the particles left in the detector. Each of the three TPCs has a central cathode and a field cage made from copper strips which provide the electric field. The readout of the TPC is made of bulk MicroMeGaS. A more detailed description of the TPCs follows in chapter 2.3.1, because some of the analyses in this thesis are performed with them.

Surrounding the inner detectors - P0D, FGDs and TPCs - the sampling electromagnetic calorimeters, ECals, are placed. They consist of plastic scintillators as active material

and lead absorbers. They complement the event reconstruction by measuring the energy and direction of all particles and photons leaving the inner detectors.
Inside of the return yoke of the magnet, the Side Muon Range detector, SMRD, is located, which measures muons escaping the detector with high angles as well as identifies background caused by cosmic rays and events, that are happening in the surrounding cavern of the detector. The active materials again are scintillator modules which are placed within the air gaps of the return yoke.
The T2K collaboration has about 500 members from 63 institutes in 11 countries [8]. A detailed description of the T2K experiment can be found in [6]. Further information is available on the experiment website [8].

1.2.1. T2K extension: T2K phase II

The T2K collaboration proposed to extend the currently approved running of $7.8 \cdot 10^{21}$ POT (protons-on-target) to $20 \cdot 10^{21}$ POT, because recent T2K measurements indicate that CP-violation in the neutrino mixing could be observed in the future [9]. With a higher number of protons-on-target a first observation of CP-violation with a sensitivity of $3\,\sigma$ or higher in case of maximum CP-violation would be possible.
The extension, here referred to as T2K-II, also aims to reach better precision on the measurements of Θ_{23} and Δm^2_{32} of at least 1.7° and 1 %, respectively.
T2K-II starts subsequently to the currently approved T2K running and should be finished before the operation of the next generation long baseline neutrino oscillation experiments, which are expected to start in 2026.
For the extension, T2K plans to upgrade the near detector ND280. To meet the requirements of the proposal, the upgrade of the near detector should contain a full and precisely known polar acceptance for muons, which are created in the charge current neutrino interaction with the same performance in momentum resolution and charge deposition as by the current ND280 detector. Also, it should have a fiducial mass of at least a few tons and a high efficiency in tracking low energetic pions and protons covering the full solid angle. In addition, a good $T0$ determination in the order of 0.5 ns is required to distinguish between backward and forward going tracks. [10]
The proposed upgrade contains a new design shown in figure 1.5, where the old three TPCs and two FGDs are kept. The P0D detector will be removed and replaced by a highly granulated scintillator detector, Super-FGD, and two new time projection chambers, HA-TPC, surrounded by additional time-of-flight detectors, TOF.
The Super-FGD consists of small scintillating cubes, each read out by three WLS fibres. It will serve as target for the neutrino interactions and will have a high acceptance for reconstructing the vertices. The scintillating cubes will have a size of $1\,\text{cm}^3$.
This Super-FGD will be sandwiched between two new TPCs. Substantially, these high angular TPCs will perform similar to the old TPCs but will have a better spatial resolution. In addition, the readout will be changed to resistive bulk MicroMeGaS and the dead area reduced by removing the CO_2 isolation gap and insulating the field cage with an insulator laminated on a composite material.

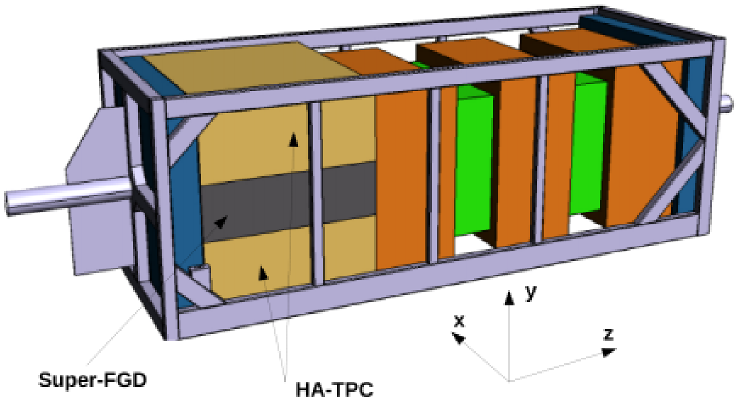

Figure 1.5.: CAD-3D model of the construction design of the ND280 upgrade with the new Super-FGD and the two new HA-TPCs. [11]

The TOF detector will be built out of thin scintillating bars which surround the cube composed of Super-FGD and TPCs. The timing resolution aimed for with this detector is in the order of 100 ps.
More details on the construction of the ND280 upgrade can be found in the technical design report [11].

1.3. Future Experiments

The roadmap of long baseline neutrino experiments focusses on two next-generation experiments. Both are operating with a higher beam power than current accelerator neutrino experiments and are planned to have large detectors. The two experiments are T2HK, which uses the same baseline as T2K but with the proposed Hyper-Kamiokande detector, and DUNE, which is provided by a beam from Fermilab and a far detector at the Sanford Underground Research Facility.

1.3.1. T2HK

The Hyper-Kamiokande detector will consist of a cylindrical tank of 60 m height and a diameter of 74 m which will be filled with 260 kT of pure water. This water Cherenkov detector is proposed to be built in the Kamioka mine in the Gifu prefecture in Japan near to its predecessor Super-Kamiokande. The detector will be operated with a 50 %

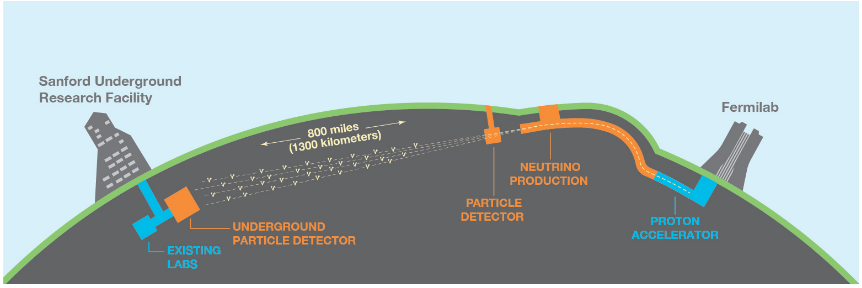

Figure 1.6.: Schematic view of the DUNE experiment. [12]

higher photodetection efficiency than Super-Kamiokande with 40, 000 ultra-sensitive photosensors. The construction of Hyper-Kamiokande is planned to start in 2020.
Hyper-Kamiokande with its higher sensitivity to detect neutrinos is planned to measure CP-violation with the (anti-)neutrino beam from J-PARC, currently used by the T2K experiment. By the time Hyper-Kamiokande will start operating, the beam power will be increased to 750 kW, making the discovery of CP-violation possible with a significance of $3\,\sigma$.
By now, a design for a near detector has not yet been decided on, but given the experience of the T2K experiment, another upgrade of the current ND280 using TPCs is possible.

1.3.2. DUNE

The Deep Underground Neutrino Experiment, DUNE, is a planned neutrino experiment in the United States of America. It will use a neutrino beam produced at Fermi National Accelerator Laboratory in Batavia, Illinois. The far detectors will be installed in the Sanford Underground Research Laboratory, SURF, in Lead, South Dakota, which is 1300 km away from the neutrino source. Four far detectors, which are all liquid argon Time Projection Chambers with combined 68 kt of liquid argon, are planned. A schematic view of the experiment is shown in figure 1.6. [12]
The basic physics program of DUNE is equal to the program of Hyper-Kamiokande. DUNE will be able to measure electron neutrino appearance as well as muon neutrino disappearance. The measurement of CP-violation and the determination of the mass hierarchy are the main goals of the experiment.
The design of the near detector is not yet fixed, but it will be placed a few hundreds of meters downstream of the target where the neutrinos are produced. Some of the proposed designs for the near detector are using gaseous time projection chambers, for example high-pressure time projection chambers, which would be operated with an overpressure of $5 - 10$ bar. These high-pressure TPCs are gaining from their high masses in order to have a higher interaction rate but also have a good track reconstruction ability like TPCs operating at atmospheric pressure.

Chapter 2

Gas based Detectors and Neutrino Detection

Time projection chambers, TPCs, are a reliable class of gaseous particle detectors. Their technology has several advantages compared to other detectors.

TPCs can be built with large volumes while using just small amounts of material, because the gas itself is the active medium to detect particles. The signal which is generated by the traversing particles via ionization can be detected with moderately sensitive amplifiers, because it is amplified by gas amplification with high electric fields. The measurement of ionization along the track also yields the energy loss of the particles. If this energy loss measurement is combined with a momentum measurement by putting a TPC in a magnetic field, particle identification is possible as well. In addition, good track reconstruction is possible using just a few channels.

In sum, TPCs are a good choice for tracking detectors with the additional possibility of particle identification.

To built such a TPC a good understanding of the drift properties of gas mixtures is needed.

2.1. Transport of electrons in gases

To understand the technology of gas detectors a profound knowledge about the motion of electrons in gases is necessary, starting from the ionization process and the drift of the ionization electrons towards the anode to the amplification by high electric fields in the detection area and signal generation. This section presents a short overview of the important processes. It losely follows [13] where a comprehensive discussion can be found.

2.1.1. Ionization in gases

When a charged particle traverses gas, it loses energy along its trajectory by interacting with the gas molecules. Depending on the particles energy, different processes contribute to the energy loss. If the energy is high enough, the gas atoms along its path are ionized. Typically a few keV/cm are needed. Generally a distinction is made between primary and secondary ionization.

Primary ionization happens, if a gas molecule A is directly ionized by a traversing particle $\mathrm{P}^{\pm}$. Thus one or more electrons can be ejected. The possible reactions are

$$\begin{aligned} &\mathrm{P^{\pm}A} \rightarrow \mathrm{P^{\pm}A^{+}e^{-}}, \\ &\mathrm{P^{\pm}A} \rightarrow \mathrm{P^{\pm}A^{++}e^{-}e^{-}}, \dots \end{aligned} \tag{2.1}$$

When the gas molecule is not directly ionized by the traversing particle but by an ionization electron or through an intermediate excited state A^*, it is called secondary ionization. The reactions with an ionization electron are

$$\begin{aligned} &\mathrm{e^{-}A} \rightarrow \mathrm{e^{-}A^{+}e^{-}} \\ &\mathrm{e^{-}A} \rightarrow \mathrm{e^{-}A^{++}e^{-}e^{-}}, \dots \end{aligned} \tag{2.2}$$

In case of an excited state the ionization happens through interaction with another gas molecule B as shown in the reaction 2.3.

$$\mathrm{A^{*}B} \rightarrow \mathrm{AB^{+}e^{-}}. \tag{2.3}$$

If the energy transfer happens by collision, it is called Penning effect and if it happens by photon exchange, Jesse effect. Most of the ionization electrons are produced via secondary ionization.

The energy loss by ionization is just a fraction of all energy lost. The total energy loss is connected to the energy spent in ionization by the energy W, which is the energy needed on average to create an electron in a certain gas mixture. The energy W is defined as

$$W = \left\langle \frac{\mathrm{d}E}{\mathrm{d}x} \right\rangle \frac{L}{\langle N \rangle} \tag{2.4}$$

by the average total energy loss per length $\langle \mathrm{d}E/\mathrm{d}x \rangle$, the average number of electrons $\langle N \rangle$ and the length of the trajectory L. It depends on the type of traversing particle, the particle's initial energy and the gas mixture. Above a few keV for electrons or a few MeV for α-particles the dependence on the initial energy vanishes.

With the knowledge of the energy W, it is possible to reconstruct the total energy loss of a particle. Today, this energy has been measured for a huge number of applied gas mixtures and can also be simulated. Typical values for W are between 20 eV and 50 eV.

2.1.2. Drift of ionization electrons

When an electric field is applied to the gas volume, the electrons and ions drift towards the electrodes according to the electric field lines. The electrons on their way to the anode collide with the gas molecules. They scatter isotropically with an instantaneous microscopic velocity v_{inst} due to the large mass difference between electrons and the gas molecules. Between the collisions the electrons are accelerated by the electric field. Every collision stops the acceleration and the direction of the electron is randomized. Over time, this macroscopic velocity of the electrons and the energy ϵ is in equilibrium. This drift velocity is depending on the exponentially distributed mean time τ between two collisions as depicted in

$$v_d = \frac{\langle 1/2 \cdot at^2 \rangle}{\langle t \rangle} = \frac{1}{2} a \frac{\langle t^2 \rangle}{\langle t \rangle} = \frac{1}{2} a \frac{2\tau^2}{\tau} = \frac{eE}{m_e}\tau. \tag{2.5}$$

The mean time between the collisions is depending on v_{inst}, the number density of the gas molecules n and the cross-section of the scattering process σ_{scat} as described in

$$\tau = \frac{1}{v_{inst} n \sigma_{scat}}. \tag{2.6}$$

The energy ϵ, which is derived from the acceleration, must on average be lost in the next collision. This introduces the average fractional energy loss per collision λ.

$$eE\Delta z = \epsilon\lambda \frac{\Delta z}{v_d \tau} \tag{2.7}$$

shows that the energy loss is equal to the energy from the acceleration of a drifting electron over a distance Δz. The energy can be described by a function of the microscopic velocity v_{inst} given as

$$\epsilon = \frac{1}{2} m_e v_{inst}^2. \tag{2.8}$$

The macroscopic drift velocity can be expressed as function of E, n, λ and σ_{scat} as shown in

$$v_d^2 = \frac{e}{m_e \sigma_{scat}} \sqrt{\frac{\lambda}{2}} \cdot \frac{E}{n}. \tag{2.9}$$

This is achieved by the combination of equation 2.5 to 2.8. This expression can be simplified by the introduction of the electron mobility μ. Thereby, μ is defined as ratio of the drift velocity to the fraction of electric field and gas density E/n. The simplification results in

$$\vec{v}_d = \sqrt{\frac{e}{m_e \sigma_{scat}} \sqrt{\frac{\lambda}{2} \frac{n}{E}}} \cdot \frac{\vec{E}}{n} = \mu \cdot \frac{\vec{E}}{n}. \tag{2.10}$$

The gas density depends on temperature and pressure and can be assumed as proportional to $n \propto p/T$. Followed by the fact that the electric field only occurs in fractions of E/n, it is possible to compensate temperature and pressure changes by adjusting the electric field. In this thesis, the drift velocity is always given as a function of the reduced electric field ET/p.

2.1.3. Electron diffusion

The electrons can be considered as a point-like cloud when they start to drift. On their way towards the anode, they scatter due to collisions with the gas molecules and so the electron cloud diffuses. The origin of the cloud can be assumed to travel with the average drift velocity as in equation 2.10, while the velocity of the individual electrons deviates. In the simplest assumption this cloud can be considered isotropic in all directions with a gaussian distribution

$$n_e = \left(\frac{1}{\sqrt{4\pi D t}}\right)^3 \exp\left(\frac{-r^2}{4Dt}\right). \tag{2.11}$$

The cloud is starting point-like at $t = 0$ with the radius $r^2 = x^2 + y^2 + (z - v_d t)^2$ and travels with v_d in the z-direction. D is the diffusion constant. The electron current is $\vec{\Gamma} = n_e \vec{v_d} - D\vec{\nabla} n_e$ and is conserved. Thus, the electron number density n_e satisfies the continuity equation

$$\frac{\partial n_e}{\partial t} + \vec{\nabla} \cdot \vec{\Gamma} = 0. \tag{2.12}$$

The mean squared deviation of the charge from its center is $\sigma_r^2 = 2Dt$. This deviation can thus be interpreted as the width of the electron cloud. Further calculations show that the diffusion constant is depending on the microscopic velocity and the mean time between the collision τ and thereby, using equation 2.6, is depending on the gas density n as shown in

$$D = \frac{1}{3} v_{inst}^2 \tau = \frac{v_{inst}}{3n\sigma_{scat}}. \tag{2.13}$$

In this thesis, a different definition for the diffusion coefficient is used. The defined coefficient shows the dependence of the cloud width from the travelled distance according to

$$\sigma_r = \sqrt{\frac{2D}{v_d}} \sqrt{\Delta z} = d\sqrt{\Delta z}. \tag{2.14}$$

In this definition, the diffusion coefficient is a function of v_d and thus a function of the reduced electric field ET/p. In addition, the diffusion coefficient depends directly on the density, which makes it necessary to scale the diffusion coefficient with the gas density for comparisons.

In general, the diffusion is non-isotropic. Therefore, it is distinguished between the diffusion in the direction of motion, the longitudinal diffusion, and the diffusion perpendicular to the moving direction, the transverse diffusion. This changes the density distribution of equation 2.11 to the anisotropic case

$$n_e = \frac{1}{\sqrt{4\pi D_L t}} \left(\frac{1}{\sqrt{4\pi D_T t}}\right)^2 \exp\left(-\frac{x^2 + y^2}{4D_T t} - \frac{(z - v_d t)^2}{4D_L t}\right), \tag{2.15}$$

with the cloud moving in the z-direction. As a consequence, the width of the electron cloud is $\sigma_l = \sqrt{2D_L/v_d}\sqrt{\Delta z} = d_l\sqrt{\Delta z}$ in the longitudinal dimension and $\sigma_t = \sqrt{2D_T/v_d}\sqrt{\Delta z} = d_t\sqrt{\Delta z}$ in the transverse dimension.

2.1.4. Gas amplification

The amount of ionization electrons, that reach the anode, is usually too small to create a sufficient signal. Therefore, high electric fields near the anode are used to create more ionizing particles to amplify the signal. In higher fields the electrons are further accelerated gaining more energy to create new ionizations. The newly created electrons again create even more ionization particles what leads to an ionization cascade. This exponential amplification process can be described by the first Townsend coefficient α_T, which describes the number of ionizations N_{ion} by a single electron per unit length. The increase of the number of electrons for a length Δz is given by

$$dN = N_{ion} \alpha_T \Delta z \tag{2.16}$$

On the one hand, the ionization rate depends on the reduced electric field E/n from the ionization cross-section and on the other hand, it is directly proportional to the gas density n itself. Mathematically α_T can be expressed as

$$\alpha_T(E/n, n) = \left\langle \frac{N_{ion}}{\Delta z} \right\rangle = f(E/n) \cdot n. \tag{2.17}$$

The amplification factor can be determined by integrating equation 2.16 along the drift length. Usually this factor is called gain and is the ratio of the number of ionization electrons before and after the avalanche process in the gas. The gain is defined as

$$G = \frac{N_{ion}}{N_{ion,0}} = \exp\left(\int_{z_1}^{z_2} \alpha_T(E/n, n) dz \right). \tag{2.18}$$

Hence, α_T depends on different effects of ionization and can in general not be calculated directly. Even though the cross-sections for primary ionization are known properly, the cross-sections for Jesse and Penning effect are not sufficiently known. In practice, the gain needs to be measured for gas mixtures.

2.1.5. Influence of a magnetic field

If, in additional a magnetic field is applied to the drift volume, the drift direction is usually not parallel to the electric field anymore, because the electrons are influenced by Lorentz forces. In general, this can be taken into account by considering the scalar electron mobility from equation 2.10 as a tensor $\boldsymbol{\mu}$ with the angle ϕ between the magnetic and electric field vector, which results in

$$\vec{v_d} = \boldsymbol{\mu}(E/n, B/n, \phi) \frac{\vec{E}}{n} \tag{2.19}$$

From [13, eq. 2.9, p. 51] the magnitude of the drift velocity in the direction of the electric field vector changes according to

$$\frac{v_d(\omega)}{v_d(0)} = \frac{1 + \omega^2 \tau^2 \cos(\phi)}{1 + \omega^2 \tau^2}. \tag{2.20}$$

At that, $\omega = e/m \cdot B$ is the cyclotron frequency.
In the same way the diffusion constant can be treated as a tensor by which the mean squared deviation in the direction of an arbitrary unit vector $\vec{e}$ is as

$$\sigma_e^2 = 2\vec{e}\boldsymbol{D}(E/n, B/n, \phi)\vec{e}t. \tag{2.21}$$

In this thesis generally only field configurations, where electric and magnetic fields are parallel to each other, are considered. In this special case, the drift direction is still in the direction of the electric field vector. Equation 2.20 with $\phi = 0$ also yields that the drift velocity has both the same magnitude with and without a magnetic field.
In addition, the longitudinal diffusion coefficient is not changing. Only the transverse diffusion coefficient is changing according to

$$\frac{D_T(\omega)}{D_T(0)} = \frac{d_t^2(\omega)}{d_t^2(0)} = \frac{1}{1+\omega^2\tau^2}. \tag{2.22}$$

2.2. Drift gas mixtures

For the operation of a gaseous detector, especially for time projection chambers, gas mixtures are used. In many cases, they are consisting of a high fraction of a noble gas and an admixture of quencher gases. The choice of the gas mixture however is always contingent on the requirements of the gaseous detector. Critical is the stability of the gas amplification process and the mean lifetime of the free electron. The lifetime has to be large enough for the ionization electrons to survive until a signal can be produced by reaching the anode.
Noble gases provide a good choice as counting gas, because they have a limited number of transitions and no vibration or rotation states. They are fairly easy to ionize and also, they are chemically low reactive. The disadvantage is, that in the process of gas amplification many UV-photons are produced, which can not be stopped easily with the noble gas. These photons can amplify the avalanche uncontrollably. Therefore, quenching gases are mixed with the noble gases. These quenching gases are most often organic molecular gases. They have the advantage of a high probability of absorbing photons due to their high number of radiation-free rotation and vibration transitions.
More important for the choice of the gas mixture is the dependence of its drift velocity on the reduced electric field. It is preferential, that it varies only a little by deviations in ET/p. Thus, a stable performance is feasible under fluctuations in temperature and pressure as well as smaller field gradients. Typically, working points for drift chambers are defined at an extremum of the drift velocity curve. Usually this is the maximum drift velocity. Otherwise careful calibrations are necessary.
The gas mixture also sets the limitations for the spatial resolution and thus the choice of the readout segmentation which is depending on the diffusion coefficients. Compromises have to be made to keep the diffusion as low as possible such that good separation of nearby tracks can be achieved. If the longitudinal diffusion coefficient

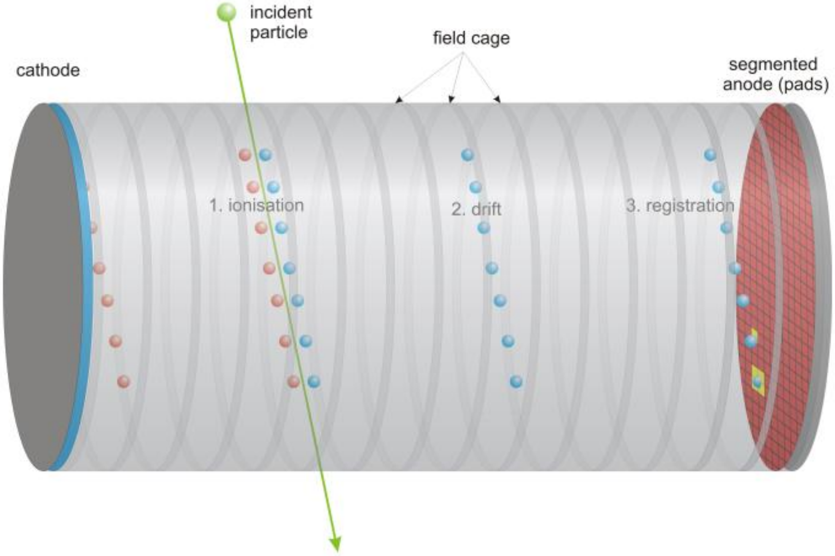

Figure 2.1.: Working principle of Time Projection Chambers. [16]

is too large, tracks drifting behind each other merge together and will be detected as only one smeared large electron cloud at the readout plane. Transverse diffusion limits the separation of two tracks perpendicular to the drift direction. On the other hand, the transverse diffusion needs to be large enough to spread the electrons over several readout segments to achieve a better resolution for the track reconstruction.

2.3. Time Projection Chambers

A Time Projection Chamber, TPC, is composed of a gas-filled detection volume inside a homogeneous electric field. It provides a complete, three-dimensional reconstruction of ionization tracks that take place in the gas.

Typically the gas-filled volume is divided in two halves by a central high-voltage cathode. The anode endplates are in general segmented and originally equipped with multi-wire proportional chambers. Nowadays also MicroMeGaS (Micro-MEsh GAseous Structure [14]) and GEM (Gas Electron Multiplier [15]) are used to read out the signal of the ionization electrons. Figure 2.1 shows the basic working principle of a TPC.

When the gas is ionized, the ionization electrons are drifting towards the anode according to the applied electric field. Because of the segmentation of the anode, two dimensions are reconstructed. Since the electric field is homogeneous, the electrons drift with a constant drift velocity and so, the third coordinate can be reconstructed by the time of the electron drift. Therefore, typically timing informations for the track from outer detectors are needed. Only needing the readout on the endplates, a TPC can be operated with just a few channels as opposed to other detector types, for example silicon trackers.

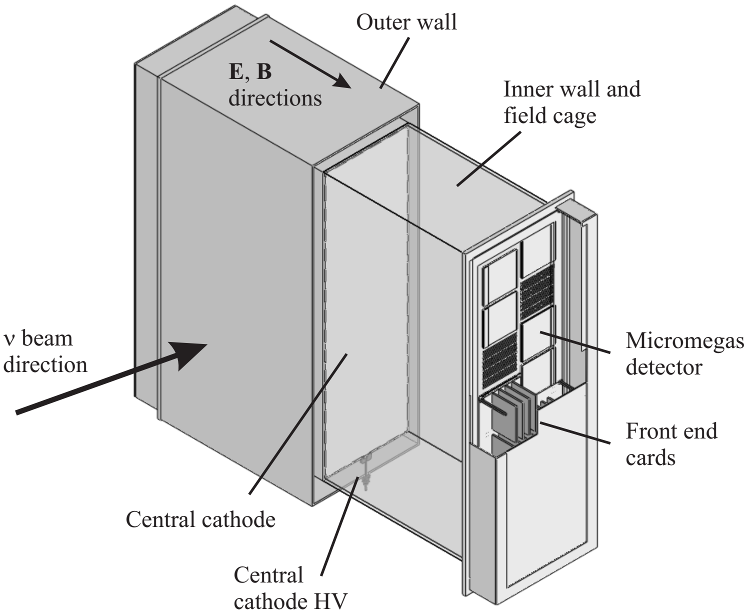

Figure 2.2.: Design sketch for a TPC for the ND280 detector. [17]

If an additional magnetic field is applied to the TPC parallel to the electric field, it is possible to improve the spatial resolution in the anode plane, because the transverse diffusion is minimized. In addition, it is thus possible to reconstruct the particle momentum. With the measurement of the collected charge, the energy loss dE/dx can be determined and, therefore, particle identification can be done by measuring dE/dx for a given particle momentum.

2.3.1. ND280-TPCs

In this thesis the TPCs of the ND280 near detector of the T2K experiment are used for analysing gas properties. Three TPCs are installed in ND280 and are used as trackers together with the two FGDs.

Each of the identically constructed TPCs has an active rectangular volume of $1808 \times 2230 \times 854\,\mathrm{mm}^3$, where the z-coordinate is in the direction of the neutrino beam. This volume is separated in two halves by a central cathode and each readout side has a maximal drift length of $l_{\text{drift, max}} = 897\,\mathrm{mm}$ excluding parts of the volume where the electric field is insufficiently uniform. The active volume is located in an outer gas-filled box which is filled with CO_2 to provide electrical insulation. The applied drift gas in the inner volume is a mixture of argon (Ar), tetrafluoromethane (CF_4) and isobutane (iC_4H_{10}) and is mixed in volume fractions of 95:3:2, respectively. This gas mixture is further referred to as T2K gas mixture. A sketch of one TPC is shown in figure 2.2.

The applied electric field is approximately $275\,\mathrm{V/cm}$ and the magnetic field supplied by the reused UA1 magnet is adjusted to $0.2\,\mathrm{T}$.

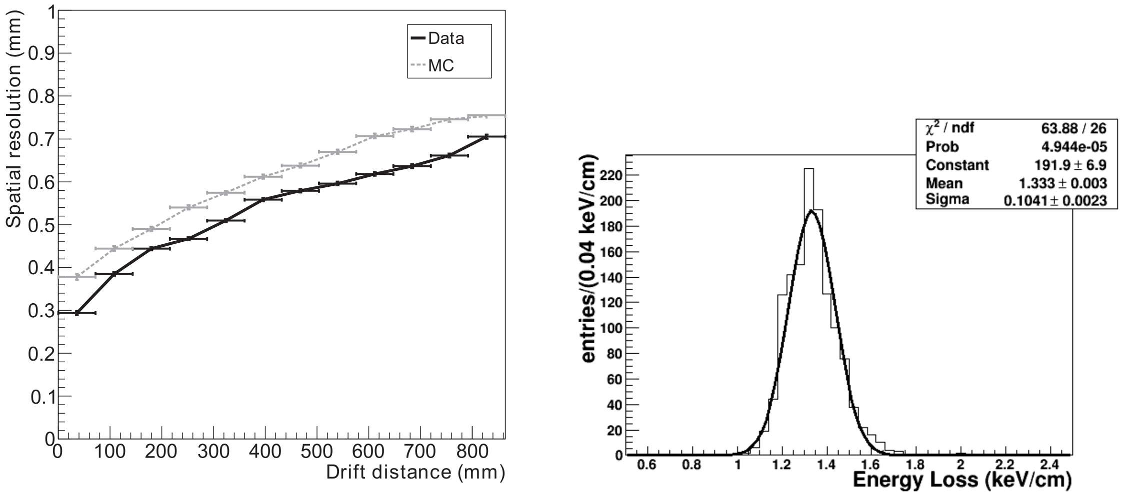

Figure 2.3.: Performance of the TPCs in the ND280 detector. On the left side the spatial resolution as function of the drift distance of clusters of two detector pads is shown. On the right side the energy loss for negatively charged particles with momenta between 400 MeV/c and 500 MeV/c is shown. [17]

The endplates are composed of bulk MicroMeGaS, which are read out by the AFTER-chip [18]. This ASIC-based readout-chip was designed to match the requirements of these TPCs. Each detection surface is equipped with twelve bulk MicroMeGaS modules that consist of 1728 pads in 48 rows of 36 pads each. One module has a size of $36 \times 34\,\mathrm{cm}^2$. The pads have a rectangular shape with an effective size of $9.8 \times 7.0\,\mathrm{mm}^2$. The amplification voltage for every MicroMeGaS is 350 V.

The TPCs are operated since 2009 and perform within their specifications. The required spatial resolution of at least 0.7 mm within reconstructed clusters of at least 2 detector pads is shown in figure 2.3 on left side. On the right side of figure 2.3 the energy loss for minimum ionization particles is shown. The resolution is $7.8 \pm 0.2\,\%$ and is less than its requirement of 10 %.

The coordinate system used in this thesis for the analysis of TPC data is orientated to have the z-axis in beam direction and the x-axis parallel to the drift direction of the electrons in the TPCs.

All details are referring to [17] where a detailed description is given about the TPCs in the ND280 detector.

2.3.2. Gas Monitoring Chambers

The Gas Monitoring Chambers, GMCs, are built to monitor the drift velocity and the relative gain in the gas system of the TPCs inside ND280. They are built as mini-TPCs and have a field cage of a length of $l = 14.8\,\mathrm{cm}$. The field cage consists of copper strips on a Kapton foil that are connected with SMD resistors. Electric fields of up to 350 V/cm can be achieved.

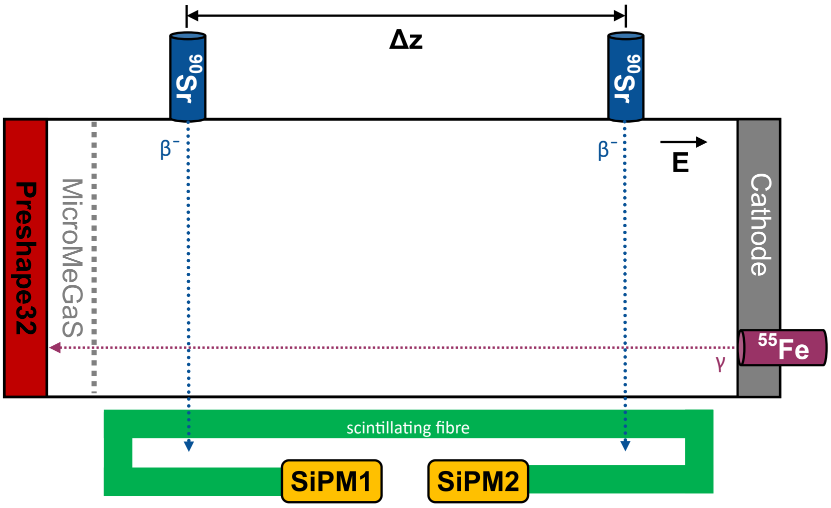

Figure 2.4.: Schematic view of the gas monitoring chamber. Two tracks can be created by the strontium-90 sources with a certain distance from each other to measure the drift velocity. By means of the well-known energy deposition of the iron-55 source, a relative gain can be determined.

A schematic view of the GMC is shown in figure 2.4. At the top side of the chambers two slits are present with a distance of $\Delta z = 12.1\,\text{cm}$ where β^--sources are placed to measure the drift velocity. Usually strontium-90 sources are used. At the bottom side parallel to the slits, scintillating fibres that are read out by two SiPMs, are located. They are used as trigger system. At the cathode side of the chamber, another slit is available to place an iron-55 source to measure the relative gain of the supplied gas. A γ-source is used, because its primary ionization is point-like. In addition, γ-particles emitted from the source have discrete energies which lead to a similar primary ionization in the gas.

The anode is built out of a MicroMeGaS similar to those used in the TPCs of the ND280 detector. The pad structure consists of square pads with a pitch of 5 mm and is arranged in four rows of 14 pads. A sketch of the pad structure with the applied connections of pads for the measurements is shown in figure 2.5.

To measure the drift velocity, four pads in each row (1 to 4), which are perpendicular to the direction of the β-electrons from the strontium-90 source, are connected. The drift velocity is measured by the drift time difference of both β-electron tracks. The measurement is triggered by the trigger system and the stop signal is given by the electrons reaching the anode.

On the other side of the MicroMeGaS the gain is measured. For that, four pads are connected in a quad (5) which is surrounded by a ring of pads as veto region (6). To

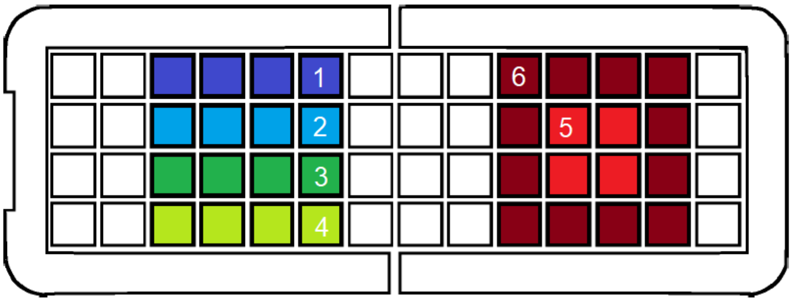

Figure 2.5.: Configuration of the MicroMeGaS pad structure. Modified from [19].

measure the gain, the signal on the connected quad pads is integrated, in case no signal on the veto ring occurs. From the distribution the mean value is then determined by a fit.

2.4. Neutrino Gas Interaction

Nowadays, neutrino oscillation experiments reach a phase, where they are not limited primarily by statistics. Systematic uncertainties on the neutrino-nucleus interactions play an increasing role in the precision of the measurements. The investigated interactions often rely on cross-section measurements of former experiments or have to be measured within the experiment itself, as T2K does with its near detector ND280.

Originally, these cross-section measurements with ND280 were done using reactions in the solid state detectors (FGD, PØD) and the TPCs were only used for particle identification and the momentum measurement of the final state particles. There is a high threshold for the particles originating from the vertex. For example protons in the FGD need to have a minimal momentum of least 450 MeV/c.

Alternatively, the TPCs can be used as detection volume, which means the neutrino interaction takes place in the gas of one TPC. The detection threshold for the TPC is significantly lower compared to solid state detectors due to its lower density and higher granularity. The drawback of the lower density is a lower target mass which leads to a lower interaction rate.

Since the TPCs are exposed to the neutrino beam from the beginning of the T2K experiment, enough data has been gathered to make first analyses of neutrino gas interactions. The benefits of these measurements are reaching previously inaccessible regions in the phase space to further study nuclear effects.

The precision of such an analysis is enhanced by a good knowledge of the gas properties. This can lead to a better performance of the detector and lower systematic uncertainties. The recent analysis from [20] shows a respectable difference between data and Monte Carlo samples, which could be improved with a better understanding of the actual gas properties in the TPCs.

2.5. High Pressure Detectors

As explained, cross-section measurements performed in TPCs have a lower momentum threshold compared to solid state detectors. Unfortunately, the neutrino interaction rates are quite low due to the small target masses of gaseous detectors. Higher probabilities for neutrino interactions can be reached by increasing the number of target atoms. This can be done by increasing the pressure inside the TPCs.

The concept of high-pressure TPCs is currently part of investigation for near detectors for future long baseline neutrino experiments like DUNE and Hyper-Kamiokande. High-precision cross-section measurements are imperative to reach their goals of systematic uncertainties at a $1-2\,\%$ level.

In [21], a prototype of a high-pressure TPC is proposed which was investigated in a testbeam between August and September 2018. The working group in Aachen attended this testbeam with a gas monitoring chamber developed to operate under pressures of up to 10 bar. This high-pressure GMC is described in [22].

Chapter 3

Magboltz Simulation Studies

The transport of electrons in gases is sensible to changes of the environmental parameters temperature and pressure. Electric fields as they are used in TPCs also affect the diffusion coefficients and the drift velocity of gases.

Another factor are magnetic fields. In case of a magnetic field parallel to the electric field only the transverse diffusion coefficient is affected. Given the enormous complexity of field configurations only this case is studied here.

In this chapter gas mixtures simulated with the program `MAGBOLTZ` [23] are presented. This program performs a numerical integration of the Boltzmann transport equation and computes the relevant gas parameters e.g. drift velocity v_d, transverse d_t and longitudinal diffusion d_l. This has to be done since there are no analytic formulas that describe these quantities.

3.1. Simulation of gas parameters

To simulate the diffusion coefficients and the drift velocity a framework is used where the numerical simulation software `MAGBOLTZ` is embedded into `Garfield++` [24], described in [25]. This framework which is called **magsim** uses v1r0 of `GARFIELD++` with an adaptation to make use of `MAGBOLTZ` version 10.6 .

The desired gas mixtures are specified in volume fractions of the pure gas contents. Then these fractions are converted to molecule masses for the calculation done in `MAGBOLTZ`. The results of a simulation are the drift velocity and the three-dimensional diffusion along the track in the specified range of ET/p.

To understand the performance of the gas parameters, several simulations for different gas mixtures are conducted which can also be accessed in a data base.

The diffusion coefficient itself depends on temperature and pressure given the definition from equation 2.13. Therefore, the diffusion coefficients calculated in the simulation are scaled to lab conditions at $T_{\mathrm{lab}} = 293.15\,\mathrm{K}$ and $p_{\mathrm{lab}} = 1013\,\mathrm{mbar}$ by equation 3.1 where T_{sim} and p_{sim} are the values used in the simulation.

$$d_{t/l,n} = d_{t/l} \cdot \frac{\sqrt{T_{\mathrm{lab}}/p_{\mathrm{lab}}}}{\sqrt{T_{\mathrm{sim}}/p_{\mathrm{sim}}}} \tag{3.1}$$

The following examples are simulations with **T2K gas mixture** which is a gas mixture of 95 % argon, 3 % tetrafluoromethane and 2 % isobutane in volume fraction. This gas mixture is used in the TPCs of ND280 of the T2K experiment.

3.1.1. Fit functions

Since there are no analytical formulas to calculate the drift velocity as well as the longitudinal and transverse diffusion coefficients depending on the reduced electric field ET/p, fit functions need to be established to describe the simulated data. Comparisons using these fit functions are more accurate than simply taking single points from the simulation. Given the limited number of electrons used to simulate a single point accurately, simulations vary due to statistic fluctuations. This is mostly an issue concerning the diffusion coefficients and is visible in the error bars in the simulations shown below. During this thesis a deficiency in the error propagation of the diffusion coefficients in `GARFIELD++` was found. This was corrected in the simulation below.
In the following, the fit functions for both diffusion coefficients and the drift velocity are described. For each of them a different fit function is needed due to their different behaviour with increasing ET/p. All simulations are done with **T2K gas mixture**.

- **Drift Velocity:** The fit function for the drift velocity v_d is taken from [25]. It describes the simulated points especially well around the maximum of v_d as shown in figure 3.1.

$$v_d(ET/p) = (a + b \cdot ET/p) \cdot \exp(-d \cdot ET/p) + c \tag{3.2}$$

- **Longitudinal Diffusion:** The fit function for the longitudinal diffusion coefficient d_l is mostly formed by an exponential function with a negative coefficient b. The fit describes most of the range shown in figure 3.2. Excluding the large error bars, the usability of the fit is apparent in the residual plot in figure 3.2.

$$d_l(ET/p) = \exp(a + b \cdot ET/p) + c \tag{3.3}$$

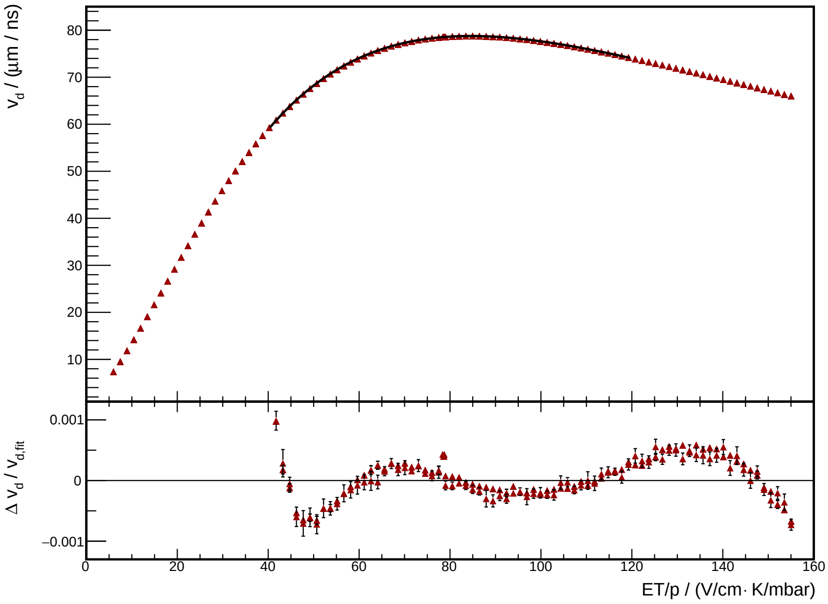

Figure 3.1.: `MAGBOLTZ` simulation of the drift velocity for T2K-gas with empirical fit.

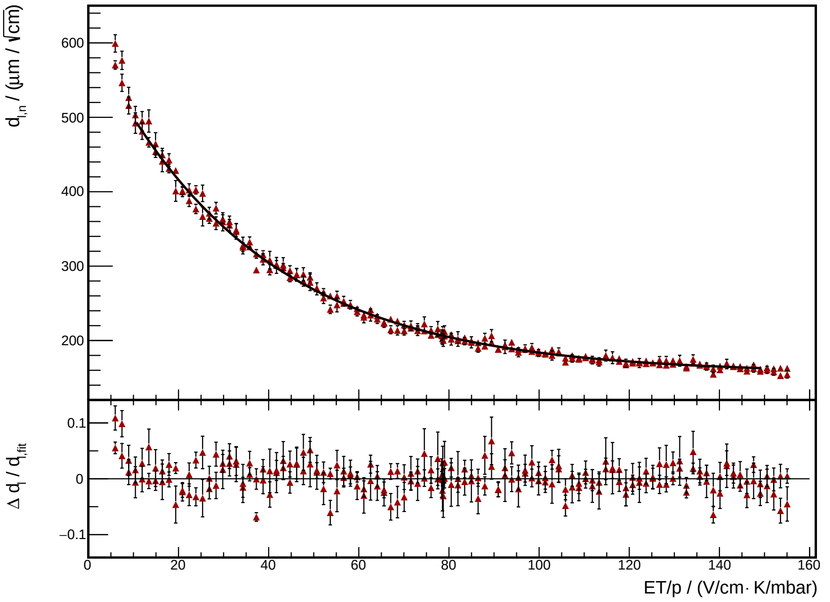

Figure 3.2.: `MAGBOLTZ` simulation of the longitudinal diffusion coefficient for T2K-gas with empirical fit.

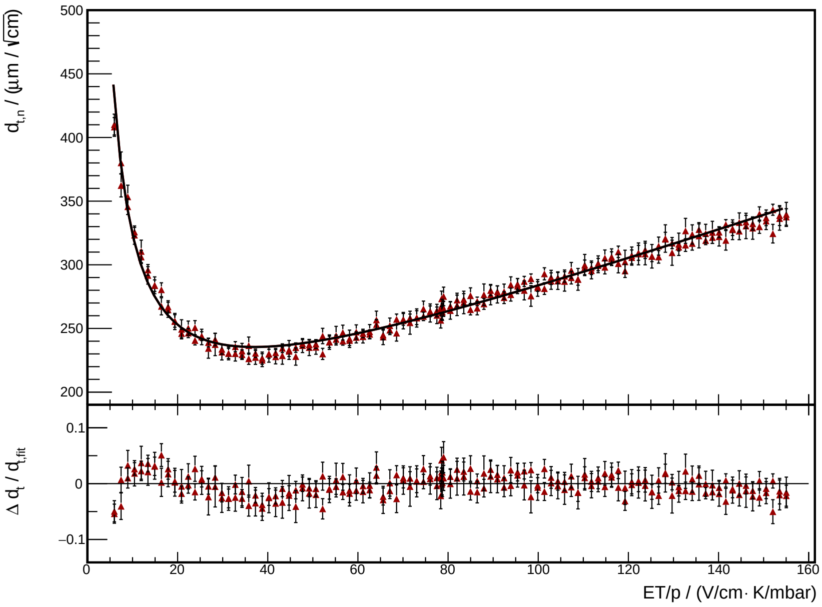

Figure 3.3.: `MAGBOLTZ` simulation of the transverse diffusion coefficient for T2K-gas with empirical fit.

- **Transverse Diffusion:** This function reproduces the behaviour of the coefficient from small values of ET/p to larger ones as shown in figure 3.3. It shows an infinite coefficient for $ET/p = 0$ which decreases and reaches a minimum. From there the coefficient increases again with ET/p.

$$d_t(ET/p) = a \cdot ET/p + \frac{b}{ET/p} + c \tag{3.4}$$

If not mentioned otherwise, these functions are used to describe the `MAGBOLTZ` simulations. Values for the drift velocity or the diffusion coefficients for a certain ET/p are determined by fits using these functions.

3.1.2. Impact of B-Fields

Applying a magnetic field to a drift volume affects the drift velocity and the diffusion coefficient due to Lorentz forces. The magnitude of this influence is depending on the magnetic field strength and the angle between the electric field and the magnetic field. Regarding the case of a magnetic field parallel to the electric field only the transverse diffusion coefficient is influenced. Commonly used TPCs provide parallel fields.
Figure 3.4 shows the fitted functions for the transverse diffusion coefficients. The relevant simulations were done without magnetic field represented by the blue line and with a magnetic field parallel to the electric field with $B = 0.2\,\mathrm{T}$ shown as red dotted line. Both simulation are done for T2K gas mixture.

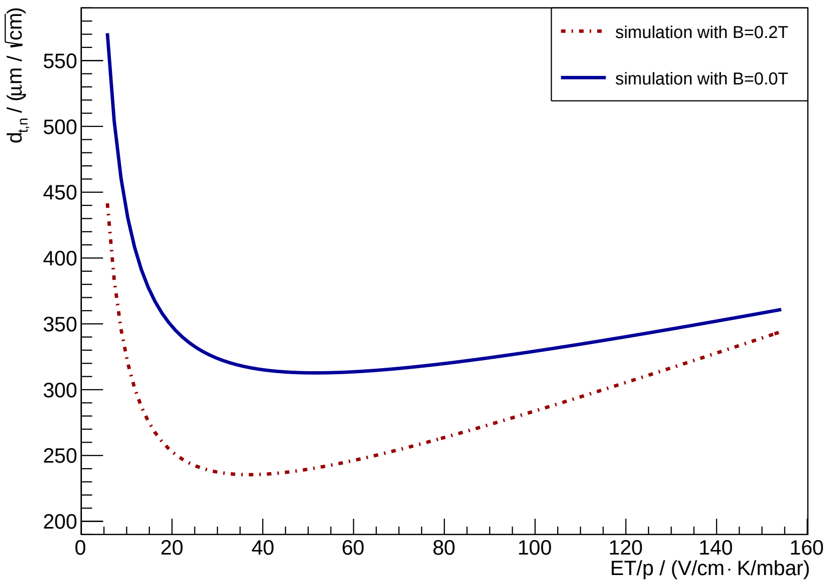

Figure 3.4.: Comparison between `MAGBOLTZ` simulations of the transverse diffusion coefficient with and without application of a magnetic field. The blue line is the fit result of a simulation without magnetic field. The red line is the result of a simulation with $B = 0.2\,\mathrm{T}$. The magnetic field is parallel to the electric field. Both simulations were done for the T2K gas mixture.

Comparing the simulations allows the conclusion that applying an magnetic field parallel to the electric field lowers the transverse diffusion coefficient. This becomes most apparent in figure 3.4 around the minimum. The transverse diffusion coefficient with $B = 0.2\,\mathrm{T}$ is dropping faster with rising ET/p and the minimum is reached at a smaller ET/p value. After the minimum the increase of the coefficient is more rapid than without magnetic field.

The same comparison is done for the drift velocity and the longitudinal diffusion coefficient in A. It shows that in case of a magnetic field parallel to the electric field neither of these quantities is influenced.

CHAPTER 4

Simulation Studies on Charge Distributions and Signal Generation

The toy simulations described in the following are conducted to understand the signal used in the diffusion analyses. Therefore, the shaping function of the MicroMeGaS readout electronics in ND280 is investigated. This is important to find out how the original width of the electron cloud can be reconstructed from the electric signal.
Another toy simulation is used to determine the charge distributions on pad structures. This is necessary to analyse the transverse diffusion in the ND280 TPCs and the gas monitoring chambers. In case of the T2K gas monitoring chambers the toy simulation can be used to determine the required pad size to measure the diffusion coefficient directly under the assumption of predefined drift distances.
The direct fitting of the charge distribution is not capable of measuring the desired transverse diffusion coefficients since the pads are too large for the charge to be split over enough pads. Therefore, another method is investigated. To prove its usability also a toy simulation is performed. This simulation in addition provides the calibration function needed to translate the resulting width to the requested one.

4.1. Simulation of the AFTER-Chip

The AFTER-chip (**A**SIC **F**or **T**PC **E**lectronic **R**eadout) is used to collect and filter the electric signal from the MicroMeGaS [18]. The signals are sampled continuously in Switched Capacitor Arrays, SCA. When a trigger arrives, the signals are read out by external 12-bit quad-channel ADCs on the Front-End Card, FEC.
Each of the 72 channels has a front-end part and an SCA part for sampling. The components of the front-end part are a Charge Sensitive Amplifier, CSA, a Pole-Zero Can-

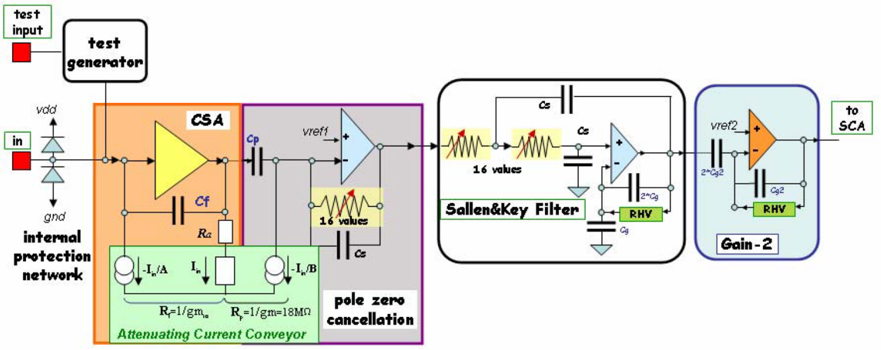

Figure 4.1.: Architecture of the AFTER front-end part. [18]

cellation block, PZC, a RC^2-filter and a Gain-2 amplifier. These parts form the shaped signal waveform which is recorded. A scheme of the architecture of the front-end part is shown in figure 4.1.

4.1.1. Shaping function studies

A toy simulation is used to simulate the response shaping function of the AFTER-chip. The simulation is based on the same algorithms as the electronic simulation for ND280 Monte Carlo samples. These algorithms are defined in the ND280 software class `elecSim`.

To produce a signal in the simulation first an electron distribution is created according to a drift time. This drift time is related to the drift distance between the origin of ionization in the gas created by a traversing particle and the arrival of the cloud at the MicroMeGaS. It is calculated by the predefined drift velocity v_d by $\Delta t = \Delta l / v_d$. In the ND280 the used drift velocity is $v_d = 78.5\,\mu\text{m/ns}$.

The resulting distribution of electrons is gaussian with the width σ_{LD} given by the longitudinal diffusion constant d_l using

$$\sigma_{LD} = d_l \cdot \sqrt{v_d \cdot \Delta t}. \tag{4.1}$$

This electron distribution is then processed through the simulation of the AFTER-chip. The shaped signal is simulated by the sum of the single electrons in the cloud.

$$q_{e^-} = \left(\frac{t_{in}}{t_{Rise}}\right)^3 \cdot \exp\left(-\frac{t_{in}}{t_{Rise}}\right) \cdot \sin\left(\frac{t_{in}}{t_{Rise} C_0}\right) \cdot C_1 \tag{4.2}$$

depicts the response function for a single electron with arrival time t_{in}. In this equation t_{Rise} is the rise time and C_0 and C_1 are constants given by the hardware. The values used for the simulation are given in table 4.1.

The digitization is simulated in the next step by modulating the sum of all single electrons with the gain and transfer it to a DAC value.

Table 4.1.: Parameters for the AFTER-chip simulation.

parameter	t_{Rise}	C_0	C_1
value	71 ns	3.5	0.91629 fC

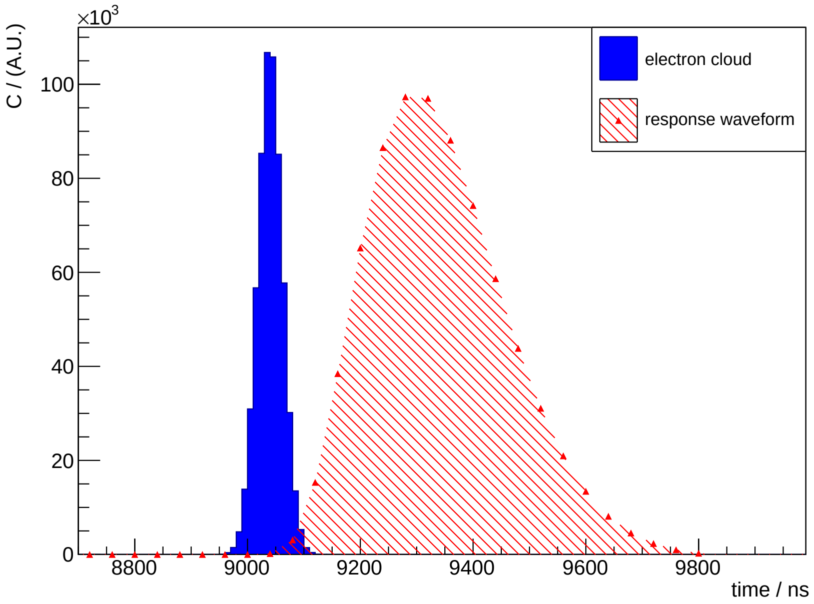

Figure 4.2.: Comparision of a electron cloud and the shaped signal of the AFTER-chip for the same cloud.

Figure 4.2 shows a comparison between the electron distribution and the digitized response waveform from the AFTER-chip. The electron distribution is getting roughly six times wider by shaping. Furthermore, the original gaussian shape of the distribution is smeared with a longer falling edge. Therefore, the signal is not symmetric around the maximum anymore, which requires studying how the width of the signal can be reconstructed.

4.1.2. Calibration factor for longitudinal diffusion measurement

The widths of the waveforms need to be determined to measure the longitudinal diffusion coefficient from the electric signal on the pads. Therefore, it is assumed that the simulation can be used as some kind of black box which produces the correct output waveform according to an electron cloud with a certain width as input. Additionally, it is important that the simulation reproduces the real waveform sufficiently well.
First of all, a parametrization of the waveform of the shaped signal is needed. As shown in figure 4.2 the waveform is not symmetrical, but reminds of a gaussian distribution

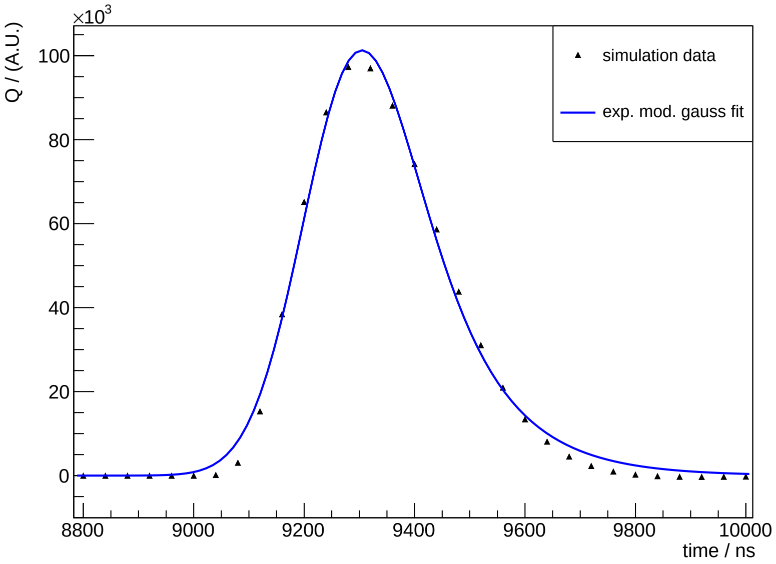

Figure 4.3.: Example for the fit of a simulated waveform with the exponentially modified gaussian function.

with a falling tail. This waveform can be described by a fit of an exponentially modified gaussian function

$$C \cdot \exp(-\lambda(x-\mu)) \cdot \operatorname{erfc}\left(\frac{x-\mu}{\sqrt{2}\sigma}\right). \tag{4.3}$$

This exponentially modified gaussian function is a convolution of a gaussian function with an exponential function. In this fit function μ is the mean and σ the sigma parameter of the gaussian function while λ is the parameter of the exponential function. The scaling parameter C is used to adjust the fit function to the maximum of the waveform.

In figure 4.3 a waveform fitted with the fit function using equation 4.3 is shown. The fit function describes the waveform sufficiently well, even though the rising and falling parts show smaller deviations and the fitted maximum of the function seems to be slightly higher. Since these deviations are small there are no concerns about using this function to determine the width of the signal. Moreover the fitted width is calibrated to the incoming width of an electron cloud anyway.
A simulation with different input width of electron clouds is used to calibrate the output width of the signal to the input width. For every cloud width σ_{in} the waveform is fitted and the determined width σ_{out} is filled into a two dimensional histogram of σ_{in}^2 versus σ_{out}^2. The result of this simulation is presented in figure 4.4. It shows that σ_{out}^2 and σ_{in}^2 have a linear dependence, which means the calibration can be realized with a linear fit. Since the longitudinal diffusion coefficient is determined by a linear fit to the squared calibrated width as function of the drift coordinate x, only the slope of the fit is relevant for the correction. The calibration factor κ is therefore defined as $\sigma_{in}^2 = \kappa \cdot \sigma_{out}^2$. The simulation results in a correction factor of $\kappa = 0.98652 \pm 0.00097$.

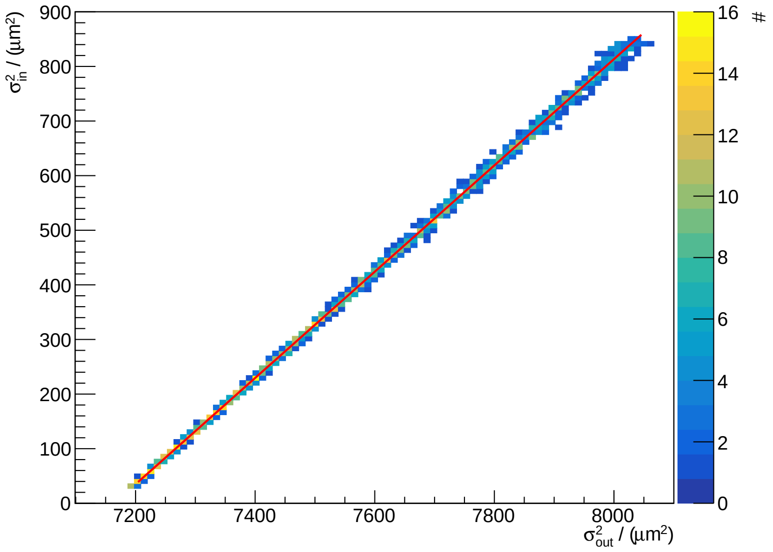

Figure 4.4.: Calibration curve for the width of the waveform.

4.2. Charge Distribution on Pad Geometry

The toy simulation studies described in the following aim to understand how the gaussian charge distribution looks like on a readout structure segmented in pads. In the ND280 TPCs a rectangular pad structure is used while a squared one is used in the gas monitoring chambers. The objective of these studies is the projection from gaussian clouds in the transverse direction on a segmented read out which is needed for the measurement of the transverse diffusion.

4.2.1. Double-Error-Function

First of all, the mathematical description is developed by investigating the situation of a charge cloud hitting on a pad in one dimension. In this case the cloud can be described as a one dimensional gaussian function and the pad as a rectangle function. By convoluting both together we get the function

$$\begin{aligned}\int_{-\infty}^{\infty} \mathrm{rect}(a) \cdot C \cdot \frac{1}{\sqrt{2\pi\sigma^2}} \exp\left(-\frac{((x-\tau)-\mu)^2}{2\sigma^2}\right) d\tau = \\ \frac{1}{2} \cdot C \cdot \left(\mathrm{erf}\left(\frac{a+\mu-x}{\sqrt{2}\sigma}\right) + \mathrm{erf}\left(\frac{a-\mu-x}{\sqrt{2}\sigma}\right)\right).\end{aligned} \tag{4.4}$$

It uses the standard parameters of the gaussian function μ for the mean value and σ for its width. Parameter a is half of the pad width and C a scaling parameter. For small widths compared to the padsize the function looks like a rectangle with the width of the pad as shown in figure 4.5. For wider widths the function follows the shape of a gaussian distribution.

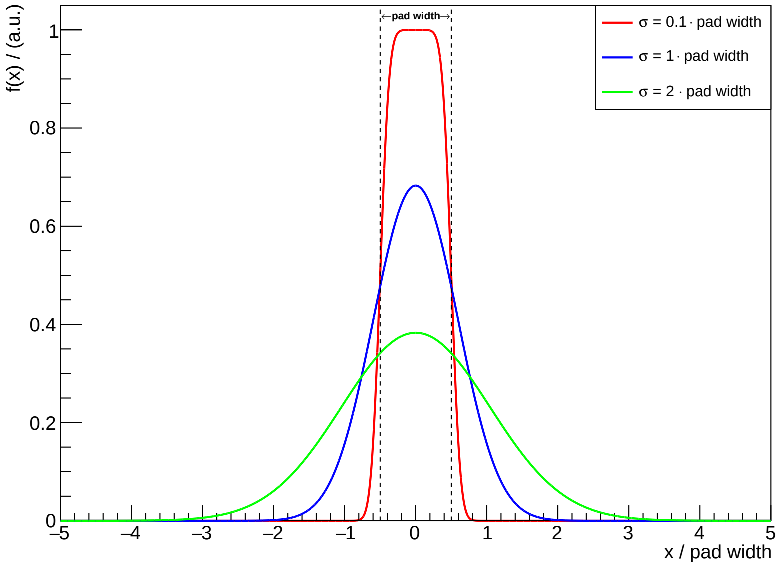

Figure 4.5.: Examples of double error functions with different widths.

Clouds with too small widths, for example clouds with an origin near the pad plane and hence a short drift distance or clouds hitting pads that are too wide, can not be reconstructed since the whole charge is collected on one pad. If the cloud is becoming larger the charge distribution is getting gaussian and the effect of pad structures on the charge distribution decreases.

Furthermore, the projection of the charge distribution depends on the origin of the ionization represented by the mean value of the charge cloud. This provides another challenge in the reconstruction of the charge distribution. Considering pads in just one dimension it is necessary to use at least four pads in order to get a reasonable reconstructed mean value for a charge cloud. This is a result of a toy simulation. It shows the discrepancy between the reconstructed mean value and the true mean of the cloud in dependence on the true mean. The mean $x_{c.o.c.}$ is determined by the center of charge calculated with

$$x_{c.o.c.} = \frac{\sum_i q_i \cdot x_i}{\sum_i q_i}. \tag{4.5}$$

The result of this study is shown in figure 4.6. The study proves that for only two pads the reconstruction of the mean is rather poor with large deviations which are getting smaller with a higher number of pads. The size of the pads is chosen such that they cover the same area. This means all configurations see the same signal that is distributed to a varying number of pads. If the cloud hits at least four pads the discrepancy between reconstructed and true mean decreases and a deviation of 2% at maximum is achieved.

The results of the charge distributions, which are reconstructed using $x_{\text{c.o.c.}}$, are shown in figure 4.7. By using x_{true} the charge distributions are reconstructed correctly in every case. If $x_{\text{c.o.c.}}$ is applied for just two pads the reconstructed distribution is triangular

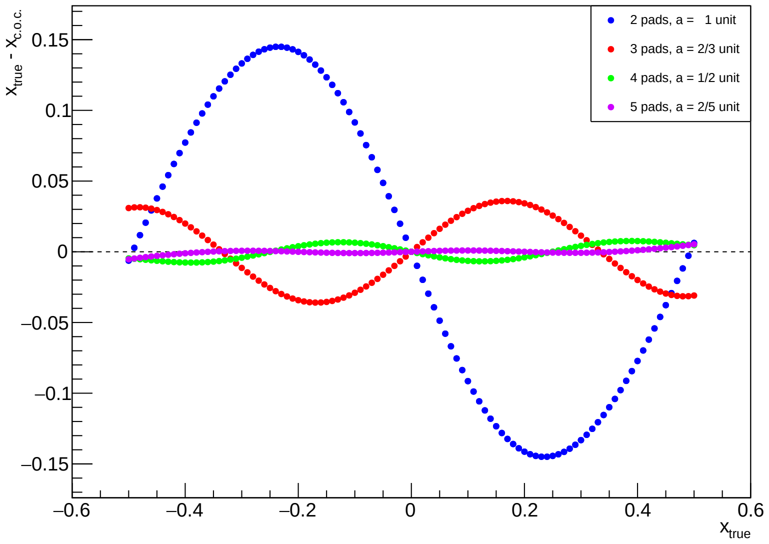

Figure 4.6.: Discrepancy between the reconstructed mean of the electron cloud $x_{\text{c.o.c.}}$ and the true mean x_{true} w.r.t. x_{true}.

because both pad positions have to lie on a straight line. Using three pads the reconstructed distribution converges with the actual charge distribution but still has some aberrations. The results of the distribution with four or five pads show no distinguishable deviations from the true distribution.

Even though the shapes reconstructed with less than four pads are not fully covering the true shape of the distribution, it is possible to determine the full width half maximum, FWHM, to get a parameter representing the width of distribution. Looking closely to the distributions in figure 4.7 the true distribution and the reconstructed one have points of intersection at the point where the half of the maximum is reached. Therefore, a reconstruction to determine the transverse diffusion coefficient is possible if at least two pads collect charge.

A study to check the relation between the FWHM of the reconstructed charge distribution and the width of the input cloud is performed in [26]. For this the pads are configured in five rows consisting of four connected pads, which is not the original pad configuration used in the T2K gas monitoring chambers. The pitch between the rows is 5 mm.

This study reveals that charge clouds larger than approximately 600 μm are reconstructible neglecting noise on the signal. Since the shorter of the two drift distances in the monitoring chambers is approximately 1.7 cm, only diffusion coefficients larger than 460 $\mu\text{m}/\sqrt{\text{cm}}$ are measurable.

Unfortunately, this method is not suitable to measure the transverse diffusion coefficient for T2K gas due to this limitations since it has diffusion coefficients in the order of 300 $\mu\text{m}/\sqrt{\text{cm}}$. As the measurement for T2K gas is a benchmark this method can not be used in this thesis. Instead another method is introduced using the ratio of the

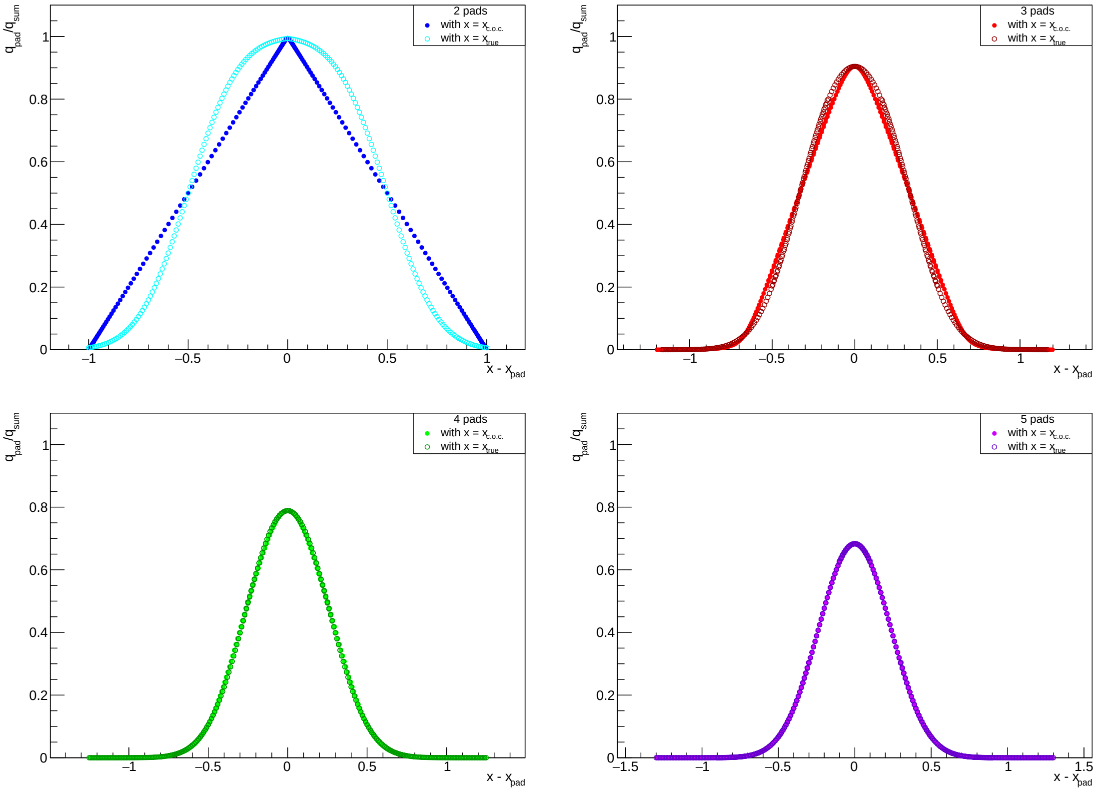

Figure 4.7.: Simulated charge distribution with different numbers of pads. Top left shows the distribution with two pads, top right with three pads, bottom left with four pads, bottom right with five pads.

charge on the top side to the total collected charge. This method is described in 4.2.2. To determine the transverse diffusion coefficient in the TPCs of ND280 the origin of the cloud is reconstructed by track fitting. Here, the track fitting is done by global fitting which makes the reconstruction quite accurate. The charge distributions reconstructed by this are sufficient to measure their widths as input to the measurement of the transverse diffusion coefficient.

4.2.2. Cloud width reconstruction by the charge ratio

The method described in the following allows to measure much smaller widths of charge clouds than feasible by direct fitting of the charge distribution collected with the pads of the gas monitoring chambers. The method is a modified approach of the one used in [27]. In this method, charge clouds are investigated which are distributed to only two pads. Figure 4.8 shows examples for these clouds with two different widths and their signals received by the pads. Depending on the width and the mean position of the cloud, the charge is separated between the pads. If the width of the cloud is small, it is possible that the charge is only recorded by one pad, while a cloud which

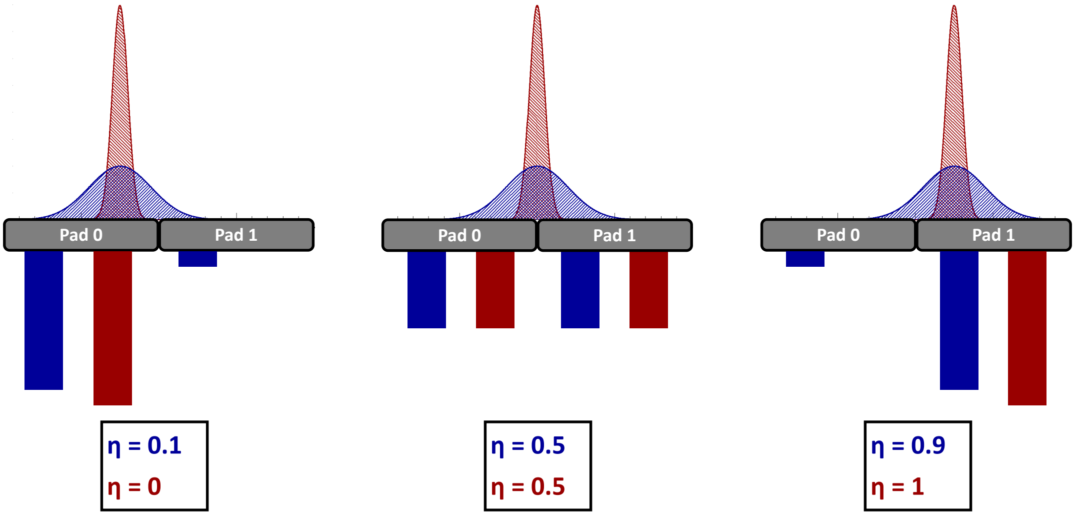

Figure 4.8.: Charge separation on two pads for charge clouds with different widths.

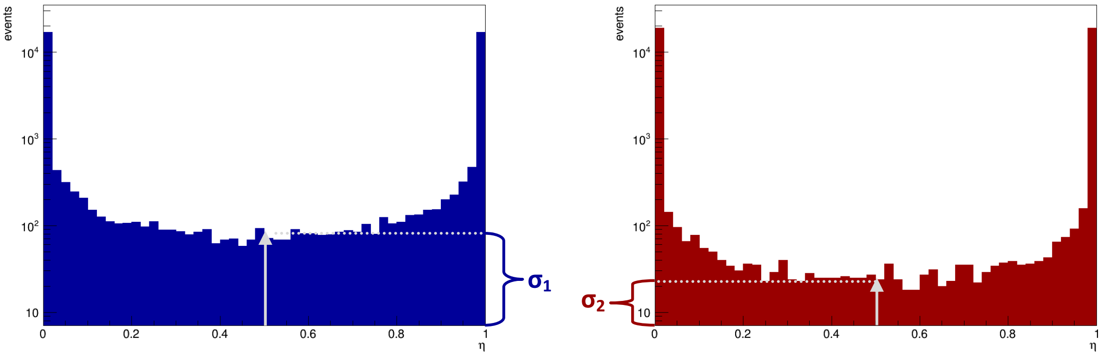

Figure 4.9.: Charge ratio distribution for signals with different widths.

has a larger width and the same mean position separates its charge to two pads. From the charge collected by the pads, the ratio η is calculated by

$$\eta = \frac{q_0}{q_0 + q_1} \tag{4.6}$$

for N clouds with different mean positions. From its distribution the mean charge distribution can be reconstructed. Figure 4.9 shows two of these distributions. The blue distribution on the left side is found for a larger width of the cloud and the red on the right side for a smaller width. The difference in the width results in a different height in the center of the η distribution. Small widths yield less entries around an η of 0.5 relative to the total number of events.
In [27] this method is described to reconstruct the charge distribution with two silicon strips, where the charge clouds are striking the pads with a uniform local distribution.

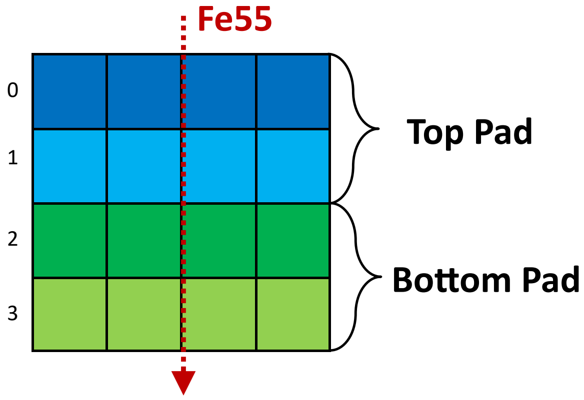

Figure 4.10.: Pad configuration for reconstruction of electron cloud width by charge ratio.

For the measurement performed in this thesis four columns of pads are used of which two are connected, respectively. Using four pads has the advantage of being able to reconstruct broader charge distribution. The configuration of the pads is shown in figure 4.10. The local distribution also has to be adapted to an exponential distribution. A simulation is done with the objective of proofing the feasibility of modifying the method in [27]. It so happens that the modified method yields a sufficiently precise result to determine the width of the charge distribution albeit the results need to be corrected with a calibration function.
The local distribution of charge clouds along the beam direction of the iron-55 γ-source (red arrow in figure 4.10) $\frac{dN}{dx}$ is assumed to be exponential. It is described by an exponential distribution with the absorption length λ_γ

$$\frac{dN}{dx} = \frac{N_0}{\lambda_\gamma} \cdot \exp\left(\frac{-x}{\lambda_\gamma}\right). \tag{4.7}$$

All measured events N_{tot} are limited in distance by a and b, with a being the middle between the two top pad columns and b being the middle between the two bottom columns. N_0 is constrained by a, b and the measured events N_{tot}:

$$\int_a^b \frac{dN}{dx} dx \Leftrightarrow N_0 = \frac{N_{\text{tot}}}{\exp(-a/\lambda_\gamma) - \exp(-b/\lambda_\gamma)}. \tag{4.8}$$

Of all collected events with more than 50% of charge on the inner two pad columns e.g. $q_1 + q_2 > 0.5 \cdot (q_0 + q_1 + q_2 + q_3)$ the charge ratio η is measured according to

$$\eta = \frac{q_0 + q_1}{q_0 + q_1 + q_2 + q_3}. \tag{4.9}$$

One of these distributions is shown in figure 4.11 on the left side. This example shows the distribution for a drift distance of $s = 1.7\,\text{cm}$ and a transverse diffusion coefficient of

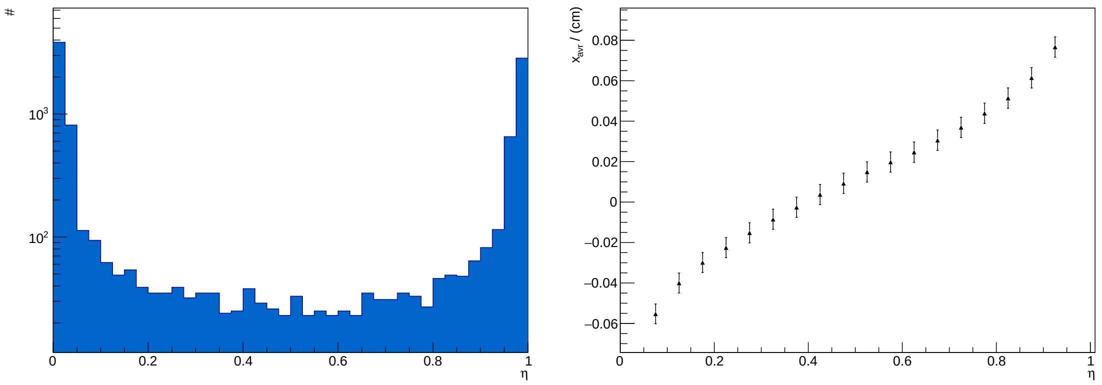

Figure 4.11.: Simulation of the charge ratio distribution and the average impact point for the reconstruction of the width of electron clouds in the gas monitoring chambers. The simulation is done for the short drift distance and T2K-gas on the working point. Charge ratio distribution on the left side. Average impact point on the right side.

$d_t = 323\,\mu\mathrm{m}/\sqrt{\mathrm{cm}}$. It suits the situation of the short drift length in the gas monitoring chambers for T2K gas mixture at the working point.
From this distribution the average impact point $x_{\mathrm{avr.}}$ is determined by

$$\int_a^x \frac{dN}{dx'}dx' = \int_0^{\eta'} \frac{dN}{d\eta}d\eta \tag{4.10}$$

The scale of $x_{\mathrm{avr.}}$ needs to be corrected to match the scale of η. Therefore, the offset $-\frac{a+b}{2}$ is added to $x_{\mathrm{avr.}}$. The functional description of $x_{\mathrm{avr.}}$ in dependence of η is

$$x_{\mathrm{avr.}} = -\lambda_\gamma \ln\left(\exp\left(-\frac{a}{\lambda_\gamma}\right) - \frac{1}{N_0}\cdot\int_0^{\eta'}\frac{dN}{d\eta}d\eta\right) - \frac{a+b}{2}. \tag{4.11}$$

The right side of figure 4.11 shows the relating $x_{\mathrm{avr.}}$ with respect to η for the example on the left side.
As stated in [27] for the charge collected by the pads for an ionization at $x_{\mathrm{avr.}}$, the one dimensional charge distribution $f(\xi)$ on the top side is $q_{\mathrm{top}} \propto \int_{-\infty}^{x_{\mathrm{avr.}}} f(\xi)d\xi$ and on the bottom side $q_{\mathrm{bottom}} \propto \int_{x_{\mathrm{avr.}}}^{\infty} f(\xi)d\xi$. Merging this with the definition of η from equation 4.9 and the exponential event distribution from equation 4.7, the relation

$$\begin{aligned} \frac{dN}{d\eta} &= \frac{dN}{dx}\cdot\frac{dx}{d\eta} = \frac{N_0}{\lambda_\gamma}\cdot\exp\left(-\frac{x}{\lambda_\gamma}\right)\cdot\frac{1}{f(-x)} \\ \Leftrightarrow f(-x) &= \frac{N_0}{\lambda_\gamma}\cdot\exp\left(-\frac{x}{\lambda_\gamma}\right)\cdot\frac{1}{\frac{dN}{d\eta}} \end{aligned} \tag{4.12}$$

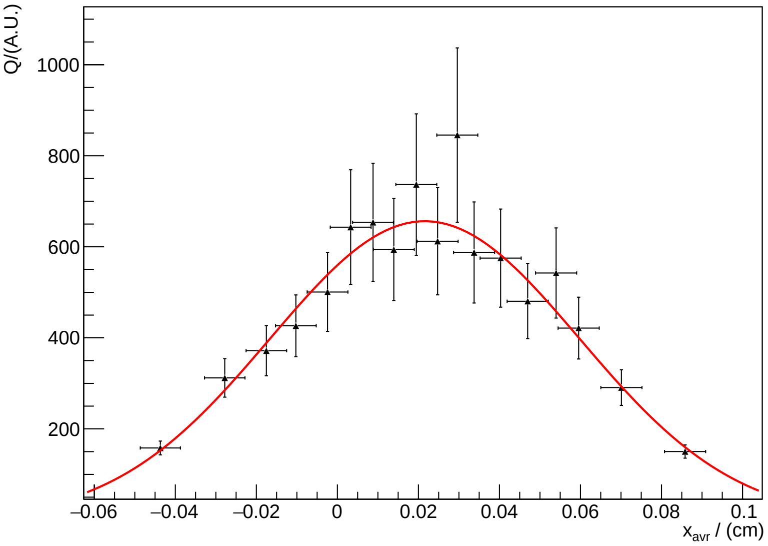

Figure 4.12.: Reconstructed charge distribution in dependence on the average impact point $x_{\text{avr.}}$ for a simulation with T2K gas mixture at the working point and the short drift distance in the GMCs.

is obtained which depicts the charge distribution in dependence on the average impact point $x_{\text{avr.}}$.

The charge distribution reconstructed for the above simulation is shown in figure 4.12. It possesses the gaussian shape expected from the input distribution. The uncertainties contained in the distribution strongly depend on the number of simulated events.

The propagation of statistical uncertainties on the average impact point $x_{\text{avr.}}$ result in

$$\sigma^2_{x_{\text{avr.}}} = \left(\frac{\lambda_\gamma}{N_0} \cdot \frac{\sigma_{N(\eta \leq \eta_0)}}{\exp\left(-a/\lambda_\gamma\right) - N(\eta \leq \eta_0)/N_0} \right)^2 . \tag{4.13}$$

It can be said that only the number of events for $\eta = \eta_0$ expressed by $N(\eta \leq \eta_0) = \int_0^{\eta_0} \frac{dN}{d\eta} d\eta$ has a binomial statistical uncertainty of $\sigma_{N(\eta \leq \eta_0)}$. N_0 is determined by the data set and λ_γ is an external parameter. Therefore, both are without uncertainty in this calculation.

The uncertainty for the charge distribution $\sigma_{f(x)}$ depends on $\sigma_{x_{\text{avr.}}}$ and the uncertainty on the rate $\frac{dN}{d\eta}$. The propagation of these uncertainties is

$$\sigma^2_{f(x)} = (f(x))^2 \cdot \left(\left(\frac{\sigma_{dN/d\eta}}{\frac{dN}{d\eta}} \right)^2 + \left(\frac{\sigma_{x_{\text{avr.}}}}{\lambda_\gamma} \right)^2 \right). \tag{4.14}$$

Using this simulation it is again examined whether there is a functional dependency between the width of the ingoing charge distribution and the reconstructed one. Therefore different input widths were simulated and compared to the width which is reconstructed from the η-distribution. The result is shown in figure 4.13. To describe the

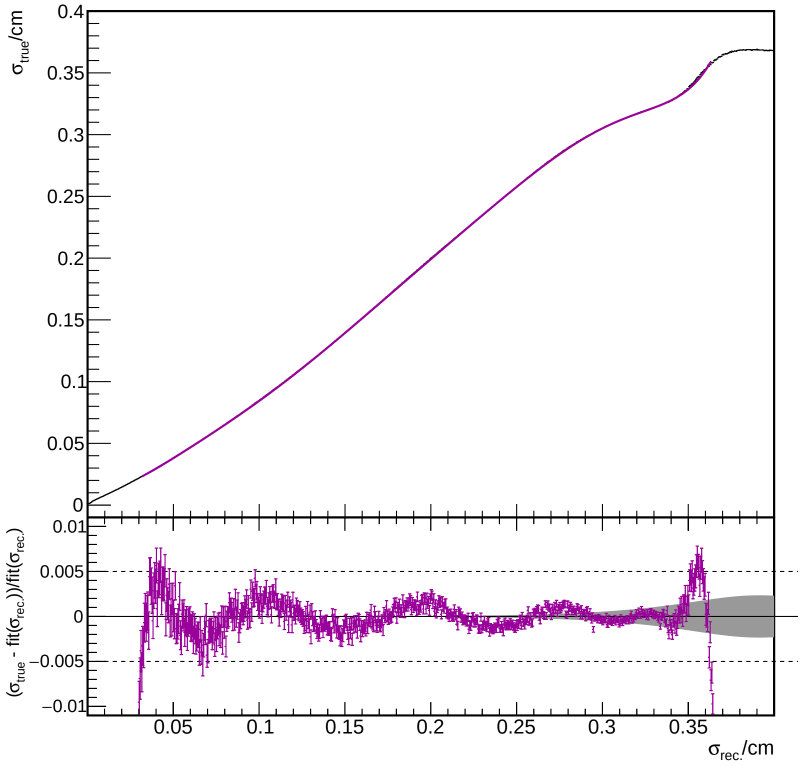

Figure 4.13.: Calibration function for the reconstruction of the charge distribution width by the η distribution.

functional dependence empirically, a eight degree polynomial function is used. The function describes the relationship between the widths sufficiently well within the fitted range as depicted by the residual. The parameters of this function are shown in table 4.2. The deviation is 0.5 % at maximum. For widths outside of the fitted range no sufficient functional connection is present, as depicted in the flattening of the relationship. The maximum reconstructable input width is $\sigma_{in} \approx 3500\,\mu\text{m}$. With the longer drift distance in the GMCs of $s_l \approx 13.8\,\text{cm}$ this limits the measurable transverse diffusion coefficient to $d_t \approx 940\,\mu\text{m}/\sqrt{\text{cm}}$.

Table 4.2.: Parameter of the calibration function for the reconstruction of the charge distribution width from the η distribution. Fixed parameters have no statistical uncertainty.

Parameter	**value**	**uncertainty**
a_0	0.0163186	-
a_1	-0.688209	3.78204e-05
a_2	46.2589	-
a_3	-746.177	-
a_4	7070.63	-
a_5	-39256.5	-
a_6	126173	-
a_7	-217500	0.559703
a_8	155266	1.65926

Chapter 5

Measurements with the ND280-TPCs

This chapter presents measurements of the diffusion coefficients and the drift velocity using the TPCs in the near detector ND280 of the T2K experiment. Since the TPCs are built as trackers, they are not designed to measure these quantities. Nevertheless, it is possible to reach a moderate to high precision for all three measurements.

The determined diffusion coefficients as well as the drift velocity are measurements for a complete T2K run. This means that smaller changes due to fluctuations of pressure and temperature have to be compensated. This is different from measurements with the gas monitoring chambers which take these environmental fluctuations into account and measure the time depending variation of the values. Therefore, their data is used as calibration constants for the TPCs. The average diffusion coefficients and drift velocity measured with the TPCs are used to verify the input values for the Monte Carlo production.

5.1. Diffusion measurements

This section provides the determination of the longitudinal and transverse diffusion coefficient with the TPCs of the ND280 detector. The measurement concepts are introduced and the data selection and their cuts are explained. Before the data results are presented the results from Monte Carlo samples are shown and discussed as a reference. The final result of the data is presented including an estimation of the systematic uncertainties.

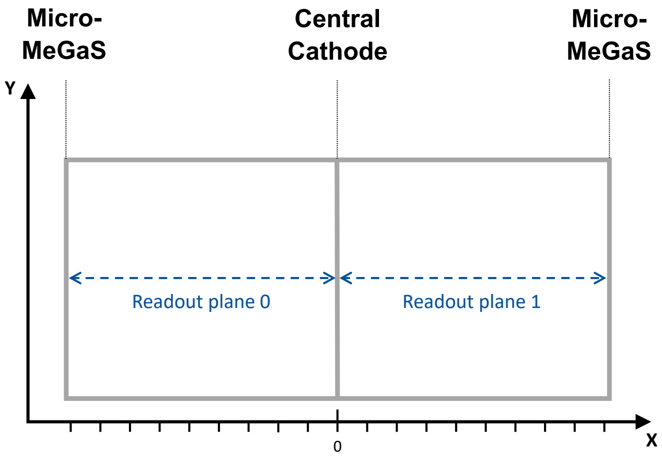

Figure 5.1.: Definition of the readout planes for the TPCs.

5.1.1. Measurement concepts

Both diffusion coefficients can be measured by the change of the electron cloud width in their spatial projection in dependence on the travelled drift distance.
The width of an electron cloud projected in the longitudinal coordinate can be determined by the time width of the electrical signal at the anode.
The transverse width on the other hand is given by the charge distribution on the pad plane perpendicular to the direction of the ionizing particle going through the TPCs.

5.1.1.1. Longitudinal diffusion

The longitudinal diffusion coefficient is measured by the width of the electrical signal in time introduced by an electron cloud drifting to the MicroMeGaS. Therefore particle tracks are split up in their reconstruction clusters. These clusters consist of pad hits for which, respectively, the waveform as well as the y- and z-coordinate is given. The x-coordinate which is the coordinate parallel to the drift direction, is determined for the whole reconstructed cluster by the drift time.
To get the width of the waveform a fit is performed as described in equation 4.2. According to the studies done in this chapter the fitted σ_{fit} is corrected by a factor $\kappa = 0.98652 \pm 0.00097$. This calibration is done via $\sigma_l^2 = \kappa \cdot \sigma_{\text{fit}}^2$.
The x-coordinate and the squared corrected width of the electron cloud, σ_l^2, are filled into a two-dimensional histogram. From this two-dimensional histogram the mean squared width in dependence on the x-coordinate is determined by gaussian slice fits. Since x is parallel to the drift direction it represents the drift distance. The longitudinal diffusion coefficient d_l can then be determined by

$$\sigma_l^2(x) = d_l^2 \cdot x + \sigma_0^2. \tag{5.1}$$

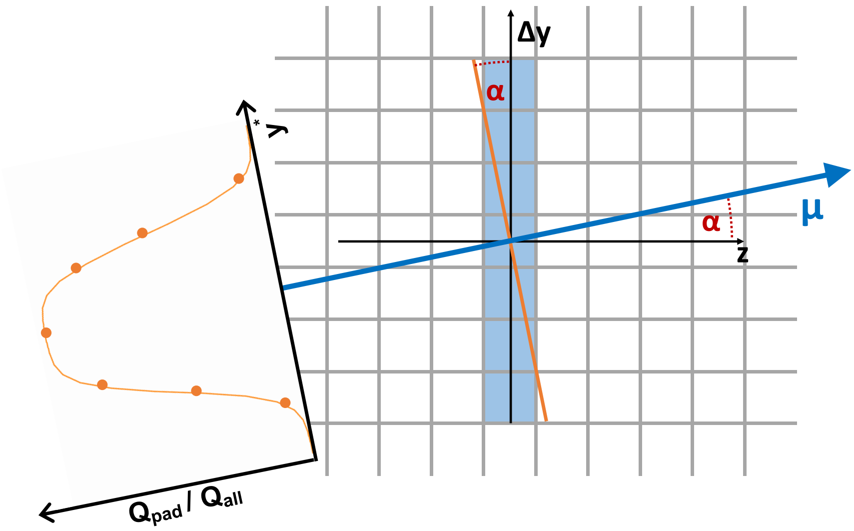

Figure 5.2.: Sketch of the charge distribution correction in the determination of the transverse diffusion coefficient.

The offset σ_0 given in this equation can be seen as a basic width of the signal conditioned by the amplifier and has no relevance for this analysis.
For each readout plane of a TPC a single fit is performed. These readout planes are defined in figure 5.1. The fit range for readout plane 0 is $-80\,\text{cm} < x < -10\,\text{cm}$ and the range for readout plane 1 is $10\,\text{cm} < x < 80\,\text{cm}$. These fits are repeated for all three TPCs of ND280.

5.1.1.2. Transverse diffusion

The transverse diffusion coefficient is measured by the charge distribution perpendicular to the drift direction of an electron cloud arriving at the MicroMeGaS. In this analysis, only horizontal tracks are used. The clusters of them consist of vertically distributed hits, which are reconstructed to one cluster. For each row of pads a separate cluster is reconstructed. The selected tracks are nearly parallel with a maximum angle α to the neutrino beam direction.
Figure 5.2 shows a sketch of the determination of a charge distribution for one cluster including the correction for small angles between the track and the beam direction. From every pad hit the charge is reconstructed by a fit of an analytical function. This fit is also used in the TPC reconstruction expansion software `TREx`. The ratio of the single pad charge Q_{pad} and the sum of the charge of all pads in a cluster Q_{sum} is then determined in dependence on the vertical distance of the pad position y_{pad} to the reconstructed charge center position of the cluster y_{reco} i.e. $\Delta y = (y_{pad} - y_{reco})$. Since

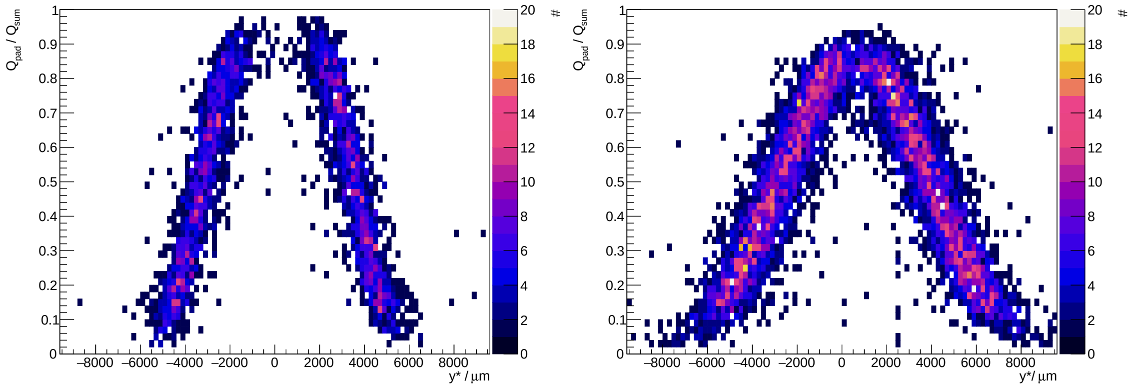

Figure 5.3.: Charge ratio distributions. The left side shows the distribution for a short drift distance, which is more rectangular, the right side the distribution for a far drift distance, which is more gaussian.

the tracks are not fully horizontal tracks, Δy needs to be corrected with the angle between the y- and z-direction of the track

$$y^* = \Delta y \cdot \cos(\alpha) = (y_{pad} - y_{reco}) \cdot \cos(\alpha). \tag{5.2}$$

The charge ratio distribution formed by Q_{pad}/Q_{sum} and y^* can be described as a convolution of a gaussian and a rectangle function as explained in chapter 4.2. These distributions are analysed in sections of the drift coordinate x. Two of these distributions are shown in figure 5.3.

To all of these charge ratio distributions a fit is performed in order to evaluate the mean width σ_t from which the transverse diffusion coefficient is determined, using the function

$$f(y^*;\sigma_t, y_{reco}) = \operatorname{erf}\left(\frac{a + (y^* - y_{reco})}{\sqrt{2}\sigma_t}\right) + \operatorname{erf}\left(\frac{a - (y^* - y_{reco})}{\sqrt{2}\sigma_t}\right). \tag{5.3}$$

In this fit the mean value of the distribution y_{reco} is a free parameter. The half of the pad pitch is $a = 3500\,\mu$m and is a fixed parameter in the fit.

The squared width of the charge distribution is then again investigated in dependence on the drift coordinate x and the transverse diffusion coefficient d_t is determined in analogy to the method used for the longitudinal diffusion coefficient. The linear dependence between σ_t^2 and x is fitted using

$$\sigma_t^2 = d_t^2 \cdot x + \sigma_0^2. \tag{5.4}$$

These fits are done for all TPCs in ND280 with the fit range of $-80\,\text{cm} < x < -10\,\text{cm}$ for readout plane 0 and of $10\,\text{cm} < x < 80\,\text{cm}$ for readout plane 1.

Table 5.1.: Used T2K run separated by MR and ND280 runs with recording dates, delivered spills and delivered POT.

T2K run	MR run	ND280 runs	recording period	recorded POT
4	44	9000 - 9088	2012/10/19 - 2012/11/12	$5.05 \cdot 10^{19}$
4	45	9128 - 9217	2012/11/21 - 2012/12/12	$5.70 \cdot 10^{19}$
4	46	9322 - 9475	2013/01/18 - 2013/02/22	$11.43 \cdot 10^{19}$
4	47	9580 - 9708	2013/02/25 - 2013/04/01	$7.31 \cdot 10^{19}$
4	48	9708 - 9721	2013/04/01 - 2013/04/12	$4.05 \cdot 10^{19}$
4	49	9789 - 9796	2013/05/02 - 2013/05/08	$1.77 \cdot 10^{19}$

5.1.2. Data selection and cut motivations

The measurements of both diffusion coefficients take the same data sets which were processed during production 6. Data sets are used from T2K run 4 with beam trigger which took place from October 2012 until May 2013. The data is corresponding to $3.6 \cdot 10^{20}$ POT (Protons on Target). All related ND280 runs which were used are listed in table 5.1.

For Monte Carlo studies 554 files were used which are listed in table 5.2. These Monte Carlo samples were produced with the neutrino generator `genie` [28]. ND280 configurations with and without a water-filled P0D subdetector are used. Since these analyses only use tracks from secondary particles in the TPCs with no restriction on their origin, these configuration differences can be neglected.

Data samples as well as Monte Carlo samples were processed through ND280-software package v12r2 and the TPC reconstruction is done with `trexRecon` v2r28.

For both diffusion coefficients, most selection criteria and cuts are the same and are explained in the following. All analysed tracks need a valid T_0 to make sure the track is reconstructed correctly and the reconstructed x-coordinate gives the right drift distance. T_0 is the time when a particles crosses a TPC and is given from an outer detector. The time can be either the time a particle enters or leaves the TPC. It represents the time when the ionization starts and the electron cloud starts to drift towards the anode.

The waveform of a pad signal needs to be non-saturated. This is necessary for the longitudinal diffusion coefficient since the fit to determine the width does not work

Table 5.2.: Used Monte Carlo samples from production 6.

run	number of subruns	P0D Water
91200000	21	out
91200001	31	out
91200002	31	out
91200010	29	out
91200011	33	out
91200012	24	out
91200020	29	out
91200021	28	out
91200022	21	out
91200030	25	out
91200031	27	out
91200032	21	out
91410000	56	in
91410001	56	in
91410002	55	in
91410003	56	in

properly on saturated waveforms and gives a wrong result. For the transverse diffusion coefficient a saturated waveform gives too low charge for a pad as it only reaches the saturated value at the maximum. Because of this, not only the charge on the pad is reconstructed incorrectly but also the sum of the charge. Therefore, the whole cluster is rejected for the analysis, if a waveform is saturated. For the determination of the longitudinal diffusion coefficient only the affected pad is rejected.

In the determination of the longitudinal diffusion coefficient only fit results with a maximum relative fit uncertainty of 10 % on the σ_{fit} fit parameter are used. Before filling these widths into the two-dimensional histogram they are corrected with the correction factor κ from chapter 4.1.

The output of the analytic fit of the charge, the variable `fitCharge`, needs to be below 380 A.U. and its standard deviation below 500 A.U. to be used in the determination of the transverse diffusion coefficient.

In addition, to reduce noise in the charge ratio distribution fit, only statistically relevant bins are used. That means only bins with a content larger or equal to the mean bin content of the whole two-dimensional histogram are considered.

For both diffusion coefficients the selected tracks have to pass a muon criteria to remove tracks with large fluctuation in the initial ionization. The advantage of using muons is the enhanced reconstruction performance, since they not only pass the whole gas vol-

Table 5.3.: Definition of the fiducial volume of the TPCs used in the analysis. The coordinates are given in mm.

	x	y	z
TPC 1	$[-870.0, 870.0]$	$[-930.0, 1030.0]$	$[-724.85, -71.15]$
TPC 2	$[-870.0, 870.0]$	$[-930.0, 1030.0]$	$[634.15, 1287.85]$
TPC 3	$[-870.0, 870.0]$	$[-930.0, 1030.0]$	$[1993.50, 2646.85]$

ume but also the surrounding detectors and, therefore, give a better T_0 to determine the drift distance. The muon is selected by a reconstructed transverse momentum p_t of the track in the range of $200\,\text{MeV} < p_t < 700\,\text{MeV}$ and the corrected charge `ccorr` in 200 A.U. < `ccorr` < 500 A.U..

Furthermore, only tracks are used which are approximately parallel to the pad plane. The angle ϑ between the track and the normal vector on the pad plane needs to fulfill the criterion $\cos(\vartheta) < 0.1$. For the determination of the transverse diffusion coefficient this restriction is extended. Here the tracks have to be nearly parallel to the z-direction to minimize the angular correction of y^*. The angle α between track and z-direction is chosen to match the criterion $\cos(\alpha) > 0.9$.

All used reconstructed clusters have to be in a fiducial volume which is defined in table 5.3. For the transverse diffusion coefficient this fiducial volume is later shrunk to reduce effects on the outer edges of the TPCs that are affected by electric and magnetic field distortions. The definitions are shown in chapter 5.1.4.3.

For the transverse diffusion parameter some further quality criteria are required. The relevant quantities are calculated in the reconstruction process of the ND280 framework. These quality criteria are the following:

- The uncertainty of the hit position in y is smaller than 0.25 cm.
- The uncertainty of the hit position in z is smaller than 0.2 cm.
- The spread of hits in z is smaller than 5.2 cm.

In addition to the determination of the diffusion coefficients the slow control data for temperature, pressure and electric field are collected for all selected tracks. From this the reduced electric field $E^* = {}^{ET}/_{p}$ is calculated and its average is used for the whole data set.

5.1.3. Results from Monte Carlo sample analysis

The analysis of Monte Carlo samples is used to review the measurement concepts to determine the diffusion coefficients. The longitudinal and the transverse diffusion coefficients are input parameters for the simulation and, therefore, they can be compared to the outcome of the analyses. The results give an estimation of the accuracy of the analyses.

5.1.3.1. Monte Carlo description

The Monte Carlo samples are produced from a list of physical processes which are occurring in the detector due to neutrino interactions. The output particles from these processes are then simulated and processed through a `GEANT4` detector simulation, which creates the primary ionizations in the TPCs. Following this, the active parts of each subdetector are simulated with the ND280 software package `elecSim`. The purpose of this software package is to create the output signals as given by the electronics of each subdetector.

In the `elecsim`-simulation of the Time Projection Chambers the primary ionizations produce electron clouds which drift to the anode due to the electric field. This drift is realized by calculating the mean path of the cloud and its arrival point at the anode. Afterwards the scattering of the cloud due to diffusion is calculated by the distance travelled in the gas and the predefined diffusion coefficients for longitudinal and transverse diffusion.

In contrast to simulation programs like `garfield++` the drift itself on the path through the detector is not simulated. The statistical variations in elecSim are simulated by random distributions taking into account the gaussian width of the cloud.

The signal of the drifted electron cloud is simulated as described in chapter 4.1. The simulated waveforms are produced by equation 4.2 with the smeared distribution of electrons. The resulting output is similar to the real raw data.

The signals are then processed in the same way as measured data. The raw data is first calibrated with the detector calibration framework which adjust gains and alignments. The calibrated hits in the TPCs are then used to reconstruct tracks. For the reconstruction of tracks and objects in the TPC the class `trexRecon` is used.

With this reconstructed data the analysis of longitudinal and transverse diffusion is performed as described in section 5.1.1. For general neutrino analyses the data is further processed to join reconstructed objects to analysis objects.

5.1.3.2. Longitudinal diffusion coefficient from Monte Carlo samples

The input longitudinal diffusion coefficient for the used Monte Carlo samples is

$$d_{l,\mathrm{MC}} = 290\,\frac{\mu\mathrm{m}}{\sqrt{\mathrm{cm}}}. \tag{5.5}$$

The determination of the longitudinal diffusion coefficient is done as described above.

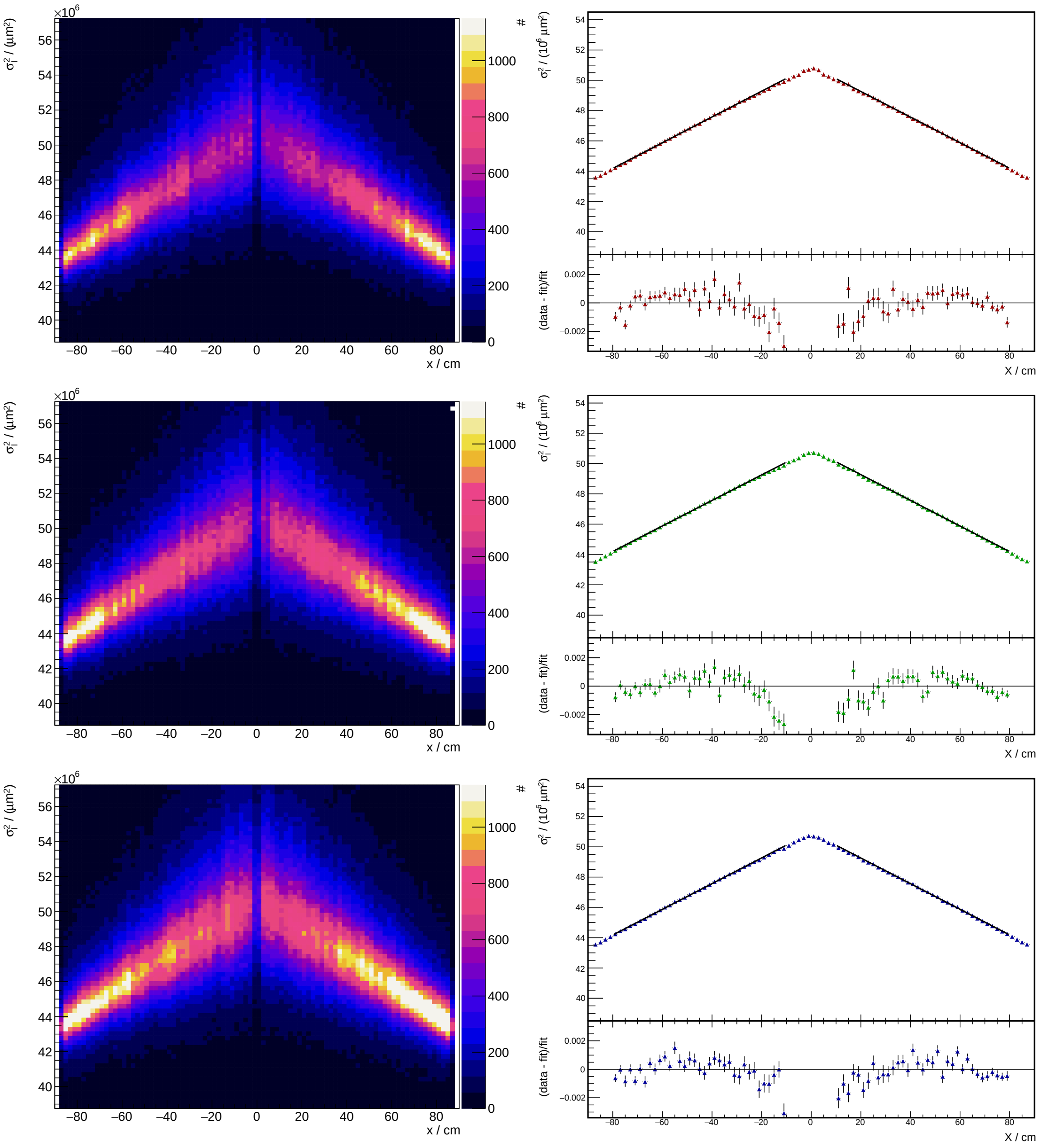

Figure 5.4.: Two-dimensional distributions of the squared width with respect to the x-coordinate in Monte Carlo samples on the left side and the mean squared width with respect to the x-coordinate on the right side. The width in the two-dimensional distribution is the result of the waveform fit. The mean squared width is evaluated by a slice fit to the two-dimensional distribution in bins of x. All three TPCs are shown, starting with TPC 1 at the top, TPC 2 in the middle and TPC 3 at the bottom.

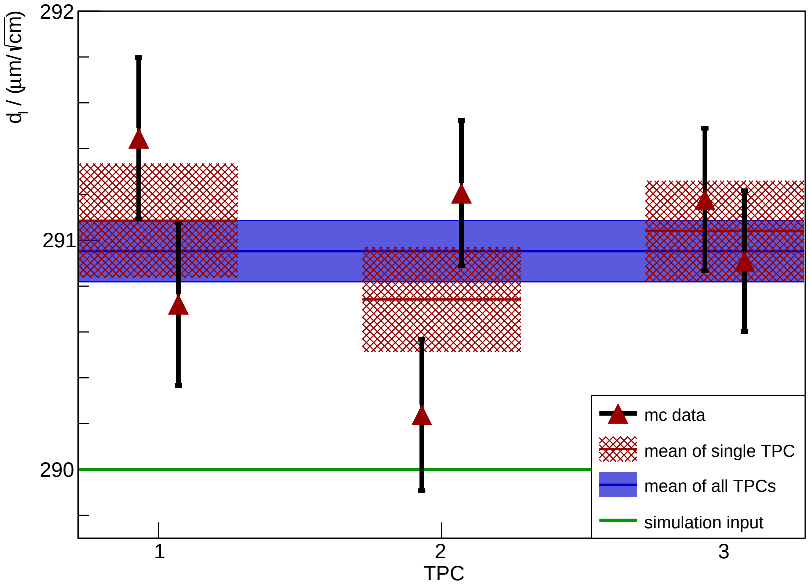

Figure 5.5.: Result for the longitudinal diffusion coefficient in ND280 with Monte Carlo samples.

The left side of figure 5.4 shows the two-dimensional distribution of the squared width with respect to the the drift coordinate x. It is clearly visible that there is a linear dependence of σ_l^2 on the drift distance on both sides of each TPC. To these two-dimensional distributions gaussian slice fits are performed. Their results are shown on the right side of figure 5.4. For both readout planes on each of the three TPCs the linear fit is performed and a longitudinal diffusion coefficient is extracted. The individual results are given in table 5.4.

All mean squared width distributions look very similar, because all pad planes are simulated with the same gain. This is also the reason for the symmetry of these distributions around the cathode at $x = 0$. As mentioned above, the offset has no influence on the diffusion coefficient and, therefore, is not further studied.

All results are shown in figure 5.5. The combination of all six individual measurements from all pad planes in the TPCs is

$$d_{l,\text{Meas.}} = (290.95 \pm 0,13)\,\frac{\mu\text{m}}{\sqrt{\text{cm}}}. \tag{5.6}$$

Compared to the input parameter the deviation is only +0.3 %. This shows that the concept to measure the longitudinal diffusion coefficient works quite well.

On the other side the result is more than seven standard deviations above the input value. Therefore, another correction factor is introduced to solve this deviation. It is defined as ratio of the Monte Carlo input and the combined result of the analysis

$$d_{l,\text{MC}} = \beta \cdot d_{l,\text{Meas.}}. \tag{5.7}$$

The bias correction value is $\beta = 0.9967$ and will be applied to the data result, too.

Table 5.4.: Results for the longitudinal and transverse diffusion coefficient measured in Monte Carlo data.

		TPC 1	**TPC 2**	**TPC 3**
d_l / (μm/$\sqrt{\text{cm}}$)	rp0	291.45 ± 0.35	290.24 ± 0.33	291.18 ± 0.31
	rp1	290.72 ± 0.35	291.21 ± 0.32	290.91 ± 0.31
	average	291.09 ± 0.25	290.74 ± 0.23	291.05 ± 0.22
	comb. average	290.95 ± 0.13		
d_t / (μm/$\sqrt{\text{cm}}$)	rp0	287.30 ± 1.86	286.18 ± 1.76	284.07 ± 1.71
	rp1	287.68 ± 1.82	286.38 ± 1.74	286.43 ± 1.67
	average	287.49 ± 1.30	286.28 ± 1.24	285.28 ± 1.19
	comb. average	286.29 ± 0.72		

5.1.3.3. Transverse diffusion coefficient from Monte Carlo samples

The transverse diffusion coefficient is determined as explained above in 5.1.1 for Monte Carlo samples with an input diffusion coefficient of

$$d_t = 286\,\frac{\mu\text{m}}{\sqrt{\text{cm}}}. \tag{5.8}$$

First, the charge ratio distributions in dependence of the drift coordinate x are created for all three TPCs from the selected tracks according to 5.1.2. To these two-dimensional charge ratio distributions the parameter σ_t is fitted using equation 5.3.
The results of these fits are shown in figure 5.6 for all TPCs represented by the squared mean sigma σ_t^2 as function of the x-coordinate. As expected from equation 5.4 σ_t^2 is linear for both sides of each TPC depending on the drift distance represented by x.
The transverse diffusion coefficients for every readout plane are determined. The results of these fits are shown in figure 5.7.
As for the longitudinal diffusion coefficient all initial widths σ_0 are in the same order as shown in figure 5.7. Unlike the determination of the longitudinal diffusion coefficient these offsets are not an impact of gain since the width is only evaluated from geometrical quantities. According to chapter 4.2.1 the signal of the smallest cloud is always the width of the pad itself.
It is visible that the mean diffusion coefficients for the single TPCs are decreasing with their distance to the center of the magnet. However, all results are in statistical agreement and, therefore, this is not investigated further at this point.
The combined average of all results is

$$d_{t,\text{Meas.}} = (286.29 \pm 0.72)\,\frac{\mu\text{m}}{\sqrt{\text{cm}}}. \tag{5.9}$$

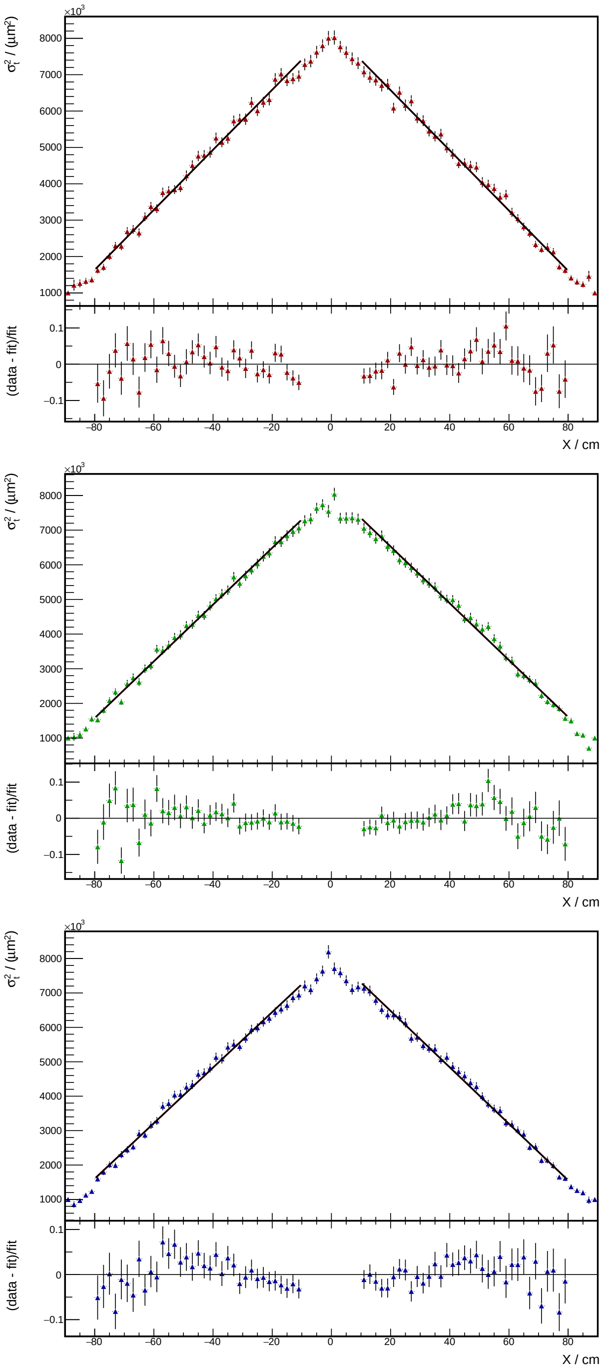

Figure 5.6.: Mean squared width σ_t^2 as function of the x-coordinate for all three TPCs from the analysis of Monte Carlo samples. TPC 1 is shown at the top, TPC 2 is in the middle and TPC 3 at the bottom.

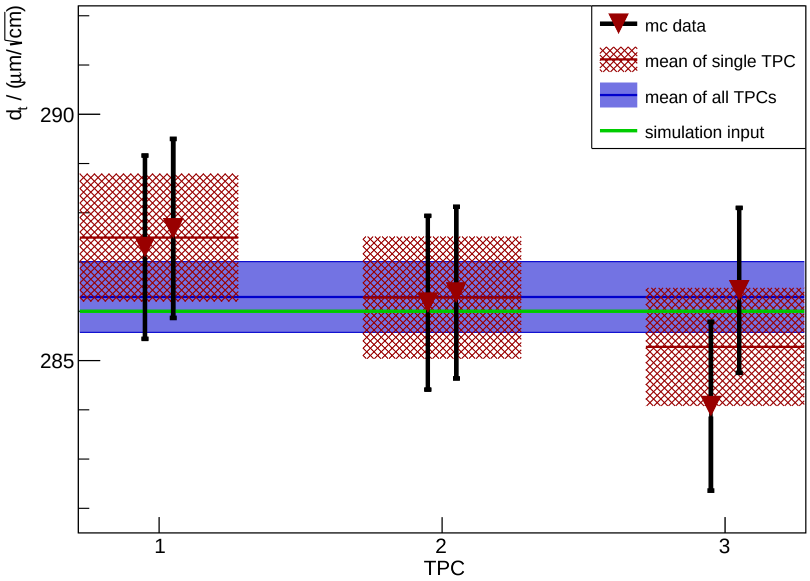

Figure 5.7.: Result for the transverse diffusion coefficient in ND280 with Monte Carlo samples.

All individual results for the pad planes are given in table 5.4. Since the combined result is in agreement with the input coefficient, no correction factor is introduced for the transverse diffusion coefficient.

5.1.4. Results from data analysis

This section describes the analysis of data samples recorded with the ND280 detector. The used data is described in section 5.1.2.

Unlike the analysis of Monte Carlo samples slow control data also need to be taken into account. From them a mean reduced electric field ET/p can be determined which enables a comparison of the measured diffusion coefficients with `MAGBOLTZ` simulations. Furthermore, only data samples with similar temperatures and pressures should be merged for theses analyses, because the diffusion coefficients strongly depend on these environmental changes as explained in chapter 3.

Apart from that, it will turn out that magnetic and electric field imperfections are not negligible and have an impact on the analysis of the transverse diffusion coefficients.

5.1.4.1. Slow control data

Since the diffusion coefficients depend on temperature and pressure, their fluctuations have to be small to get a reliable result with the applied measurement concept. As explained in chapter 3 the diffusion coefficients depend on the reduced electric field ET/p and the density T/p.

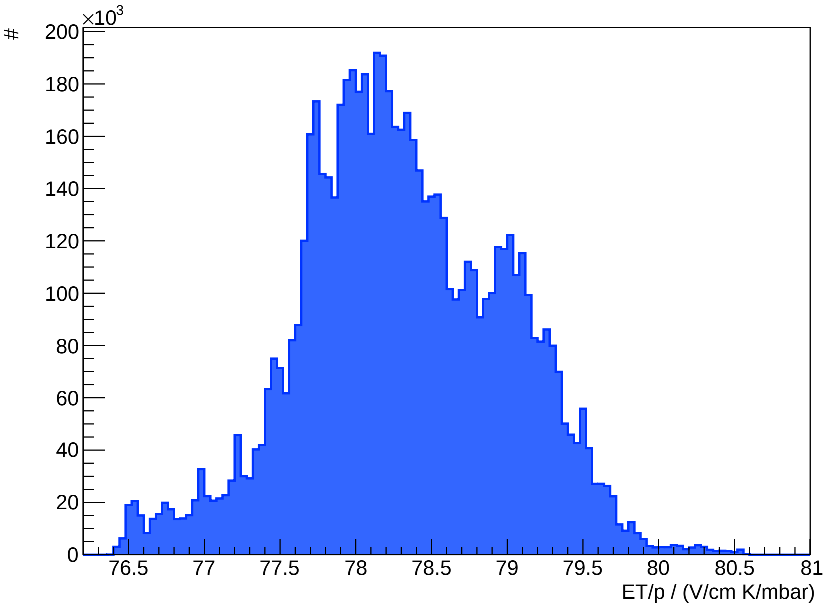

Figure 5.8.: Distribution of the reduced electric field ET/p for the analysed data samples.

In figure 5.8 the distribution of ET/p for the analysed T2K run is shown for all selected tracks. The mean of the distribution of the reduced electric field is

$$ET/p = (78.31 \pm 0.68)\,\frac{\mathrm{V}}{\mathrm{cm}} \cdot \frac{\mathrm{K}}{\mathrm{mbar}}. \tag{5.10}$$

The density has a mean of

$$T/p = (0.2850 \pm 0.0025)\,\frac{\mathrm{K}}{\mathrm{mbar}}. \tag{5.11}$$

These values are used for the `MAGBOLTZ` simulation of the diffusion coefficients.
The deviation of the drift velocity v_d is also reviewed, because it is used in the translation of the longitudinal width from a time signal to a drift length. This translation is done for every track with the drift velocity that was measured at this time. This drift velocity is measured with the gas monitoring chambers explained in chapter 2.3.2 and is used to calibrate the TPCs. The distribution of drift velocities for the analysed tracks is shown in figure 5.9. The mean drift velocity is

$$v_d = (78.44 \pm 0.06)\,\frac{\mu\mathrm{m}}{\mathrm{ns}} \tag{5.12}$$

and matches the design value.
Furthermore, the evolution of temperature and pressure is scanned for irregularities which may need to be excluded from the analysis. As shown in figure 5.10, both temperature and pressure do not show any larger fluctuations. In chapter B.1 the temperature distributions for the single TPCs are shown. Even in comparison between the single TPCs no larger deviation are found.

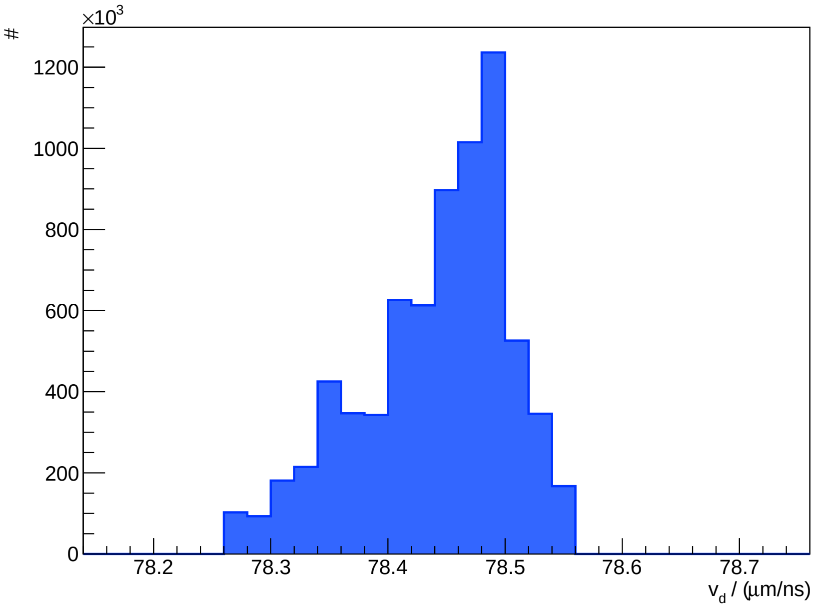

Figure 5.9.: Distribution of the drift velocity v_d which is used in the diffusion analysis.

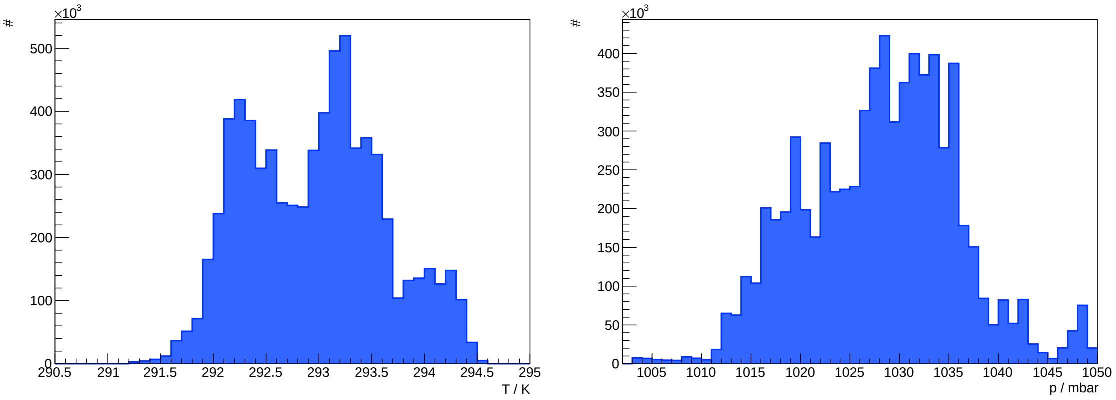

Figure 5.10.: Distributions for temperature on the left side and pressure on the right side.

5.1.4.2. Longitudinal diffusion coefficient from data analysis

The longitudinal diffusion coefficient is determined as explained in section 5.1.1. The two-dimensional distributions of the squared longitudinal width in dependence oo the x-coordinate are shown in figure 5.11 for each TPC. The width is determined by fitting the waveforms. From the two-dimensional distribution the mean squared width is determined by performing gaussian slice fits in slices of the x-coordinate. The results of these slice fits for each TPC are shown in figure 5.11 on the right side. For each readout plane these mean squared width functions show a linear dependence on x which is fitted using equation 5.1. This fit is used to determine the longitudinal diffusion coefficient for each of the readout planes. The results are given in table 5.5.

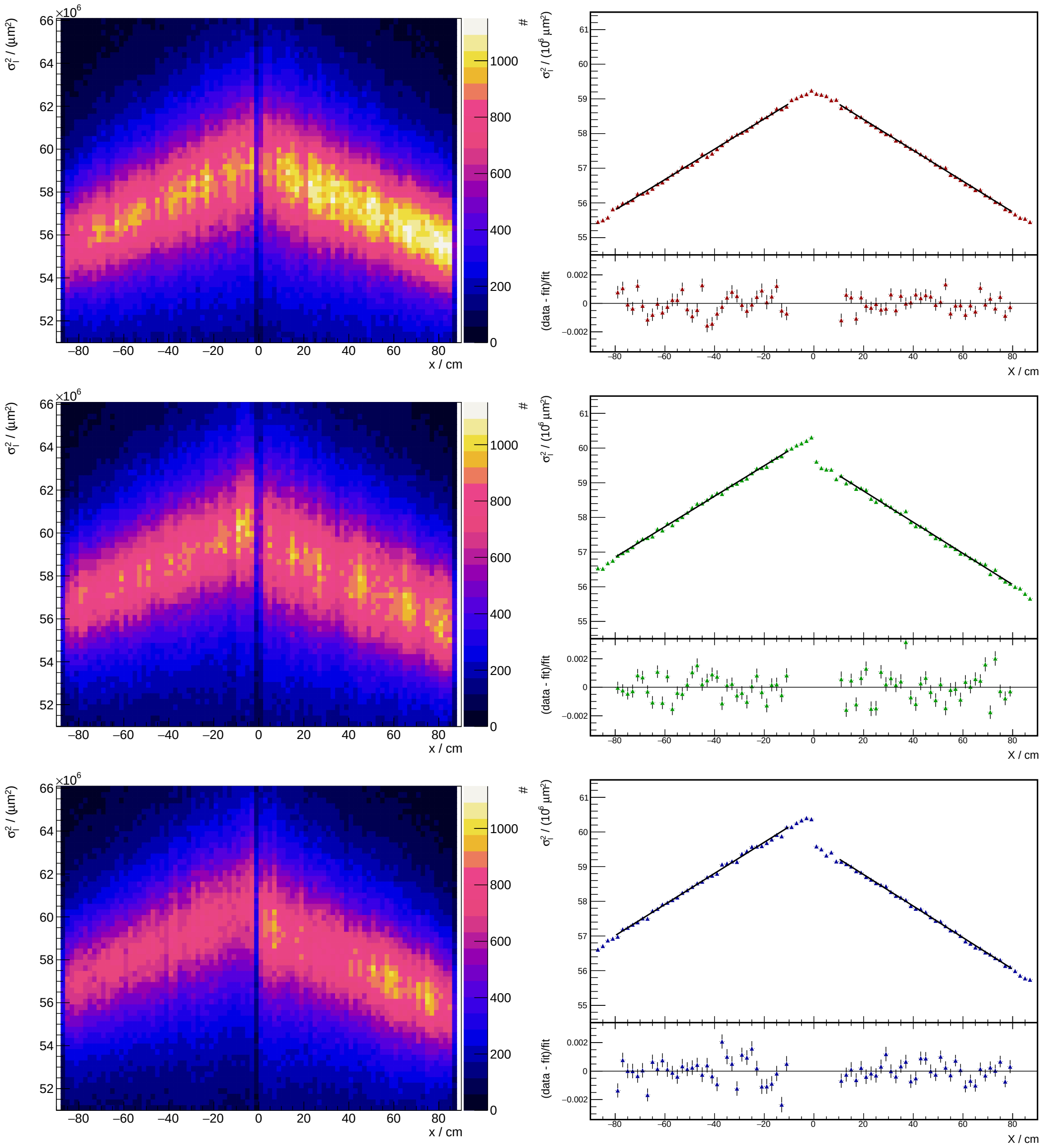

Figure 5.11.: Two-dimensional distributions of the squared width in dependence on the x-coordinate on the left side and the mean squared width in dependence of the x-coordinate on the right side. All three TPCs are shown. TPC 1 is at the top, TPC 2 in the middle and TPC 3 at the bottom.

Table 5.5.: Results of the analysis of ND280 data samples for the longitudinal diffusion coefficient.

		without β correction $d_l/(\mu\mathrm{m}/\sqrt{\mathrm{cm}})$	**with β correction** $d_l/(\mu\mathrm{m}/\sqrt{\mathrm{cm}})$
TPC 1	rp0	209.32 ± 0.53	208.63 ± 0.53
	rp1	210.95 ± 0.47	210.25 ± 0.47
	average	210.23 ± 0.35	209.54 ± 0.35
TPC 2	rp0	209.68 ± 0.53	208.99 ± 0.53
	rp1	212.15 ± 0.54	211.45 ± 0.54
	average	210.89 ± 0.38	210.19 ± 0.38
TPC 3	rp0	211.73 ± 0.59	211.03 ± 0.59
	rp1	213.20 ± 0.52	212.50 ± 0.52
	average	212.58 ± 0.39	211.90 ± 0.39
average		211.15 ± 0.21	210.45 ± 0.21

The six readout planes all show different offsets. These offsets occur due to different amplification voltages on the MicroMeGaS for each of the six readout planes which causes a different gain. Since this is not affecting the slope for drift distances in the analysed ranges, the offset can be neglected.

The results for the longitudinal diffusion coefficient from the six readout planes are shown in figure 5.12. The individual results are depicted as data points with statistic uncertainty as well as the combination of statistic and systematic uncertainty. The red shaded areas show the weighted mean for each of the three TPCs from both readout planes with their statistical uncertainty. The red line in the middle represents the mean value. The blue area represents the mean result for the longitudinal diffusion coefficient which is calculated from all six readout planes with the mean value as dark blue line in the middle. All results from analysed data are corrected with the β correction factor according to equation 5.7.

For comparison, the longitudinal diffusion coefficient from `MAGBOLTZ` simulations is additionally depicted as a green band. The mean value is represented by the dark green line. This value belongs to a reduced electric field of

$$ET/p = (78.31 \pm 0.68)\,\frac{\mathrm{V}}{\mathrm{cm}} \cdot \frac{\mathrm{K}}{\mathrm{mbar}} \tag{5.13}$$

and is scaled in respect to the gas density with

$$T/p = (0.2850 \pm 0.0025)\,\frac{\mathrm{K}}{\mathrm{mbar}}. \tag{5.14}$$

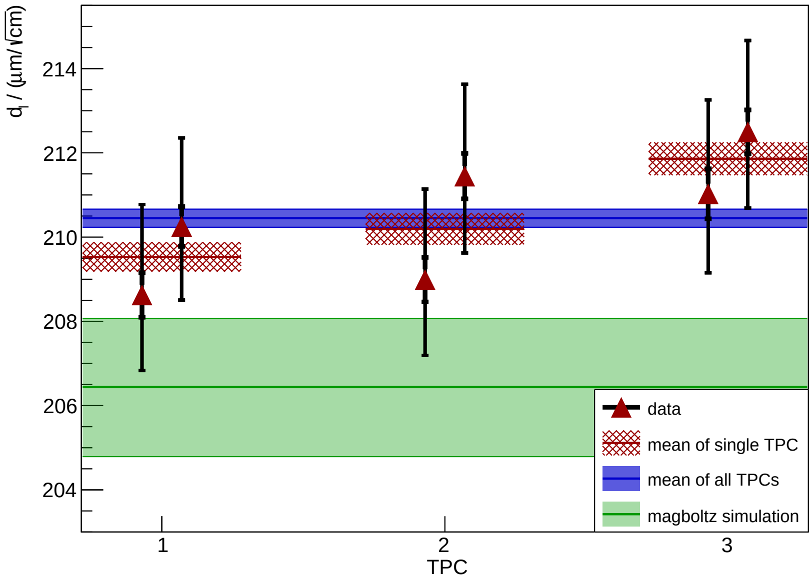

Figure 5.12.: Result for the longitudinal diffusion coefficient from the analysis of ND280 data samples. Results for all three TPCs including both readout planes are shown and compared to the MAGBOLTZ simulation value for the designated ET/p value.

The uncertainty band consists of statistical and systematic uncertainties. The designated longitudinal diffusion coefficient evaluated from MAGBOLTZ simulation is

$$d_{l,\mathrm{sim.}} = (206.44 \pm 0.61\,(\mathrm{stat.})\,^{+1.51}_{-1.55}\,(\mathrm{sys.}))\,\mu\mathrm{m}/\sqrt{\mathrm{cm}}. \tag{5.15}$$

The combined result for the longitudinal diffusion coefficient from the three TPCs of ND280 is

$$d_l = (210.45 \pm 0.21\,(\mathrm{stat.})\,^{+1.74}_{-1.19}\,(\mathrm{sys.}))\,\mu\mathrm{m}/\sqrt{\mathrm{cm}} \tag{5.16}$$

and is about four standard deviations above the simulation value of MAGBOLTZ including the systematic uncertainties. The statistical accuracy of the individual measurements is between 2 ‰ and 3 ‰ which yields the combined result of 1.2 ‰. This statistical accuracy is far below the total systematic uncertainty of +7.8 ‰ / −6.1 ‰. The systematic uncertainty consists of the reconstruction of the x-coordinate, the drift velocity and the uncertainties of the correction factors κ and β. Their individual contributions are explained in the following.

The impact of the reconstruction resolution of the x-coordinate is determined by truth information in Monte Carlo samples. This is done by using the real x-coordinate of the track instead of the reconstructed one. The individual results for the TPCs are then compared to the results with the reconstructed x-coordinate. The maximum difference between both is taken as systematic uncertainty for the x-reconstruction. It is found to be +0.5 ‰ / −1.1 ‰.

Table 5.6.: Systematic uncertainties for the longitudinal diffusion coefficient.

source	**systematic uncertainty**
x-reconstruction	$+0.5$ ‰ / -1.1 ‰
drift velocity v_d	$+6.6$ ‰ / -4.0 ‰
κ-correction (sys.)	$+3.6$ ‰ / -3.8 ‰
κ-correction (stat.)	$+0.9$ ‰ / -1.6 ‰
β-correction	± 1.7 ‰
combined	$+7.8$ ‰ / -6.1 ‰

The systematic uncertainty of the determination of the drift velocity also contributes to the uncertainty of the diffusion coefficient, because the drift velocity is used to transfer the width of a signal in time to width in length. Due to uncertainty propagation the relative uncertainty is $\Delta d_l / d_l = \Delta v_d / v_d$ with a relative uncertainty for the drift velocity of $\Delta v_d / v_d = +6.6$ ‰ / -4.0 ‰. This is the systematic uncertainty for the measurement with the gas monitoring chambers and is derived in 6.7.1.
The correction factor κ for the shaping of the AFTER-chip introduces two single contributions to the systematic uncertainty of the longitudinal diffusion coefficient. On the one hand the introduction of this calibration is assumed to have an uncertainty of 25 % as by $\Delta\kappa/\kappa(\text{sys.}) = 0.25 \cdot (1-\kappa)/\kappa$. By shifting κ with this uncertainty a deviation of the results between $+3.6$ ‰ and -3.8 ‰ is observed. On the other hand the statistical uncertainty given in chapter 4.1.2 also contributes to the systematic uncertainty, which is again determined by shifting κ, which results in a contribution of $+0.9$ ‰ / -1.6 ‰.
The bias correction β, which corrects the result of the Monte Carlo sample analysis to their input value, is assumed to have an uncertainty of 50% with $\Delta\beta = 0.5 \cdot (1-\beta)$. This uncertainty is contributing to the systematic uncertainty of the longitudinal diffusion coefficient by $\Delta d_l / d_l = \Delta\beta/\beta = \pm 1.7$ ‰. All systematics are summarized in table 5.6.

5.1.4.3. Transverse diffusion coefficient from data analysis

The transverse diffusion coefficients for the TPCs are determined by the method described in 5.1.1. Using the full fiducial volumes, the functional dependences between the mean squared transverse width σ_t^2 and the drift coordinate x were found out as shown in figure 5.13 on the left side. The predicted linear dependence is broken in the middle of both readout sides of the drift volumes for TPC 1 and TPC 2. Comparing the results for the transverse diffusion coefficients from the linear fits of TPC 3 with one of the other two TPCs, an increase is observed. This increase can not be explained by the kink in linearity. The fit results are given in table 5.7.
It is presumed that these kinks arising in TPC 1 and TPC 2 are originating from electric field distortions on the walls of the TPCs. Therefore, the fiducial volume of each of the three TPCs is shrunk by half in the z-dimension. The new fiducial volume is placed in

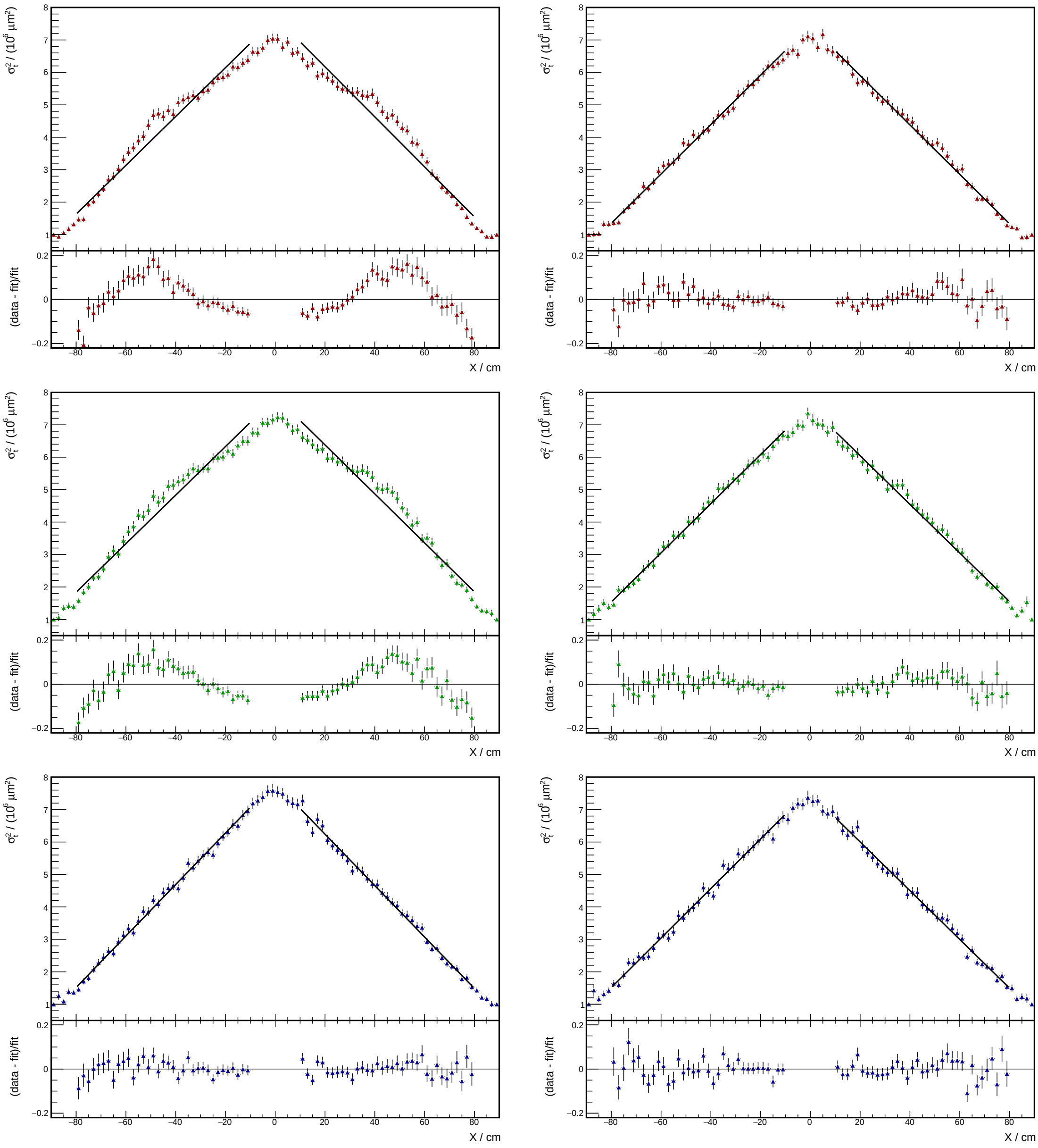

Figure 5.13.: Mean squared transverse width σ_t^2 as function of the drift coordinate x determined in data samples for each TPC. TPC 1 is shown at the top, TPC 2 in the middle and TPC 3 at the bottom. On the left side the results for the mean squared transverse width of the analysis of the full fiducial volume is depicted, on the right side the results of the analysis of the shrunk fiducial volume.

Table 5.7.: Results of the analysis of ND280 data samples for the transverse diffusion coefficient. Results are given for two different fiducial volumes.

		full fiducial volume $d_t/(\mu\text{m}/\sqrt{\text{cm}})$	**shrunk fiducial volume** $d_t/(\mu\text{m}/\sqrt{\text{cm}})$
TPC 1	rp0	274.25 ± 1.77	275.93 ± 1.75
	rp1	277.49 ± 1.71	275.89 ± 1.74
	average	275.93 ± 1.23	275.91 ± 1.23
TPC 2	rp0	273.61 ± 1.93	275.24 ± 1.97
	rp1	274.70 ± 1.94	273.65 ± 1.93
	average	274.15 ± 1.37	274.43 ± 1.38
TPC 3	rp0	281.69 ± 1.85	276.33 ± 2.07
	rp1	281.47 ± 1.84	274.02 ± 2.03
	average	281.58 ± 1.30	275.15 ± 1.45
average		277.27 ± 0.75	275.22 ± 0.78

the middle of the old fiducial volume. Even though the kink is not occurring in TPC 3, the same reduction of fiducial volume is done there. It is possible that TPC 3 also suffers from magnetic field distortion, since it is placed close to the edge of the magnetic coil. With the reduction of its fiducial volume the possible exposure to magnetic field distortion should be also reduced. The new fiducial volumes are given in table 5.8.
The functional dependencies between σ_t^2 and x, achieved with the new fiducial volumes, are shown in figure 5.13 on the right side. The results show a linear dependence as predicted by equation 5.4 and the kinks are not occurring anymore. All extracted transverse diffusion coefficients determined by the fit are now in agreement with each other. The results are given in table 5.7. The results for the new fiducial volumes are also in agreement with those with the full fiducial volumes of TPC 1 and TPC 2.
The reason the kinks are not appearing in the analysis of Monte Carlo samples with full fiducial volume is that the field distortions are not sufficiently simulated in `elecSim`. On the one hand the drift itself is not simulated as explained in 5.1.3.1, on the other hand these field distortions are not known precisely enough and their parametrization is fairly complex.
The results from the analysis of the shrunk fiducial volume are shown in figure 5.14. The individual results for each readout plane are shown as data points and the mean values with their statistical uncertainty for each TPC are shown as shaded red area with the line representing the mean value. Statistical and systematic uncertainties are shown for each data point. The smaller but thicker error bars represent the statistical uncertainties and the bigger thinner error bars the combination of statistical and systematic uncertainties. The blue line illustrates the mean value for all six results

Table 5.8.: Coordinates for the shrunk fiducial volume of the TPCs used to determine the transverse diffusion coefficient. The coordinates are given in mm.

	x	y	z
TPC 1	$[-870.0, 870.0]$	$[-930.0, 1030.0]$	$[-561.5, -234.5]$
TPC 2	$[-870.0, 870.0]$	$[-930.0, 1030.0]$	$[797.5, 1124.5]$
TPC 3	$[-870.0, 870.0]$	$[-930.0, 1030.0]$	$[2156.8, 2483.5]$

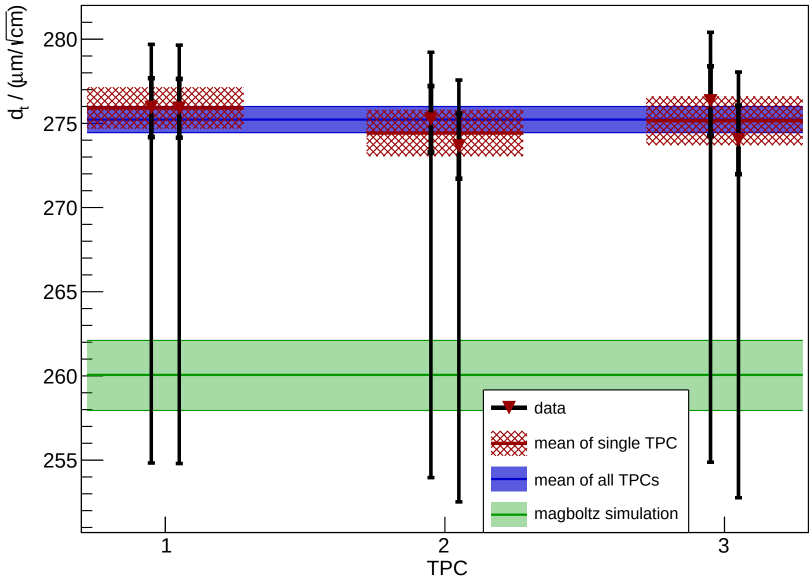

Figure 5.14.: Result for the transverse diffusion coefficient from ND280 data samples.

with the blue area as its statistical uncertainty. The green band shows the result of the `MAGBOLTZ` simulation for

$$ET/p = (78.31 \pm 0.68)\,\frac{\mathrm{V}}{\mathrm{cm}} \cdot \frac{\mathrm{K}}{\mathrm{mbar}} \tag{5.17}$$

and

$$T/p = (0.2850 \pm 0.0025)\,\frac{\mathrm{K}}{\mathrm{mbar}} \tag{5.18}$$

with its statistical and systematic uncertainties. The systematic uncertainty consists of the uncertainty of ET/p as well as of the scaling with the density T/p.
The mean value of the transverse diffusion coefficient for all six TPC readout planes is

$$d_t = (275.22 \pm 0.78\,(\mathrm{stat.})^{+2.00}_{-19.30}\,(\mathrm{sys.}))\,\frac{\mu\mathrm{m}}{\sqrt{\mathrm{cm}}}. \tag{5.19}$$

The `MAGBOLTZ` simulation results in

$$d_{t,\mathrm{sim.}} = 260.06 \pm 0.72\,(\mathrm{stat.})^{+1.33}_{-1.39}\,(\mathrm{sys.}))\,\frac{\mu\mathrm{m}}{\sqrt{\mathrm{cm}}}. \tag{5.20}$$

Table 5.9.: Systematic uncertainties for the transverse diffusion coefficient.

source	**systematic uncertainty**
x-reconstruction	+7.2 ‰ / −4.3 ‰
y-reconstruction	+0.0 ‰ / −70.0 ‰
$\cos(\alpha)$-reconstruction	+1.1 ‰ / −0.9 ‰
combined	+7.3 ‰ / −70.1 ‰

Given by the large systematic uncertainty of the measurement to lower values of −70 ‰, data and Monte Carlo samples still agree within the given uncertainty. The systematic uncertainty to higher values is 7.3 ‰.

The large systematic uncertainty to lower values mostly consists of the resolution of the y-coordinate of a track. It is estimated from the spatial resolution from [17, fig. 25]. It is assumed that the resolution is 0.7 mm at worst for tracks reconstructed with at least two pads. The y-coordinate is smeared with this resolution and the analysis is rerun. For the six results of the individual readout planes a deviation between −70 ‰ to −140 ‰ from the results without smearing is detected. Considering that the spatial resolution for shorter tracks improves to 0.4 mm, it is decided to use the half of the maximum deviation, which is 70 ‰, as systematic uncertainty. One reason all results with a smeared y are lower than without smearing is that the smearing enlarges the charge distribution in dependence of y^*. This flattens the linear dependence of the σ_t^2 to x which results in a smaller diffusion coefficient.

Other contributions to the systematic uncertainties are the determination of the drift coordinate x and the angle between the track and the beam direction $\cos(\alpha)$. Both uncertainties are determined by using the true values of the track given in Monte Carlo samples. The maximum difference of both methods is used as systematic uncertainty. The maximum difference resulting from the analysis using the true x is +7.2 ‰ / −4.3 ‰, while for the true track angle $\cos(\alpha)$ a maximum difference of +1.1 ‰ / −0.9 ‰ is found. All systematic uncertainties are summarized in table 5.9.

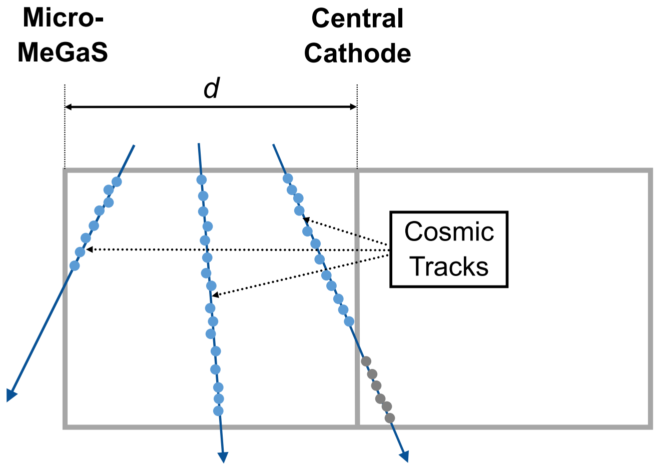

Figure 5.15.: Schematic illustration for the measurement of the drift velocity with the TPCs.

5.2. Drift velocity measurements

For reconstructing tracks in the TPCs the drift velocity is needed. It is used as calibration for the TPCs in ND280 and is measured with the gas monitoring chambers described in 2.3.2. By measuring the drift velocity continuously, changes generated by temperature and pressure fluctuation can be compensated.
Besides the measurement with the GMCs, it is possible to measure the drift velocity with the TPCs themselves. For this, cosmic tracks are used that cross the MicroMeGaS or the central cathode.

5.2.1. Measurement concept

To measure the drift velocity a program from the former `tpcCalib` package of the ND280 software is used. The used revision of `tpcCalib` is v0r4. This program collects the arrival times of electrons from all tracks triggered by the *fgd cosmic trigger* drifting to the MicroMeGaS. To determine the drift velocity the method introduced by A. Gaudin in [29] is used.
Figure 5.15 shows a sketch of a TPC. The incoming cosmic tracks create electron clouds by ionization represented by the blue dots. These electron clouds drift to the MicroMeGaS and create a signal. The time between the track crossing the TPC and the arrival of this signal is then used as arrival time. The start time for the track is T_0 and is given by the FGD detector. Electron clouds created directly in front of the MicroMeGaS have almost no distance to travel and, therefore, the shortest arrival time. If an elec-

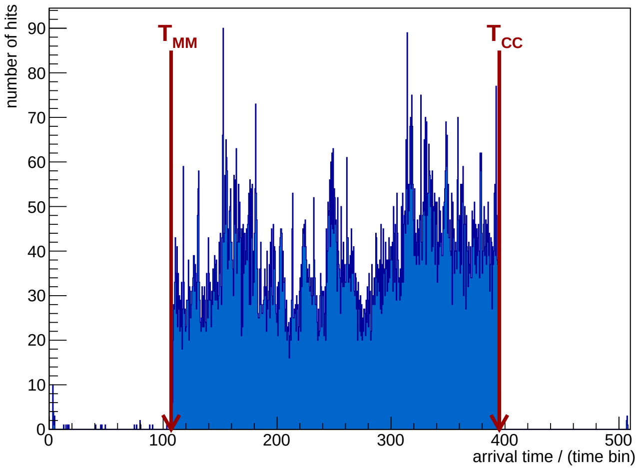

Figure 5.16.: Distribution of the electron arrival times from cosmic tracks going through TPC 1 readout plane 0 in the sector of MicroMeGaS number 6. From the edges of this distribution the minimal and maximal drift time is extracted to measure the drift velocity.

tron cloud is created directly at the central cathode it has the longest way d to travel. This results in the largest arrival time.

From the distribution of the arrival times for each MicroMeGaS module the difference in arrival times $\Delta t_{arrival}$ is extracted:

$$\Delta t_{arrival} = t_{CC} - t_{MM}. \tag{5.21}$$

The arrival time given by tracks crossing the central cathode is t_{CC} and for MicroMeGaS t_{MM}. One of these arrival time distributions is exemplarily shown in figure 5.16. Both arrival times are determined by the cut-offs of the distribution. All entries between these cut-offs are tracks going through the TPC.

The drift velocity is then calculated using equation 5.22 with the maximum drift distance $d = 89.75\,\text{cm}$, which is the distance between MicroMeGaS and cathode, and $\Delta t_{arrival}$.

$$v_d = \frac{d}{\Delta t_{arrival}} \tag{5.22}$$

5.2.2. Data selection

For the measurement of the drift velocity data samples from T2K Run 4 are used. This is the same run which is analysed to measure the diffusion coefficients in 5.1. Corresponding ND280 run numbers are given in table 5.10. The data was taken between October 2012 and April 2013. As opposed to the determination of the diffusion coefficient only samples with cosmic triggers are used to measure the drift velocity.

Table 5.10.: Run numbers for the drift velocity measurement with ND280

T2K-Run	**ND280-Run**	**Dates**
4	9000 - 9088	19.10.2012 - 12.11.2012
4	9128 - 9216	21.11.2012 - 12.12.2012
4	9400 - 9699	18.01.2013 - 01-04-2013

For the collection of the arrival times all tracks crossing one of the TPCs are used and sorted by the MicroMeGaS modules. No other cuts are used for this analysis.
In addition to the drift velocity measurement with the TPCs, the measurements with the GMCs, which were recorded in this period, are considered. Only measurements from chamber A are used. This chamber is positioned in the return line of the gas circuit. Measurements with a larger uncertainty than 0.5 μm/ns are rejected.

5.2.3. Results for the drift velocity

The drift velocity is measured for every individual MicroMeGaS module from which the mean drift velocity is calculated for each readout plane of a TPC. The individual results for the MicroMeGaS modules on each TPC are shown in figure 5.17.
The individual results for TPC 1 have no large deviations between each other. The results for the readout planes seem to be very flat with no indication of any systematic shift in one region along the MicroMeGaS plane. Comparing both readout planes the mean for readout plane 0 is slightly higher than for readout plane 1 with a deviation of only 0.0221 μm/ns. The readout planes are defined in figure 5.1.
For TPC 2 both readout planes again look similar to each other but the velocities for the top and bottom row modules of the MicroMeGaS are slightly increased. The mean values in the middle of the readout plane are smaller than for TPC 1. This could be an effect caused by electric or magnetic field distortions, however, this can not be investigated further with the available data. For TPC 2 both mean values for the readout planes are in agreement with each other and have significantly larger statistical uncertainties as compared to TPC 1.
The individual results for TPC 3 are different for each readout plane. They are on average higher for readout plane 0 and lower for readout plane 1 in comparison to TPC 1. This is may be caused by edge field effects of the magnet, because TPC 3 is located at the end of the magnetic coil. Angles between the magnetic and the electric field can change the drift velocity, even though a parallel magnetic field has no influence on the drift velocity. The mean values for both readout planes have a large discrepancy of nearly 0.1 μm/ns between each other.
Figure 5.18 shows the combination of the MicroMeGaS modules for each readout plane as data points. In addition, the mean drift velocity for each TPC as well as the combination of all of them is shown. As already mentioned, the mean results for the readout

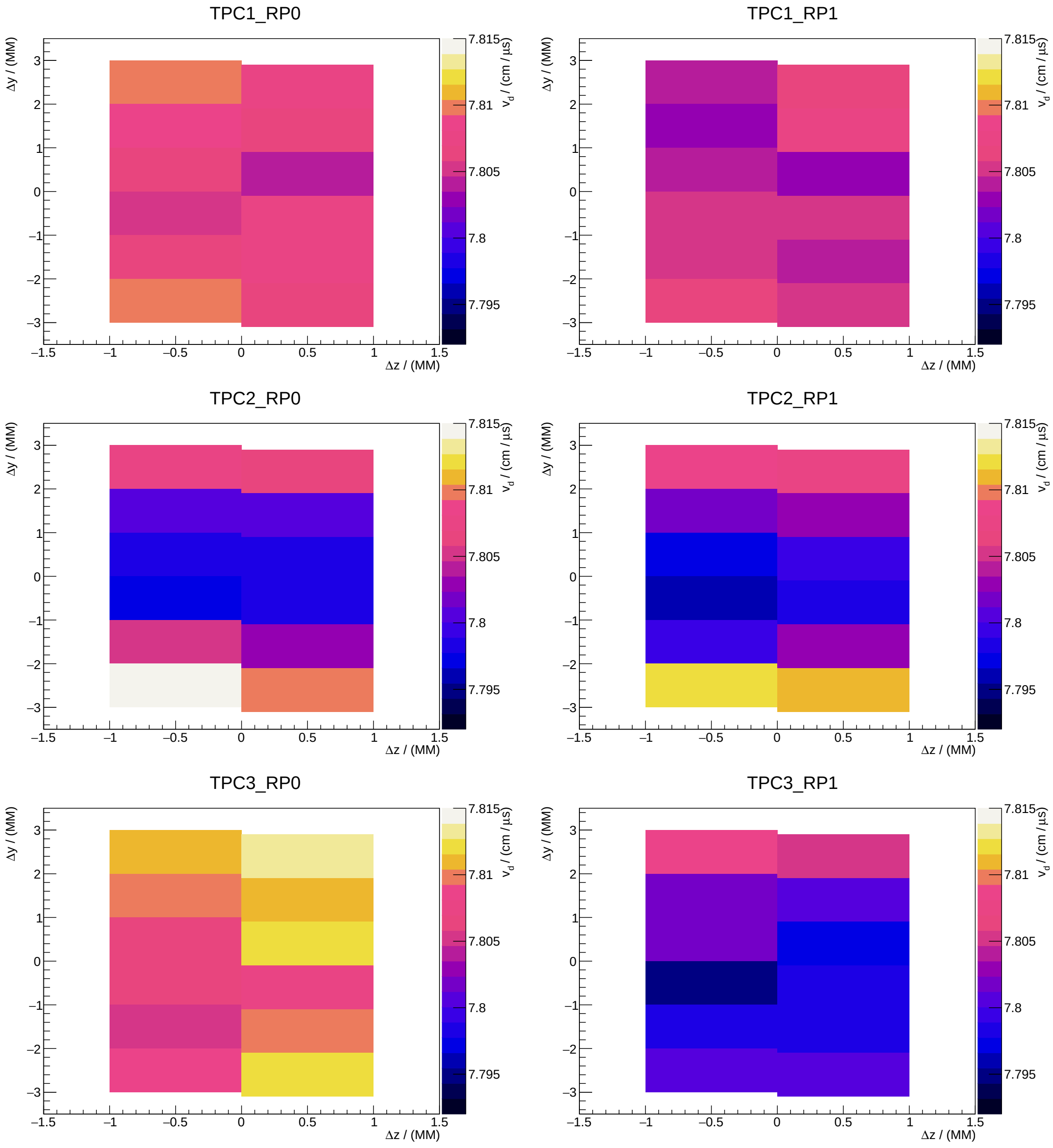

Figure 5.17.: Drift velocity results by individual MicroMeGaS in all TPCs. The z-axis scaling is the same for all plots for comparison.

planes are not well consistent. Still all of them agree within 0.1 μm/ns. The combined mean for the drift velocity of all six readout planes is

$$v_{d,\mathrm{comb.}} = (78.0712 \pm 0.0004\,(\mathrm{stat.}) \pm 1.9518\,(\mathrm{sys.}))\,\frac{\mu\mathrm{m}}{\mathrm{ns}}. \tag{5.23}$$

The systematic uncertainty is not given in [29]. Here it is estimated to be 2.5 %. It is assumed that the maximum drift distance between the MicroMeGaS modules and the central cathode has an accuracy of least $\sigma_d = \pm 1\,\mathrm{mm}$. The determination of t_{CC} and

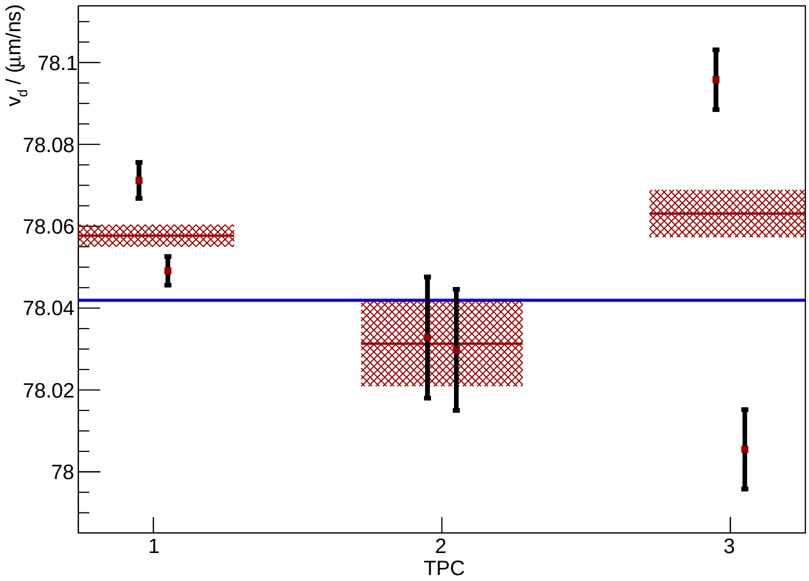

Figure 5.18.: Result for the drift velocity measured with the ND280 TPCs.

t_{MM} should have a precision of $\sigma_t = \pm 5$ time bins at least. Given a Δt of the order of 300 time bins, the systematic uncertainty of Δt is 2.4 %.
The measured result is four to five standard deviations below the value determined from `MAGBOLTZ` simulations

$$v_{d,\text{sim.}} = 78.5185 \pm 0.0401\,(\text{stat.})^{+0.0515}_{-0.0581}\,(\text{sys.})\,\frac{\mu\text{m}}{\text{ns}}. \tag{5.24}$$

Within the uncertainties, measurement and simulation values are consistent. The mean value for the drift velocity measured with the gas monitoring chambers for T2K Run 4 is

$$v_{d,\text{GMC}} = (78.422 \pm 0.008\,(\text{stat.})^{+0.518}_{-0.314}\,(\text{sys.}))\,\frac{\mu\text{m}}{\text{ns}}. \tag{5.25}$$

Figure 5.19 shows all GMC measurements of the drift velocity. The red data points are used to calculate the mean value. Measurements with too high statistic uncertainties are not used. The result of the GMC measurement is in statistical agreement with the `MAGBOLTZ` simulation. In addition it is still compatible with the measurement with the ND280 TPCs because of the systematic uncertainties. The systematic uncertainty for a single measurement of the GMCs is +6.6 ‰/ − 4.0 ‰ as shown in chapter 6.7.1.

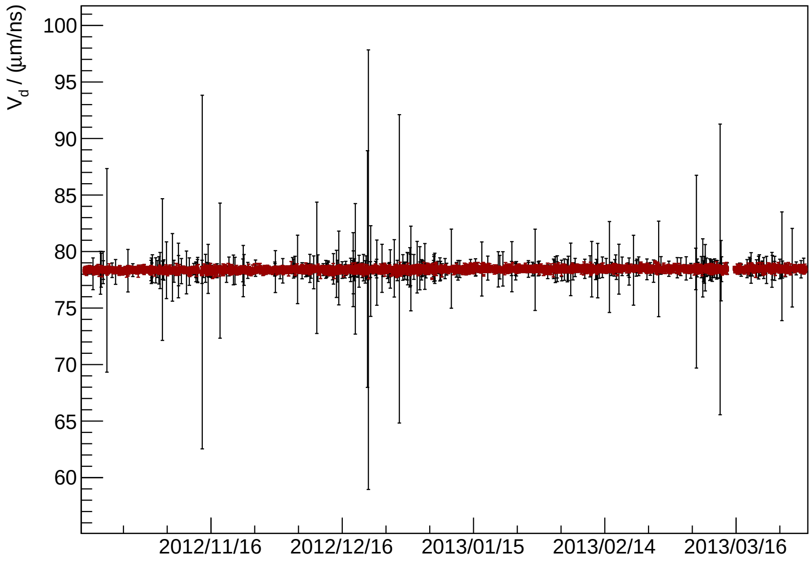

Figure 5.19.: Drift velocity measurements from the gas monitoring chambers for the time from the analysed TPC data.

5.3. Fitting the gas mixture

The results achieved with the ND280 TPCs for the drift velocity and the two diffusion coefficients are used to determine the gas mixture using a χ^2 fit. For that, the measurements are compared to simulations with different gas mixtures. The most probable gas mixture is the mixture with the minimal χ^2-value. The designed gas mixture of T2K consists of 95 % argon (Ar), 3 % tetrafluoromethane (CF_4) and 2 % isobutane (iC_4H_{10}) in volume fractions.

`MAGBOLTZ` simulations for different variations of the designated gas mixture are used as comparison values. The simulations are performed for mixtures with fractions of 1.00 % to 3.50 % of tetraflouromethane and 0.75 % to 2.75 % of isobutane in steps of 0.05 % each, where the remaining fraction is argon. These simulated curves for the diffusion coefficients and the drift velocity are fitted with the functions from chapter 3. From the fitted functions the expectation values are determined at

$$ET/p = (78.31 \pm 0.68)\,\frac{\mathrm{V}}{\mathrm{cm}} \cdot \frac{\mathrm{K}}{\mathrm{mbar}}. \tag{5.26}$$

The simulated magnetic field for all simulations is $B = 0.20\,\mathrm{T}$. Therefore, the values for the transverse diffusion coefficients need to be scaled to the magnetic field of $B = 0.2048\,\mathrm{T}$ which is applied to the TPCs in ND280. Running new simulations with the exact magnetic field is not feasible due to the huge amount of computing time needed for that.

The scaling parameter for the transverse diffusion coefficient is estimated from five simulations with exact magnetic field that are compared to the simulation with a magnetic field of $B = 0.2\,\mathrm{T}$. From that a maximum deviation of 1 % is derived. In consequence the transverse diffusion coefficients determined for the χ^2-fitting are shifted down by 1 % and a systematic uncertainty of 0.5 % introduced by this correction is assumed. The values of the longitudinal diffusion coefficient and the drift velocity do not need to be scaled since they do not change with a magnetic field applied parallel to the electric field.

For every gas mixture with the fractions of CF_4 (i) and iC_4H_{10} (j) the $\chi^2_{O,i,j}$ for the drift velocity and the two diffusion coefficients are calculated according to

$$\chi^2_{v_d,i,j} = \frac{(v_{d,\mathrm{Meas.}} - v_{d,\mathrm{sim.},i,j})^2}{\sigma^2_{\mathrm{Meas.,\,stat.}} + \sigma^2_{\mathrm{Meas.,\,sys.}} + \sigma^2_{\mathrm{sim.},i,j}}, \text{and } d_l,\ d_t \text{ accordingly.} \tag{5.27}$$

The χ^2-functions for each of the quantities are shown in figure 5.20. The functions are shifted such that the minimum is is zero by $\Delta\chi^2_{O,i,j} = \chi^2_{O,i,j} - \chi^2_{O,\mathrm{min.}}$. The minimum values are given in table 5.11.

The χ^2-function for the drift velocity shows a line of possible gas mixtures which fits the measured drift velocity from the top right at 3.5 % CF_4 and 2.6 % iC_4H_{10} to the bottom center at 2.6 % CF_4 and 0.8 % iC_4H_{10}. A reverse behaviour is depicted by the function for the transverse diffusion coefficient, where the line goes from the top center at 2.8 % CF_4 and 2.6 % iC_4H_{10} to the bottom right at 3.5 % CF_4 and 0.8 % iC_4H_{10}.

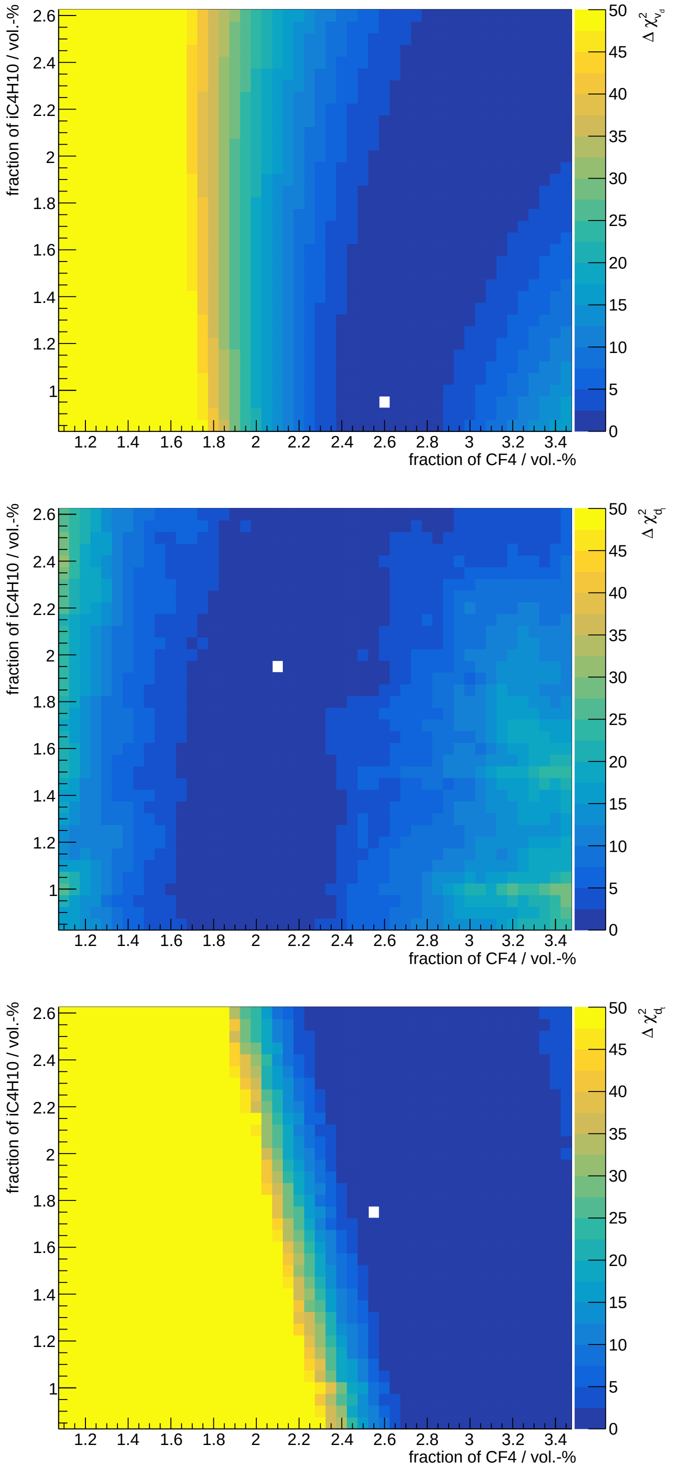

Figure 5.20.: Functions of χ^2 in dependence on the CF_4 and iC_4H_{10} fractions for the individual gas quantities. At the top the function for the drift velocity is shown, for the longitudinal diffusion coefficient in the middle and for the transverse diffusion coefficient at the bottom. The minimum χ^2-values are represented as white squares.

Table 5.11.: Minimum $\chi^2_{\text{min.}}$-values for the three gas quantities with the CF_4 and iC_4H_{10} fractions at the minimum.

	v_d	d_l	d_t
$\chi^2_{\text{min.}}$	$1.91 \cdot 10^{-5}$	$2.84 \cdot 10^{-7}$	$1.33 \cdot 10^{-6}$
CF_4	2.60 %	2.10 %	2.55 %
iC_4H_{10}	0.95 %	1.95 %	1.75 %

The χ^2-values of the drift velocity are increasing symmetrically from this line due to the symmetrical systematic uncertainty. The values for the transverse diffusion coefficient, however, increase slower to the side of higher fractions of CF_4 because of the large asymmetrical systematic uncertainty, which is much larger for lower values.
The function for the longitudinal diffusion coefficient shows the most probable gas mixtures for smaller fractions of approximately 2.0 % to 2.2 % of CF_4 while the fraction of iC_4H_{10} has less impact. The increases to both sides are approximately equal since the asymmetrical systematic uncertainties are not substantially different.
The lines of minimum χ^2-values for the transverse diffusion coefficient and the drift velocity have some overlaps, whereas the region of the longitudinal diffusion coefficient is not showing much overlap with the others.
All of the three χ^2-functions are merged together to find the most probable gas mixture. Therefore, the sum of the individual χ^2-values

$$\chi^2_{i,j} = \chi^2_{v_d,i,j} + \chi^2_{d_l,i,j} + \chi^2_{d_t,i,j} \tag{5.28}$$

is used.
The merged function is shown in figure 5.21 together with its 68.3 %- and the 95.5 %-quantiles. The most probable gas mixture is

$$95.5\,\%\ \text{Ar},\ 2.6\,\%\ CF_4\ \text{and}\ 1.9\,\%\ iC_4H_{10} \tag{5.29}$$

and has a minimum $\chi^2_{\text{min.}} = 0.00669$. The designed gas mixture with 95 % Ar, 3 % CF_4 and 2 % iC_4H_{10} lies outside of the 95.5 %-quantile.
The χ^2 is increasing faster for lower fractions of CF_4 than for higher fractions. This is caused by the χ^2-values of the transverse diffusion coefficient. This impact is larger than the preference of lower CF_4-fractions given by the individual function of the longitudinal diffusion coefficient.
The most probable gas mixtures for all individual χ^2-functions together with their 68.3 %-and 95.5 %-quantiles are shown in figure 5.22. It also shows the value with quantiles from the merged χ^2-function and the designed gas mixture.

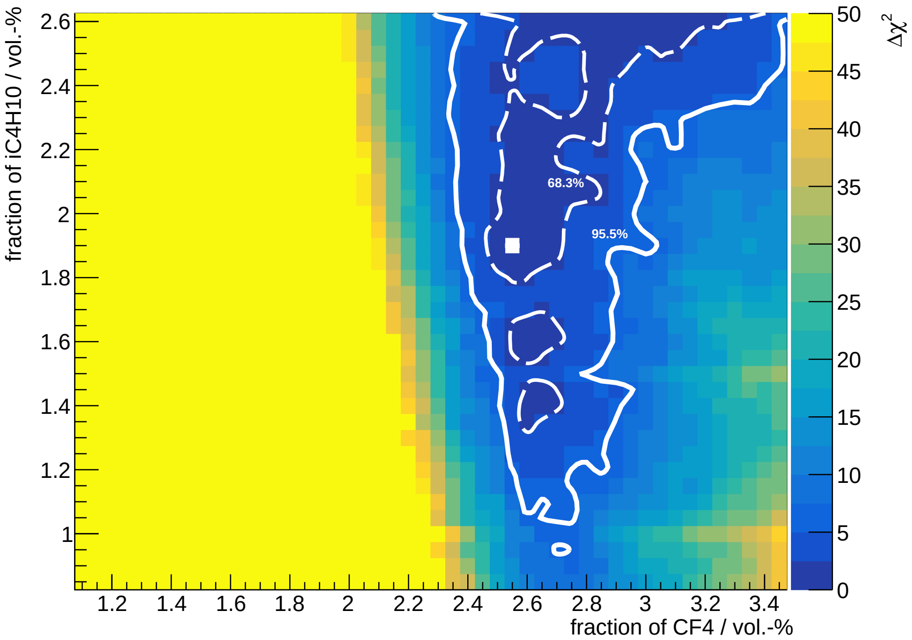

Figure 5.21.: Combined χ^2-function from the three gas quantities with 68.3 %- and 95.5 %-quantiles. The minimum χ^2-value is represented by the white square.

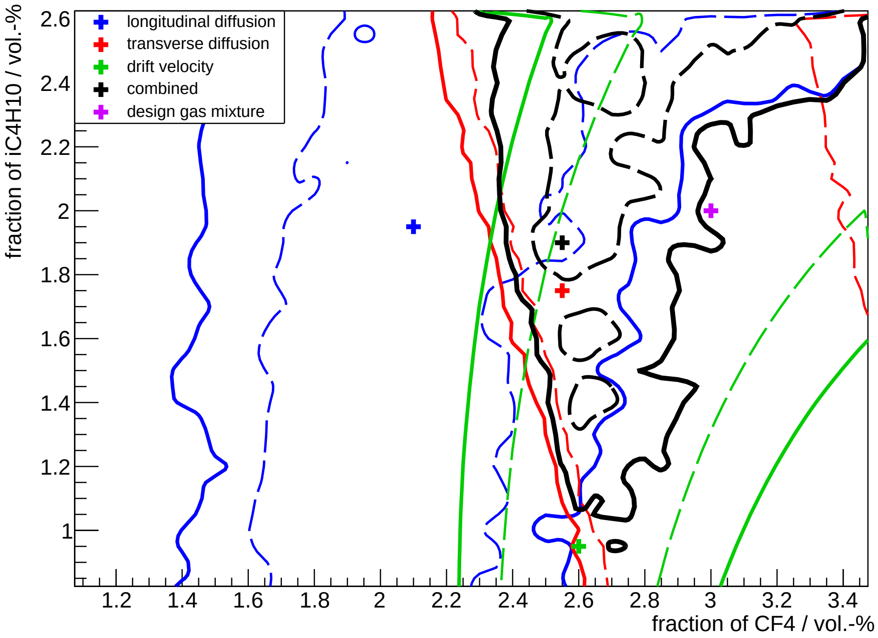

Figure 5.22.: The most probable gas mixture from each observable individually with 68.3 %-and 95.5 %-quantiles.

CHAPTER 6

Measurements with Gas Monitoring Chambers

This chapter describes the measurements of gas properties with the T2K gas monitoring chambers. These GMCs were originally built to monitor and measure the drift velocity and the relative gain. Apart from these two measurements, the possibility to measure the longitudinal and transverse diffusion coefficient in dependence on the reduced electric field ET/p is evaluated. Although the longitudinal diffusion coefficient can be determined simultaneously with the drift velocity, the original setup needs to be adjusted slightly to measure the transverse diffusion coefficient as well.
The drift velocity measurement is compared to a measurement with a new prototype GMC, which can operate at working pressures up to 10 bar.

6.1. Measurement concept for the drift velocity

To measure the drift velocity, both top side slits of the GMC are equipped with strontium-90 sources as shown in the schematic view in figure 6.1. The emitted β-electrons traverse the chambers volume from top to bottom and ionize gas molecules on their way. On the bottom of the chambers these β-electrons reach scintillating fibres. The produced light is used as start signal for a measurement.
The ionization electrons drift towards the anode along the electric field supplied in the GMC. A MicroMeGas is used as anode which provides an amplification field creating a signal that can be read out by the preshape32 amplifier [30]. This signal is recorded and serves as stop signal for the measurement.
For the signal one strip of pads is used. The pad structure is shown in figure 2.5 of chapter 2.3.2.

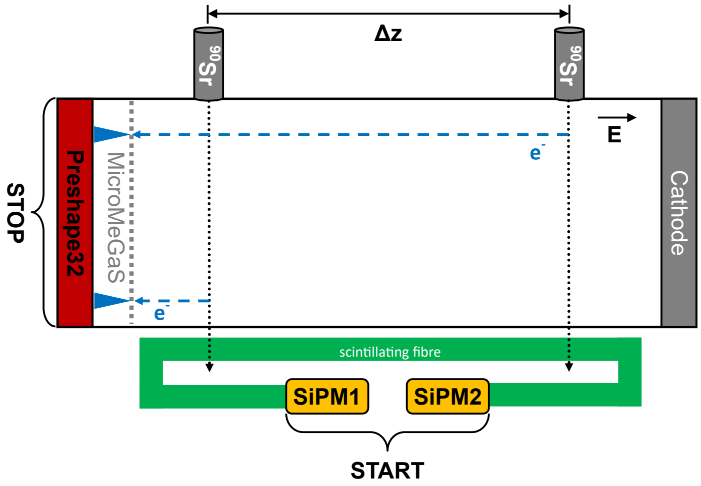

Figure 6.1.: Schematic view of the drift velocity measurement with the T2K-GMCs.

From the precisely known distance between the two slits $\Delta z = (12.10 \pm 0.01)\,\text{cm}$ and the time between the ionization and the arrival of the drifting electrons at the MicroMeGaS Δt, the drift velocity v_d is determined by

$$v_d = \frac{\Delta z}{\Delta t}. \tag{6.1}$$

Using the difference of time measurements at two positions reduces the systematic uncertainties. Timing delays and field inhomogeneities cancel out, because they are the same for both positions.

For the start signal the scintillating fibres are read out with SiPMs. A start signal is formed, if both SiPMs have a coincidence signal. Both signals are connected to a leading edge discriminator with an adjustable threshold value.

The determination of the stop time can be realized in different ways. In this thesis a method is used in which the coincidence starts the digitization of the anode signal with a flash analog-to-digital converter, FADC. These waveforms are summed up and averaged. The averaged waveform has two individual peaks for each position of the source. From these peaks the time difference Δt is determined. This averaging is performed for 1000 individual waveforms which gives a sufficient accuracy.

Another way to determine the drift velocity is to determine the time of the peak for each waveform and fill them into a histogram from which Δt can be evaluated. This method was used in [25].

Instead of sampling waveforms with the FADC it is also possible to determine the stop time with the triggerboard. This was performed in [31]. Here the anode signal is also connected to a leading edge discriminator. The time differences between start and stop are filled into a histogram from which Δt can be extracted.

6.2. Measurement concept for the longitudinal diffusion

The longitudinal diffusion coefficient is calculated from the measured widths of the signal peaks in waveforms which are recorded with the FADC. For the measurement either strontium-90 or iron-55 can be used. In case of strontium-90, it is possible to use the same data as for the drift velocity measurement. Since iron-55 is a γ source, the FADC has to be triggered by the signal itself.

To determine the width of the peak, its FWHM is used. The gaussian width σ_i in dimension of a length is then calculated from the FWHM and the drift velocity by

$$\sigma_i(s) = v_d \cdot \frac{\mathrm{FWHM(t)}}{2\sqrt{2\ln(2)}}. \tag{6.2}$$

For the measurements with strontium-90, the widths σ_l are then sorted by the time of the peak in the waveform. From this, two width distributions are gained, one for each strontium position, near and far. When using iron-55 both distributions have to be obtained by measurements with a single source at each position, respectively.

From the mean values σ_1 and σ_2 of these two distributions, the longitudinal diffusion coefficient d_l can be calculated by

$$d_l = \sqrt{\frac{\sigma_2^2 - \sigma_1^2}{\Delta z}}. \tag{6.3}$$

In this thesis the measurements are performed with strontium-90 sources. Measurements with iron-55 can be found in [32].

6.3. Measurement concept for the transverse diffusion

For measuring the transverse diffusion coefficient the method explained in chapter 4.2.2 is used. Since this method needs a monoenergetic source, iron-55 is equipped to the two top slits of the GMC.

The trigger to record waveforms with the FADC is built up from the sum of the four pad strips. For each of these strips the waveform is recorded from which the charge is extracted. As charge the height of the peak is used due to the charge integrating property of the preshape32 amplifier.

For both slits measurements have to be done separately. From the determined widths σ_i for each of the two positions, the transverse diffusion coefficient d_t is calculated using

$$d_t = \sqrt{\frac{\sigma_2^2 - \sigma_1^2}{\Delta z}}. \tag{6.4}$$

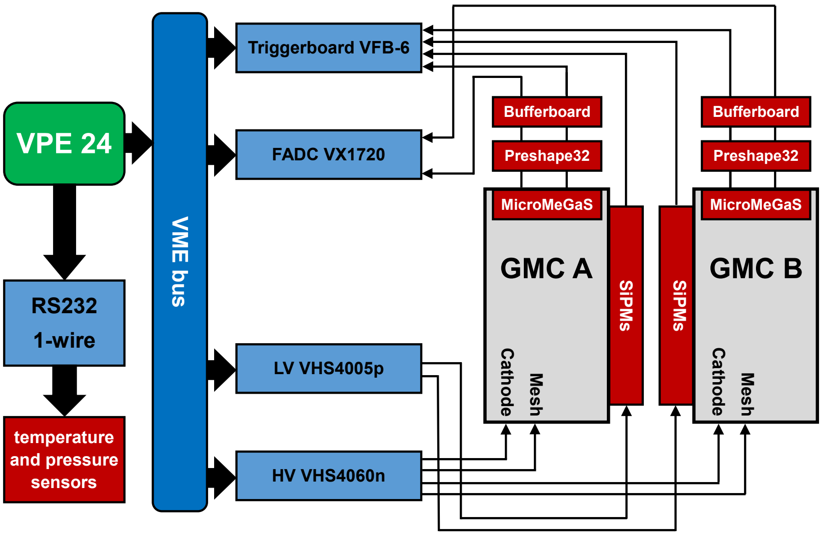

Figure 6.2.: Schematic sketch of the data acquisition of the gas monitoring chambers.

6.4. General data acquisition

The data acquisition generally used for the measurements with the gas monitoring chambers is built on a **VP E24/416-12** [33] VME-bus single board computer. It is operating the flash ADC for sampling the waveforms and the trigger board which provides the distinguished triggers for the measurements. A schematic sketch of the data acquisition is shown in figure 6.2.

As flash ADC a **CAEN VX1720** [34] with a resolution of 12 bit and a dynamic range of 2 V is utilized. The sampling rate is 250 MS/s which leads to a 4 ns time resolution.

For creating trigger signals the FPGA-based board **ELB-VME-VFB6** [35] is used which is equipped with a 16-channel discriminator. Signals can be discriminated with a 12−bit DAC in a range between −2 V and +2 V. Logical combinations of inputs can be built inside the FPGA to create the desired trigger signals which are connected to the FADC.

The VME-bus computer also controls the high voltages for the drift field and the amplification field of the MicroMeGaS with an **iSeg VHS4060n** module [36]. The bias voltages for the SiPMs are also controlled by an **iSeg VHS4005p** module [36]. Both modules can be controlled separately and in parallel to the data acquisition of the FADC.

All slow control data is determined by a 1-wire network. It consists of several temperature and pressure sensors in and around the gas monitoring chambers. These sensors are read out and logged.

Equipped with the listed parts, the system is able to run two gas monitoring chambers with alternating measurements. The system is also capable of running the measurements automatically.

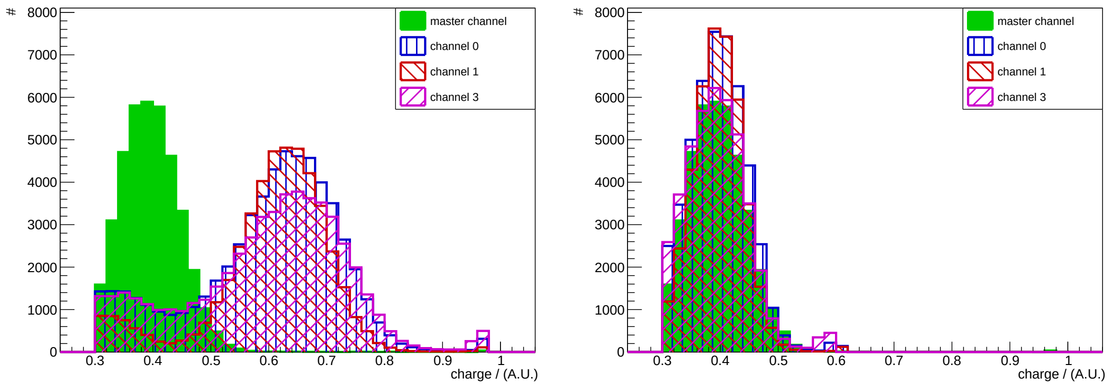

Figure 6.3.: Example for the calibration of the pad gain. On the left side the charge distributions before calibration are shown. On the right side the charge distribution after calibration shifted to the distribution of the master channel is shown.

6.5. Gas mixing

The gas mixtures, which are measured in this thesis, are mixed with the Universal Gas Mixing Apparatus, UGMA [37]. This apparatus is able to create several gas mixtures containing up to three different gas components. These mixtures have a high accuracy. The gas mixtures are mixed in parallel flow mixing mode. The precision on the fractions for a two component gas mixture is 7 % of the quencher gas. This means for example, that for a gas mixture of argon and methane with 10 % of methane, the mixture could have 10.7 % of methane instead of the requested fraction.

6.6. Preparatory measurements

This section presents studies done for the preparation of the measurements. They determine possible systematic uncertainties and effects. The results are used to calibrate the measurements of the diffusion coefficients and the drift velocity.

6.6.1. Pad gain calibration

The gains of the individual channels used for the determination of the transverse diffusion coefficient have to be aligned to reconstruct the total charge correctly. Therefore, measurements of the charge distributions are done for each individual channel with different amplification voltages supplied to the MicroMeGaS. Each measurement is triggered by its own signal, respectively, and just events with a collected charge on the considered channel of at least 90 % of the total charge of all channels are studied.
These charge distributions are then aligned by a fit. The function to minimize is the difference between the charge distribution of a master channel and of the calibration

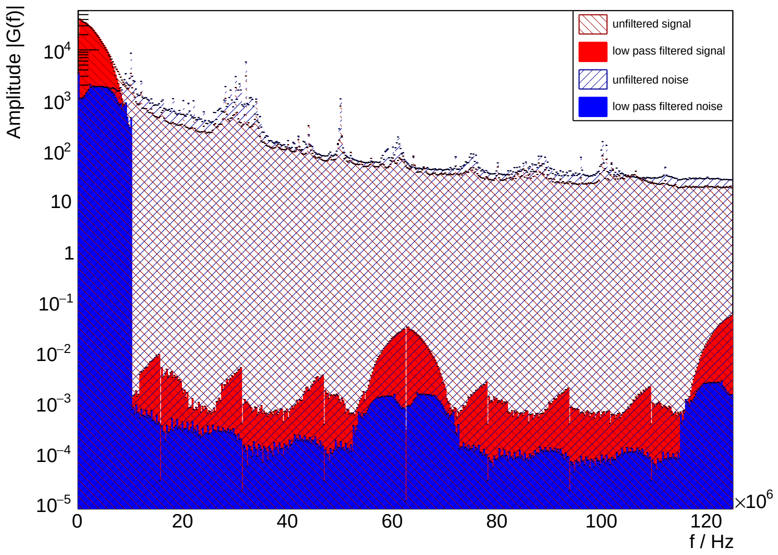

Figure 6.4.: Frequency spectra for signal and noise waveforms from discrete fourier transformation. Unfiltered spectra are depicted hatched. Solid spectra are filtered with DFT-based low pass filter. Red spectra are from signal waveforms, blue spectra from noise waveforms.

channel. This procedure is done for three of the four channels used. The fourth channel is the master channel, which is chosen arbitrarily. Figure 6.3 shows an example of this calibration. On the left side the charge distributions before calibration are shown. The means of the non-calibrated distributions are higher than of the master channel. After performing the fit and using the calibration factors, the charge distributions are all aligned as shown on the right side of figure 6.3.
This calibration is done for all measurements of the transverse diffusion coefficient.

6.6.2. Characterization of noise frequencies

The diffusion measurements are very sensitive to electric noise. This was already found in [32] for the measurement of the longitudinal diffusion coefficient with iron-55 sources. The approach there was to smooth the data with a gaussian smoothing algorithm.
Since this was too computing-intensive, a digital low pass filter based on a discrete fourier transformation is introduced to smooth the data. This filter transforms the data with a fourier transformation into the frequency domain, where the noise frequencies are removed. This applied low pass filter keeps all frequencies below a certain cutting frequency. Above this cutting frequency the data is first reduced defined by a slope and then cut out completely. The remaining data from the frequency spectrum is then transformed backwards and gives the filtered waveform.

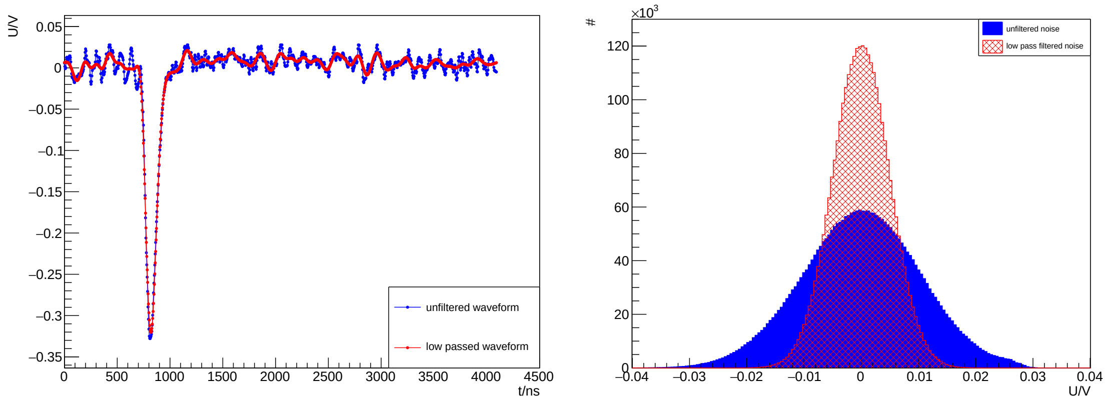

Figure 6.5.: Waveform and noise distribution for the tuning of the DFT-based low pass filter. On the left side the signal waveform with and without filtering is shown. On the right side the distribution for the noise of the baseline with and without filtering is shown.

To evaluate the cutting frequency and the slope, the signal frequencies have to be compared to the noise frequencies. Both spectra are shown in figure 6.4. The signal frequency is dominant in the region below 10 MHz visible by the red hatched spectrum. All other peaks are congruent with the frequency spectra of noise shown as blue hatched spectrum.

The low pass filter is tuned to reduce the baseline noise and optimize the signal to noise ratio. Therefore, a fit is used which tries to minimize the spread of the baseline shown in figure 6.5 on the right side. At the same time, it should minimize the influence on the signal peak of the waveform which is defined as the voltage difference between baseline value and peak minimum. A waveform is shown in figure 6.5 on the left side.

The result of the fit gives a cutting frequency of

$$f_{cut} = 5.61\,\mathrm{MHz} \tag{6.5}$$

and a slope of

$$s_{cut} = (1/4.64)\,\mathrm{MHz}^{-1}. \tag{6.6}$$

Figure 6.4 shows the cutted frequency spectra for signal and noise as solid spectra. It ought to be noticed that the mean part of the signal is kept. The still existing data in the rejected region is caused by the discrete transformation algorithm. Due to its small share it can be neglected.

From the low passed waveform it can be concluded that the peak itself is kept while the noise oscillation is widely reduced. This is shown as red curve in figure 6.5 on the left side. The reduced noise in the baseline is shown on the right side in hatched red. Since the grounding of the chambers was rearranged, it was found out that the low pass filter is not necessary anymore. Therefore, the measurements presented in this thesis were performed without this filter. Figure 6.6 shows the comparison between

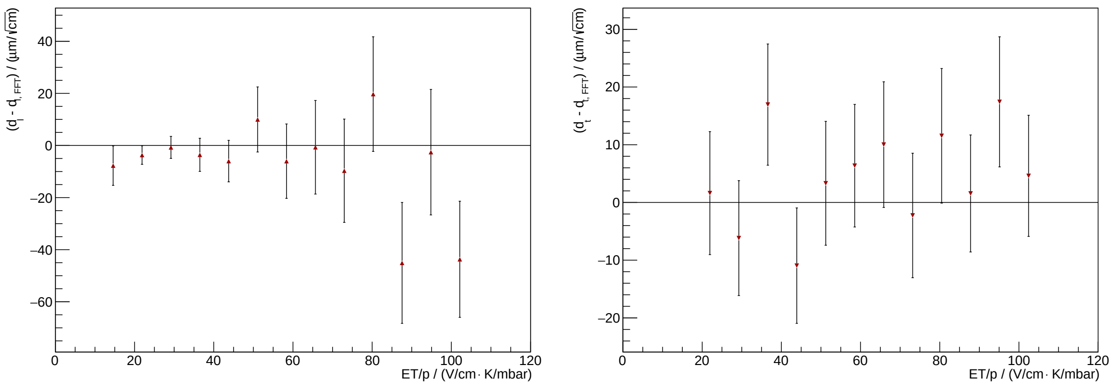

Figure 6.6.: Comparisons between measurements with and without low pass filter. On the left side comparisons for measurements of the longitudinal diffusion coefficient are shown and on the right side for the transverse diffusion coefficient.

measurements with and without the filter. On the left side the comparison for a measurement of the longitudinal diffusion coefficient is shown and on the right side for the transverse diffusion coefficient. From these comparisons it becomes apparent that the filter has no relevant impact due to the rearranged grounding of the chambers.

6.7. Measurement results

The measurements are all presented in dependence on the reduced electric field ET/p. The systematic uncertainty on ET/p is taken from [25] and is

$$\frac{\sigma_{ETp,\mathrm{sys.}}}{ET/p} = \sqrt{\left(\frac{\sigma_{U_f}}{U_f}\right)^2 + \left(\frac{\sigma_{l_f}}{l_f}\right)^2 + \left(\frac{\sigma_T}{T}\right)^2 + \left(\frac{\sigma_p}{p}\right)^2} = \pm 4\,‰. \tag{6.7}$$

It is composed of the precision of the electric field as well as the precision of the temperature and pressure measurements.
The electric field is created by a voltage U_f which is supplied to the field cage with a length l_f. The precision of the voltage was determined in [25] to result in a systematic uncertainty of

$$\frac{\sigma_{U_f}}{U_f} = \pm 0.5\,‰. \tag{6.8}$$

The length of the field cage l_f was measured with $\Delta l_f = \pm 0.5\,\mathrm{mm}$ which results in a systematic uncertainty of

$$\frac{\sigma_{l_f}}{l_f} = \frac{\Delta l_f}{l_f} = \pm 3\,‰. \tag{6.9}$$

The systematic uncertainty of the temperature measurement is estimated by the guaranteed precision of $\Delta T = \pm 0.5\,\mathrm{K}$ by the manufacturer of the sensor. Since all the mea-

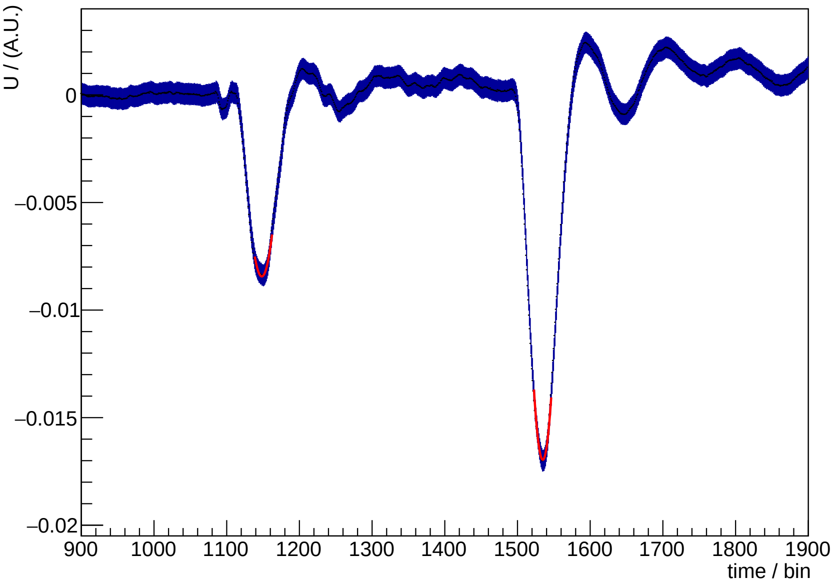

Figure 6.7.: Average waveform for the determination of the drift velocity. The data points are shown in blue, the fits to determine the position of the peaks in red.

surements were performed at room temperature the systematic uncertainty is found to be

$$\frac{\sigma_T}{T} = \pm 2\,‰. \tag{6.10}$$

According to calibrations done in [25] the pressure is measured with a precision better than $\Delta p = \pm 1\,\text{mbar}$. Measurements are performed with nominal pressure of around $p = 1000\,\text{mbar}$ which results in a systematic uncertainty of

$$\frac{\sigma_p}{p} = \pm 1\,‰. \tag{6.11}$$

6.7.1. Drift velocity

In this thesis the drift velocity is measured by the average waveform as described in section 6.1. This is the same method as used by the GMCs at the T2K experiment.

The measurement of the drift velocity collects in general 1000 of these triggers. One of these averaged waveforms is shown in figure 6.7.

Created by the two strontium-90 sources two separate peaks are occurring in the average waveform. For these two peaks the mean position μ is determined, respectively. This is done by performing parabola fits to the peaks using equation 6.12. The fits are shown in figure 6.7 as red curve.

$$U = a \cdot (x - \mu)^2 + b \tag{6.12}$$

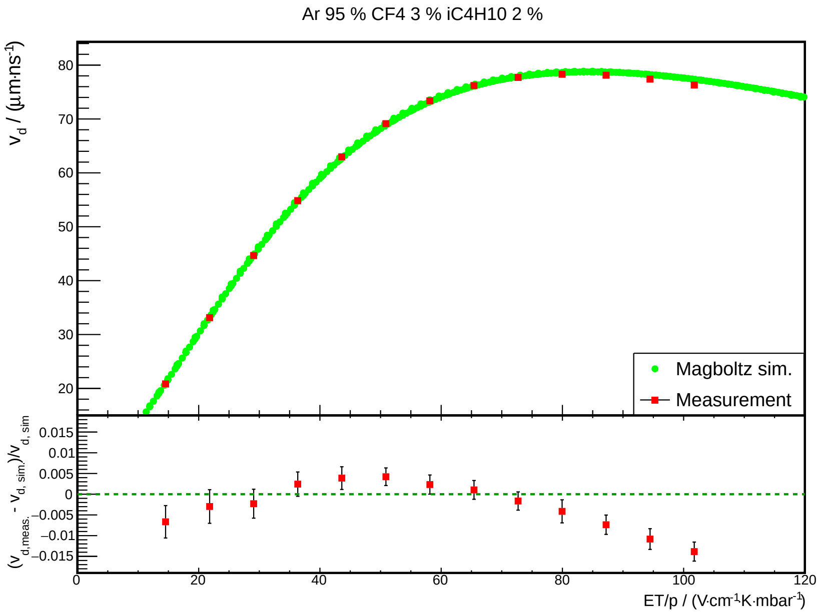

Figure 6.8.: Measurement of the drift velocity of the T2K gas mixture. Measurements for different ET/p values are shown in red, simulations in green. Simulations are shown without error bars.

The drift velocity can then be calculated by equation 6.1 with $\Delta t = \mu_2 - \mu_1$ as the difference between the two mean positions.

Measurements were performed for different gas mixtures and different electric fields. In figure 6.8 the measurements for the T2K gas mixture with Ar 95 % CF_4 3 % and iC_4H_{10} 2 % for different electric fields is shown. Since the drift velocity is not only depending on the electric field but also on the number density of electrons, the drift velocity measurements are shown as function of the reduced electric field ET/p. The data points shown for each ET/p are the weighted means of several individual measurements of 1000 triggers each.

The measurements of the T2K gas mixture are in agreement with the `MAGBOLTZ` simulation. The statistical precision of these measurements is in the order of 2 ‰. The maximum deviation between measurement and simulation is mostly lower than 1.5 %. But especially at the operating reduced field of T2K of $ET/p = 78.31\,\mathrm{V/cmK/mbar}$ the deviation is between 4 ‰ and 7 ‰.

In figure 6.9 measurements of the drift velocity for gas mixtures consisting of argon and methane are shown. These measurements show deviations up to ±3 % which is consistent with the measurements in [25].

The systematic uncertainties of the measurements are mainly taken from [25] and are in total

$$\frac{\sigma_{v_d}}{v_d} = \sqrt{\left(\frac{\sigma_{\Delta z}}{\Delta z}\right)^2 + \left(\frac{\sigma_{\Delta t}}{\Delta t}\right)^2} = \pm 4\,‰ \tag{6.13}$$

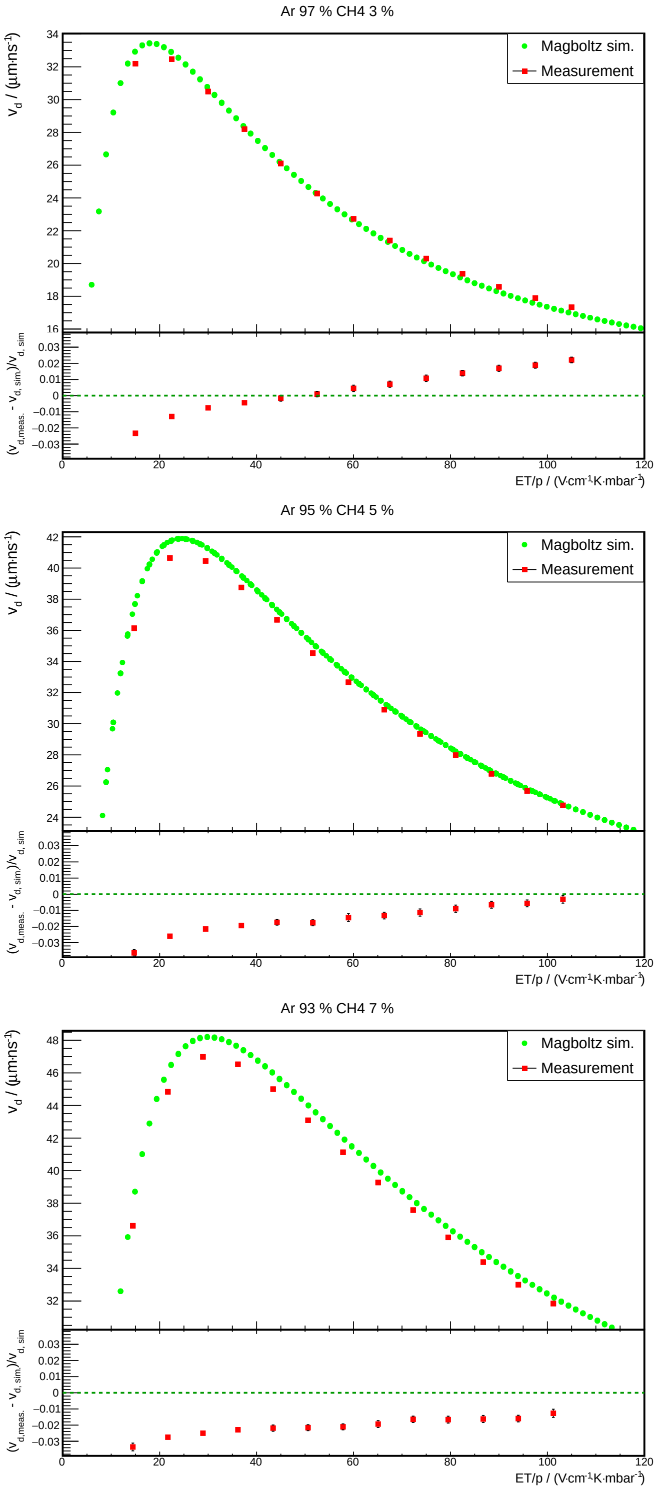

Figure 6.9.: Measurements of the drift velocity in dependence on the reduced electric field ET/p for gas mixtures of argon (Ar) and methane (CH_4). At the top measurements for the mixture Ar 97 % and CH_4 3 %, in the middle for Ar 95 % and CH_4 5 % and at the bottom for Ar 93 % and CH_4 7 %. Simulations are shown without error bars.

complemented with an additional term for the time walk of the preshape32. This time walk delays the signal. The delay, in this case, gets larger with the width of the electron cloud.

The systematic uncertainty for the drift velocity consists of the uncertainty on the drift length and the uncertainty of the time difference between the two peaks. The drift length Δz is the distance between the two slits on top of the chamber. The systematic uncertainty on this is mainly caused by the width of the slits of $\sigma_z = 1.2\,\mathrm{mm}$. This results in an uncertainty of

$$\frac{\sigma_{\Delta z}}{\Delta z} = \frac{2 \cdot 0.6\,\mathrm{mm}/\sqrt{12}}{121.0\,\mathrm{mm}} \approx 3\,‰. \tag{6.14}$$

The systematic uncertainty introduced by Δt was determined according to [25] as

$$\frac{\sigma_{\Delta t}}{\Delta t} = \pm 2\,‰ \tag{6.15}$$

by checking the time resolution with a digital signal generator. In addition to that, a contribution due to a time walk of the preshape32 amplifier is assumed. This time walk was identified in [38] and [39] and is depending on the width of the input signal. For this dependence a linear function with a slope a can be estimated. Since only time differences are used to determine the drift velocity, the offset of the linear function is not contributing to the systematic uncertainty.

The time walk creates an additional contribution to the time difference of $\delta t = a \cdot \Delta\sigma$ which reduces the measured drift velocity $v_{d,\mathrm{meas.}}$ as

$$\frac{v_{d,\mathrm{true}}}{v_{d,\mathrm{meas.}}} = 1 + \frac{\delta t}{\Delta t}. \tag{6.16}$$

The enlargement of the true drift velocity $v_{d,\mathrm{true}}$ to the measured $v_{d,\mathrm{meas.}}$ can be simplified using the definition of the longitudinal diffusion coefficient $\sigma = d_l \cdot \sqrt{z}$:

$$\frac{\delta t}{\Delta t} = \frac{a \cdot \Delta\sigma}{\Delta t} = \frac{a \cdot \frac{d_l}{v_d} \cdot (\sqrt{z_2} - \sqrt{z_1})}{\Delta t} = a \cdot d_l \cdot \frac{(\sqrt{z_2} - \sqrt{z_1})}{\Delta z}. \tag{6.17}$$

The slope can be estimated from [39, fig. 5.4] to $a = 1.25$. The total drift distances are $z_1 = 1.7101\,\mathrm{cm}$ and $z_2 = 13.8101\,\mathrm{cm}$. The uncertainty introduced by the time walk is depending on the input signal width caused by the longitudinal diffusion. A correction of this time walk is not done, because of the roughly estimated slope. In addition, the longitudinal diffusion coefficient is not measured sufficiently enough yet.

For the T2K gas mixture operating at the working point $ET/p = 78.31\,\mathrm{V/cm \cdot K/mbar}$ a diffusion coefficient of $d_l = 210\,\mu\mathrm{m}/\sqrt{\mathrm{cm}}$ can be estimated which leads to a contribution to the systematic uncertainty of

$$\frac{\sigma_{v_d,\mathrm{timewalk}}}{v_d} = +5.2\,‰. \tag{6.18}$$

The systematic uncertainty on the longitudinal diffusion measurement performed with the ND280 TPCs caused by the drift velocity is

$$\frac{\sigma_{d_l,\mathrm{ND280}}}{d_l}(v_d) = +6.6\,‰/-4\,‰. \tag{6.19}$$

In general, this systematic uncertainty needs to be evaluated for every gas mixture and ET/p value.

6.7.2. Longitudinal diffusion

The longitudinal diffusion is measured as described in section 6.2. The measurement uses the same data as the measurement of the drift velocity with strontium-90 sources. Measurements done with iron-55 sources can be found in [32].

From each individual waveform the width is determined and filled into a two-dimensional histogram with its associated peak position. A gaussian slice fit in bins of the peak position is performed around the two positions also used for the drift velocity measurement. From these fits the mean widths for the near σ_{near} and the far peak σ_{far} are determined. These widths need to be converted from a time width to a width in length. This is done by the drift velocity v_d for the certain ET/p.

The longitudinal diffusion coefficient is then calculated from

$$d_l = v_d \cdot \sqrt{\frac{\sigma^2_{\mathrm{far}} - \sigma^2_{\mathrm{near}}}{\Delta z}}. \tag{6.20}$$

The measurement is repeated for different ET/p. In figure 6.10 measurements for the T2K gas mixture are shown. The measurements follow a similar shape to the simulated curve but with an offset. In the range of an ET/p higher than 30 V/cm · K/mbar the measurements lie around 30 % below the simulations. Measurements for other gases do not show this large deviation from the simulation.

Figure 6.11 shows measurements for gas mixtures of argon with different fractions of methane (CH_4). The deviation between the measurement and the simulation are smaller than for the T2K gas mixture. Additionally, the measured diffusion coefficients are higher than the simulated coefficients. The deviation gets smaller with higher fractions of methane.

This systematic shift of the deviation from the simulations can be reduced by a proper calibration of the preshape32. For these measurements it is assumed that the dependence between the width of the incoming electron cloud is linear to the output width of the signal:

$$\sigma^2_{\mathrm{out}} \propto c \cdot \sigma^2_{\mathrm{in}}. \tag{6.21}$$

The calibration constant is chosen to be $c = 1$ as already suggested in [32]. A sufficient characterization of the preshape32 has not been performed yet and, therefore, a better calibration can not be included. An uncertainty of 10 % on the calibration

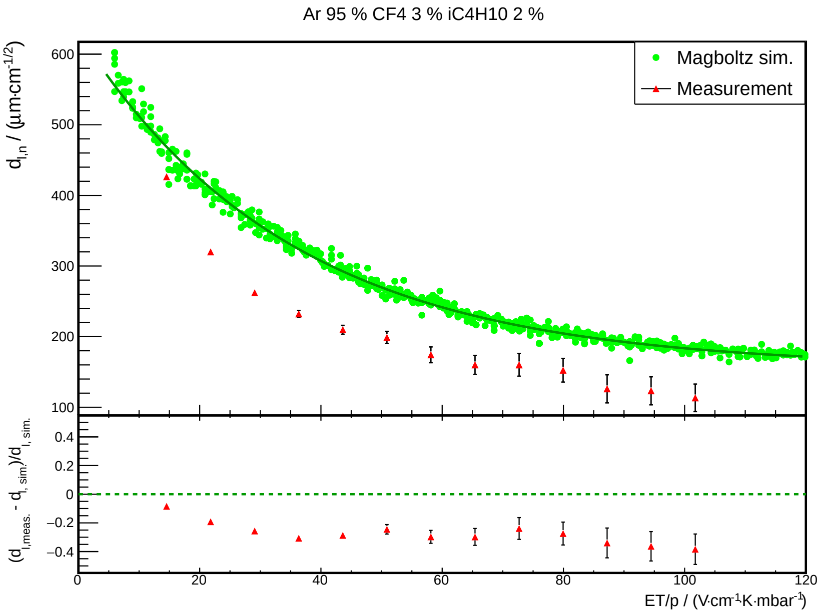

Figure 6.10.: Measurement of the longitudinal diffusion coefficients for the T2K gas mixture in dependence on the reduced electric field ET/p. Measurements are shown as red data points, the simulation as green points. Simulations are shown without error bars.

constant is taken into account to cover the variation of previous measurements with the preshape32 from [38] and [39].

The contribution to the systematic uncertainty of the longitudinal diffusion coefficients from this results in

$$\frac{\Delta d_l(c)}{d_l} = \frac{\sigma_c}{c} = 10\,\%. \tag{6.22}$$

The determination of the FWHM of a waveform is depending on the resolution of the timing of the FADC. It is assumed that the FWHM can be determined better than 0.5 bins which is 2 ns. From uncertainty propagation this results in a contribution to the systematic uncertainty of 0.5 % — 1 % depending on the FWHM itself.

The conversion of the FWHM to a width in time is done by the drift velocity measured with the GMC. The uncertainty of this measurement propagates to the systematic uncertainty of the longitudinal diffusion coefficient and is

$$\frac{\Delta d_l(v_d)}{d_l} = \frac{\Delta v_d}{v_d}. \tag{6.23}$$

The determination of the uncertainty of the drift velocity is explained in section 6.7.1. The longitudinal diffusion coefficient is also depending on the distance between the two strontium-90 sources. The contribution to the systematic uncertainty is

$$\frac{\Delta d_l(\Delta z)}{d_l} = \frac{1}{2}\frac{\sigma_{\Delta z}}{\Delta z} \approx 1.5\,‰. \tag{6.24}$$

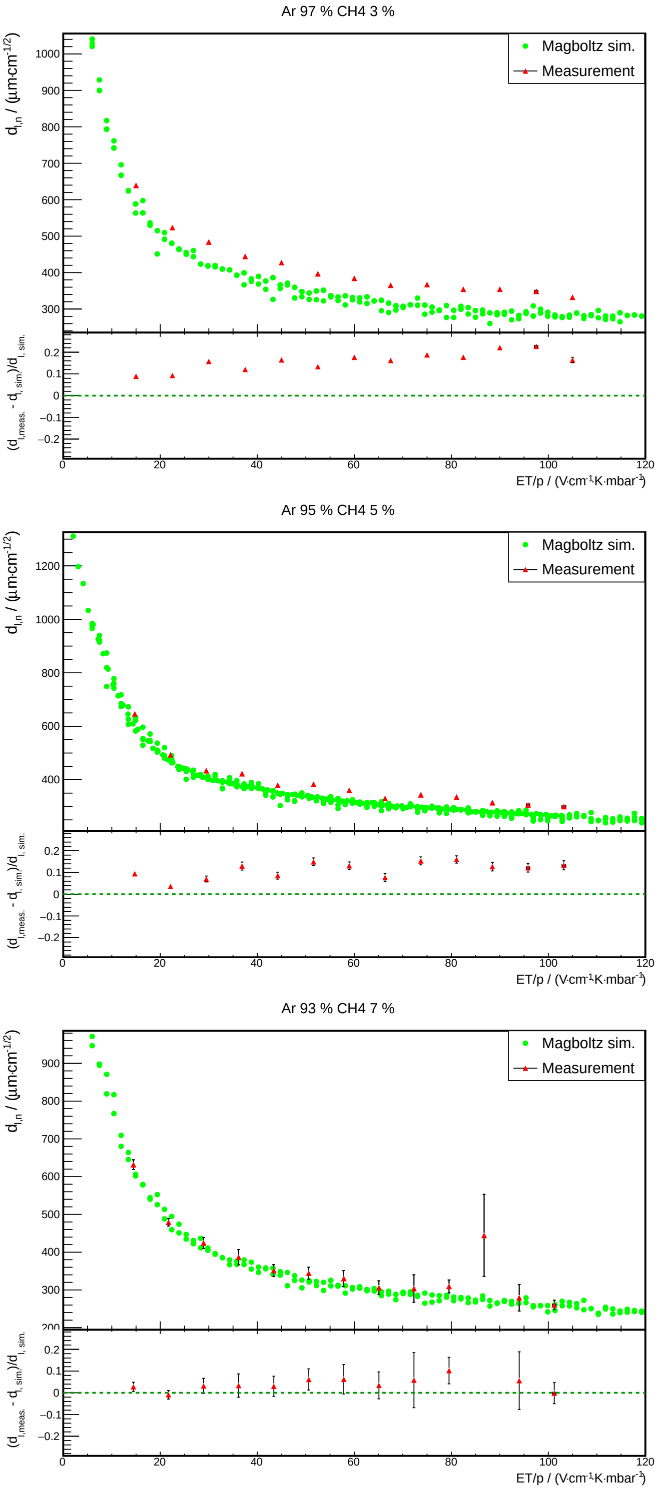

Figure 6.11.: Measurements of the longitudinal diffusion coefficients in dependence on the reduced electric field ET/p for gas mixtures of argon (Ar) and methane (CH_4). At the top measurements for the mixture Ar 97 % and CH_4 3 %, in the middle for Ar 95 % and CH_4 5 % and at the bottom for Ar 93 % and CH_4 7 %. Larger uncertainties in the measurements for the gas mixture of 7 % methane are caused by less statistics. Simulations are shown without error bars.

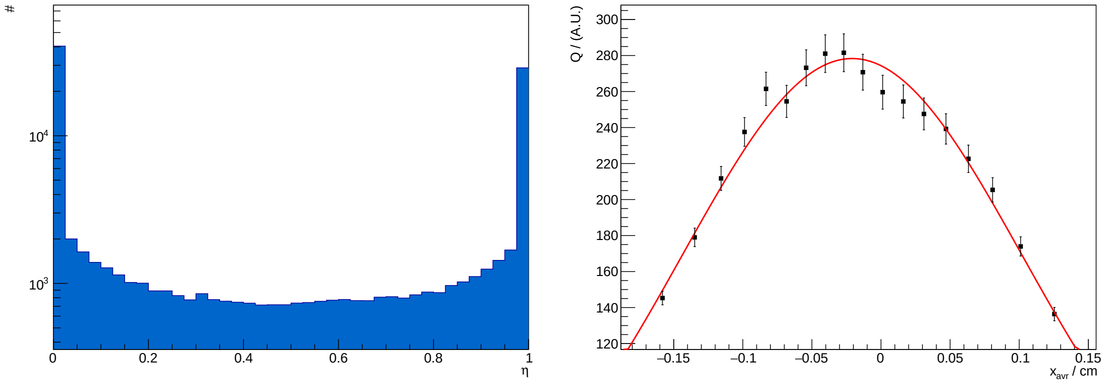

Figure 6.12.: Example for the reconstruction of a charge distribution in the measurement of the transverse diffusion coefficient. On the left side the η distribution is shown, on the right side the reconstructed charge distribution. The data is taken with the T2K gas mixture and an electric field of 275 V/cm. The distributions are from the reconstruction of the far drift distance.

6.7.3. Transverse diffusion

The measurement of the transverse diffusion coefficient is done with the adapted method from [27] as described in section 6.3. The channels are calibrated as described in 6.6.1 and all waveforms are passed through the digital low pass filter to reduce the noise of the signal as explained in 6.6.2.

The charge collected from each channel q_i is filled into a histogram for η which is defined in equation 6.25. The channels are labelled from top to bottom beginning with channel 0 as it is shown in figure 4.10. The charge in this case is the pulse height of the signal in a waveform. In figure 6.12 on the left side, an η distribution is shown as an example.

$$\eta = \frac{q_0 + q_1}{q_0 + q_1 + q_2 + q_3} \tag{6.25}$$

From these distributions the charge distribution is reconstructed according to equation 4.11 and 4.12 from chapter 4.2.2. As example a charge distribution is shown in figure 6.12 on the right side. This distribution is reconstructed from the η distribution on the left side of this figure.

The absorption length λ_γ is determined individually for each gas mixture. The single absorption lengths per energy are taken from [40]. The probability for a photon of the energy of 5.19 keV is assumed with 68.8 %, for 5.89 keV 28.0 % and for 6.49 keV 3.2 %.

$$\lambda_{\gamma,\text{gas comp.}} = \frac{1}{0.688\frac{1}{\lambda_{\gamma,5.19\,\text{keV}}} + 0.280\frac{1}{\lambda_{\gamma,5.89\,\text{keV}}} + 0.032\frac{1}{\lambda_{\gamma,6.49\,\text{keV}}}} \tag{6.26}$$

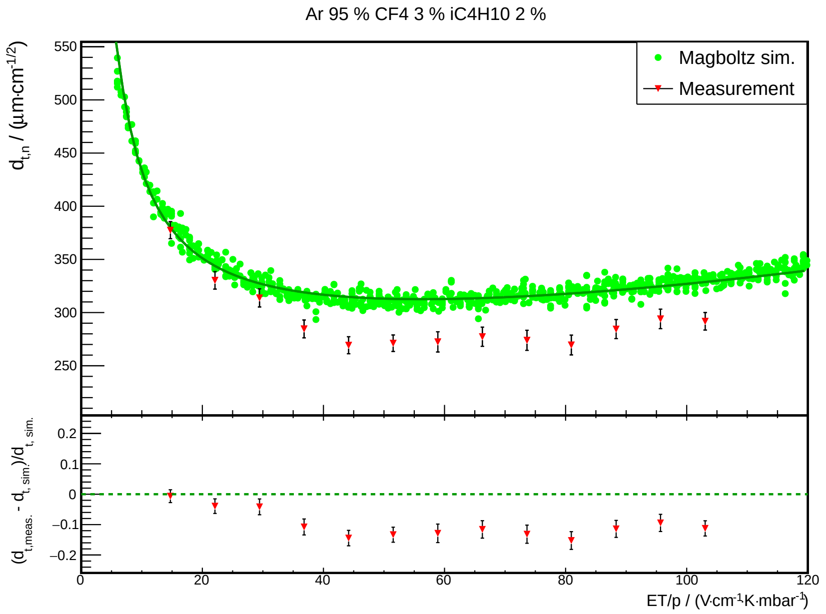

Figure 6.13.: Measurement of the transverse diffusion coefficients for the T2K gas mixture as function of the reduced electric field ET/p. Measurements are shown as red data points, the simulation as green points. Simulations are shown without error bars.

The mean absorption length for the gas mixture is then calculated from the individual mean absorption lengths of the gas mixture components by its fraction f_i:

$$\lambda_{\gamma,\text{gas mix.}} = \frac{1}{\sum_i \frac{f_i}{\lambda_{\gamma,\text{gas comp.},i}}}. \tag{6.27}$$

For the T2K gas mixture this yields an attenuation length of $\lambda_{\gamma,\text{T2K}} = 1.55\,\text{cm}$. The individual attenuation lengths for the gas components are $\lambda_{\gamma,\text{Ar}} = 1.56\,\text{cm}$ for argon, $\lambda_{\gamma,\text{CF}_4} = 5.76\,\text{cm}$ for tetraflouromethane and $\lambda_{\gamma,\text{iC}_4\text{H}_{10}} = 0.66\,\text{cm}$ for isobutane. For a gas mixture of 95 % of argon and 5 % of methane the attenuation length is $\lambda_{\gamma,\text{P5}} = 1.64\,\text{cm}$. The individual attenuation length of methane is $\lambda_{\gamma,\text{CH}_4} = 121.94\,\text{cm}$.

Measurements of the transverse diffusion coefficient in dependence on the reduced electric field ET/p for the T2K gas mixture are shown in figure 6.13. The measurements again show a deviation from the simulation in the order of $-10\,\%$ for $ET/p > 35\,\text{V/cm} \cdot \text{K/mbar}$. Below this ET/p the deviation is smaller. The measured shape resembles the shape of the simulation.

Measurements for different gas mixtures of argon and methane are shown in figure 6.14. For the gas mixtures with 5 % and 7 % of methane a deviation between the measurement and the simulation is observed. These deviations are similar to the deviation in the measurements of the longitudinal diffusion coefficient. For the measurement with 3 % of methane the simulation shows strong fluctuations and, therefore, no sufficient conclusion can be drawn from this comparison.

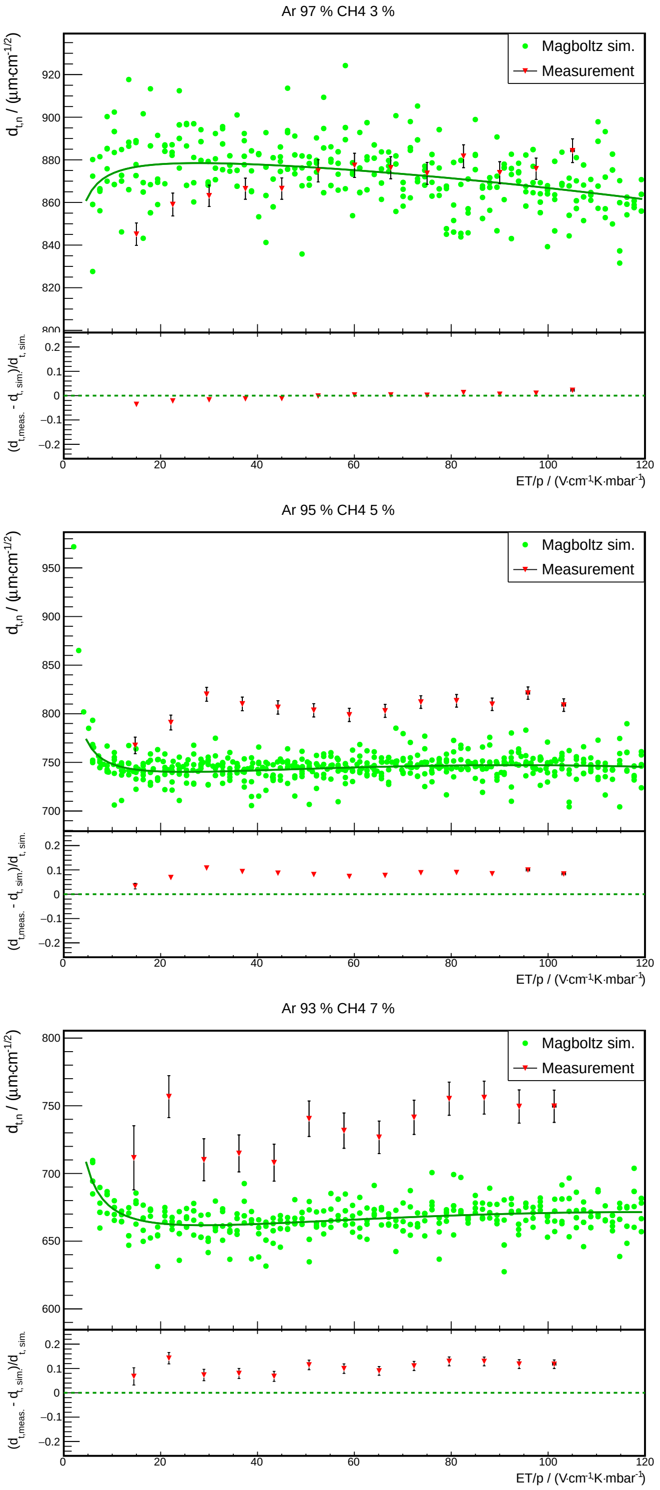

Figure 6.14.: Measurements of the transverse diffusion coefficients in dependence on the reduced electric field ET/p for gas mixtures of argon (Ar) and methane (CH_4). At the top measurements for the mixture Ar 97 % and CH_4 3 %, in the middle for Ar 95 % and CH_4 5 % and at the bottom for Ar 93 % and CH_4 7 %. Simulations are shown without error bars.

In contrast to the measurement of the longitudinal diffusion, an explanation due to systematic uncertainties is not feasible. Further discussion on these deviations can be found in section 6.7.4. The total systematic uncertainty of the measurement of the transverse diffusion coefficient is ±1 % at the maximum. This systematic uncertainty consists of different contributions explained in the following.
The absorption length is calculated for each gas mixture. Since these calculations are depending on measurements and estimations, an uncertainty of ±10 % for λ_γ is assumed. The impact of this uncertainty is determined by shifting the value of λ_γ around the uncertainty and comparing the deviation to the result without shifting. A maximum deviation of

$$\Delta d_t(\lambda_\gamma) = (+1.09/-1.63)\,\mu\text{m}/\sqrt{\text{cm}} \tag{6.28}$$

is found. For a minimum diffusion coefficient of $d_t = 300\,\mu\text{m}/\sqrt{\text{cm}}$ this adds up to a contribution of

$$\frac{\Delta d_t(\lambda_\gamma)}{d_t} \approx 5\,‰. \tag{6.29}$$

The contribution of the FADCs resolution in the measured charge is evaluated by shifting the measured charge in the analysis around the resolution in all possible combinations. The resolution of the FADC is 0.49 mV. From the variation of the charge a maximum deviation of

$$\Delta d_t(\sigma_{\text{FADC}}) = (+1.40/-1.9)\,\mu\text{m}/\sqrt{\text{cm}} \tag{6.30}$$

is found. For a minimum diffusion coefficient this results in a contribution of

$$\frac{\Delta d_t(\Delta Q_{\text{FADC}})}{d_t} \approx 6\,‰. \tag{6.31}$$

The positioning of the pads also contributes to the systematic uncertainties. These pads are built on a multilayer printed circuit board. Traces on these kind of PCBs have a tolerance of about 10 μm according to manufacturers. The positions a and b from equation 4.8 and 4.11 are shifted around the tolerance and the maximum deviation is determined as systematic uncertainty. Thus, the deviations are

$$\Delta d_t(a,b) = \pm 0.85\,\mu\text{m}/\sqrt{\text{cm}} \tag{6.32}$$

which results in a systematic uncertainty for the minimum diffusion coefficient of

$$\frac{\Delta d_t(a,b)}{d_t} \approx 3\,‰. \tag{6.33}$$

6.7.4. Discussion of the measurement results

The measurements of the drift velocity show deviations from the simulations in the order of a few percent. These deviations were already discovered in [25]. Characterizations performed in [38] and [39] show that the used amplifier preshape32 produces a time walk of the signal depending on the incoming width. The width of the signal depends on the longitudinal diffusion of the applied gas mixture. However, the consideration of this time walk in the systematic uncertainties only allows the explanation for measuring smaller drift velocities. Regarding the residuals for the gas mixture consisting of 5 % or 7 % of methane, the deviations between measurement and simulation decrease with ET/p simultaneously with the longitudinal diffusion coefficient. Although the estimated systematic uncertainty determined by equation 6.17 is too small to cover the deviations found in all measurements.

The measurement of the gas mixture with 3 % of methane shows larger drift velocities than the simulation with a deviation of up to 3 % which can not be explained by the time walk. The deviations for the T2K gas mixture are rather small in comparison to the mixtures with methane.

For a better clarification, more accurate investigations of the time walk of the preshape32 are needed. Additionally, a new amplifier could help to understand these divergences.

The measurements of the longitudinal diffusion coefficient depict similar shapes as the simulation, even though they have varying offsets for the different gas mixtures. The significance of these measurements suffers mostly from the missing calibration between the incoming and the outgoing width, which could not be sufficiently determined. This is attempted to be taken into account with a systematic uncertainty. Further investigations of the preshape32 are necessary to optimize these measurements with higher accuracy and precision. In the establishment of this measuring concept variations were discovered by using different preshape32s which hints on a series-specific functional dependence. An alternative amplifier would also help in this case to improve the measurement.

The transverse diffusion coefficient can be measured with small systematic uncertainties, even though the measurements show deviations from the simulations. The total systematic uncertainty for these measurements is estimated to be ±1 % at the maximum, but the measurements show deviations of up to 10 %. For the T2K gas mixture the measured diffusion coefficients are smaller than the simulations. For the measurements with gas mixtures consisting of argon and methane, the diffusion coefficients are larger than the simulations. Since the simulation of the gas mixture with 3 % of methane is not simulated well enough and, therefore, shows a wide spreading, the comparison with the measured data can not be used for a significant evaluation.

From the measurements of other gas mixtures the same trend of the direction of the deviation can be noted for the transverse and the longitudinal diffusion coefficient. However, they are not in the same order of magnitude. For example, the measurements for both diffusion coefficients for the T2K gas mixture lie below their simulation. For the gas mixture of argon and methane with 5 % of methane, the measurements are above the simulation for both diffusion coefficients. This leads to the conclusion that some common systematic effect causes the deviations.

The mixing of the gas mixtures has a tolerance and the designated gas mixture which is used to compare in the simulation is not exact enough. For the mixing of a two-component gas mixture this uncertainty was determined to be 7 % on the fraction of the quencher gas [37]. The impact of this, however, is not large enough to explain the divergences appearing in the measurements.

A second variation in the gas mixture is possible due to the quality of the individual gas components. The used argon has a purity of 5.2 which means that it consists of 99.9992 % of argon. The other gases have a purity of at least 3.5 which results in 99.95 % of the gas itself. For the mixture with 10 % of methane a contamination of other gases of approximately 50 ppm is possible. The simulation program `MAGBOLTZ` is only capable of simulating fractions of at least 100 ppm. The effect due to this contaminations is expected to be very small.

Other contaminations in the gas mixtures are possible caused by the outside environment. For example, water can diffuse into the gas system. For this kind of contamination, sensors are provided in the gas system for water and oxygen. These sensors never showed a higher concentration than a few ppm. Therefore, the effect of these contaminations should be negligible.

In the measurements, effects of the high electric fields in the amplification region of the MicroMeGaS are not considered. It is assumed that these effects are small and constant. Since all measurements are comparisons between the signal from a far and a near position, these effects ought to be negligible. If the effects of the high electric field are depending on the width or the total charge of a electron cloud, it would cause a contribution which is not taken into account.

The precision given by the simulations performed with `MAGBOLTZ` is very high. All used gas components are rated with five stars except for isobutane which is rated with four stars. This rating represents the reliability of the cross-section for the gas. A rating of five means a detailed and well-validated description of the gas [41]. This allows the conclusion that the simulations performed in this thesis are on a high level of precision calculated from well-measured cross-sections.

The origin of the observed deviations, therefore, needs to be understood better and the precision of the measurement has to be increased before it can compete with the simulation.

Nonetheless, the measurement concepts are working very well. Especially the results for the transverse diffusion coefficients show good results with small systematic uncertainties. Further investigations mainly on the preshape32 have to be done or an alternative amplifier has to be established.

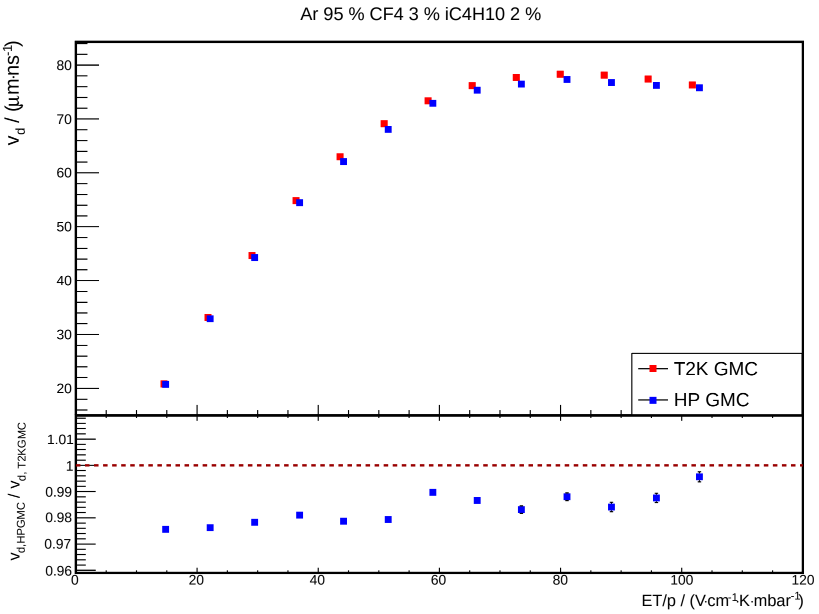

Figure 6.15.: Comparison of drift velocity measurements between the T2K GMC and the high-pressure GMC.

6.8. Measurements with the high-pressure GMC

The working group in Aachen developed a prototype for a gas monitoring chamber which can operate with 10 bar overpressure [22]. The vessel of the chamber is made from a stainless steel double-tee piping which is lined inside with perfloroalkoxy alkane, PFA, for electrical insulation. Inside the piping a field cage is located which is built from copper rings and has a length of approximately 97 mm. Drift fields of up to 3000 V/cm can be achieved. These high drift fields are necessary to measure the same ET/p ranges under high pressures than with the T2K GMCs operating at atmospheric pressure.

The high-pressure GMC has two strontium-90 sources installed with a distance of $\Delta z = 52$ mm to measure the drift velocity.

The signal amplification is realized by a single thin wire in a copper cylinder into which the ionization electrons drift when they reach the anode. The data acquisition is similar to the one used for the T2K GMC described in section 6.4. The measurement of the drift velocity uses the same concept as described in section 6.1.

Figure 6.15 shows measurements of the drift velocity for the T2K gas mixture which were performed parallel to the measurements with the T2K GMC. Additionally, the measurements with the T2K GMC and the ratio of both measurements are shown.

The measurements of the high-pressure GMC show a similar shape to the measurements of the T2K GMC. The deviation between the measurements are 3 % at the maximum. The drift velocity measured with the high-pressure GMC is constantly smaller than the measurements with the T2K GMC. This suggests that the amplifier used for the high-pressure GMC also suffers from a width depending time walk and that this effect is larger than for the preshape32. This is still under investigation.

An analysis of the longitudinal diffusion coefficient with the measured data of the high pressure GMC is not feasible by now, since the difference in the two drift lengths is too small to measure a significant change in the width from both positions with the actual readout.

Further investigations and developments of the high-pressure GMC are still in progress. It is planned to use a segmented readout in the future.

Chapter 7

Conclusions and Outlook

In this thesis measurements of gas properties are successfully performed with two different gaseous detectors.
With the TPCs of the ND280 detector suitable measurements for the longitudinal and transverse diffusion coefficients as well as the drift velocity are done, even though the TPCs were not originally built to measure these quantities. The gas properties are determined for T2K run 4, which took place between October 2012 and May 2013, due to its availability on the computing cluster in Aachen. The concepts of these analyses were tested on this T2K run and can be performed for the other T2K runs in the same way. Since the analyses need data samples including the waveforms, huge amounts of disc storage are needed. Therefore, it is recommended to perform them on GRID.
All three results are in agreement with the values determined with `MAGBOLTZ` simulations. The longitudinal diffusion coefficient is measured from the width of the electric signals. The measurement has a high accuracy and results in

$$d_l = (210.45 \pm 0.21\,(\text{stat.})\,^{+1.74}_{-1.19}\,(\text{sys.}))\,\frac{\mu\text{m}}{\sqrt{\text{cm}}}.$$

The transverse diffusion coefficient is determined from the reconstruction of the charge distribution on the pad plane. The measurement works well, but suffers from the systematic uncertainty of the determination of the y-coordinate. The transverse diffusion coefficient is measured as

$$d_t = (275.22 \pm 0.78\,(\text{stat.})^{+2.00}_{-19.30}\,(\text{sys.}))\,\frac{\mu\text{m}}{\sqrt{\text{cm}}}.$$

The drift velocity is measured by the differences in the arrival time of the signal from tracks crossing either the anode or the cathode. The result for the drift velocity is found to be

$$v_d = (78.0712 \pm 0.0004\,(\text{stat.}) \pm 1.9518\,(\text{sys.}))\,\frac{\mu\text{m}}{\text{ns}}.$$

The measurement of these gas properties can be used to improve the Monte Carlo simulation of the ND280 detector needed to perform neutrino interaction analyses in the T2K experiment.

In the future these measurement concepts can also be applied to the two new TPCs which will be installed in ND280 as upgrade for T2K-II. On the one hand, the results of these measurements can assure that the TPCs are working as expected, since the results should be in agreement with the already installed TPCs. On the other hand, by performing the measurements for each run, the input values for the Monte Carlo simulations can be controlled and adjusted if necessary.

The same gas quantities are measured with gas monitoring chambers in dependence on the reduced electric field.

For measuring the drift velocity the same measurement concept is utilized as it is used in the gas monitoring chambers operating at the ND280 detector to calibrate the TPCs. Small deviations detected between measurements and simulation can be explained by a width-depending time walk of the amplifier. Additionally, the measurement is compared to a measurement done with a prototype of a high-pressure gas monitoring chamber.

The longitudinal diffusion coefficient is again measured by the width of the electric signal. This concept was tested with iron-55 sources and can also be performed with strontium-90 sources which makes it possible to measure the longitudinal diffusion coefficient with the same data as taken for the drift velocity measurement. Further improvements for this measurement are achievable with a precisely characterized amplifier.

To measure the transverse diffusion coefficient, the concept of reconstructing the charge distribution from [27] was adapted for an exponential event distribution. This makes it possible to reconstruct the narrow charge distributions with the much larger pads of the MicroMeGaS used in the GMCs. The transverse diffusion coefficient can be measured with a systematic uncertainty of 1 % at maximum with this method.

The measurement with the gas monitoring chambers can also be used to check for environmental influenced fluctuation as it has already been done with the drift velocity at the ND280 detector. The measurement of the drift velocity there is used for the calibration of the TPCs. Changes in the diffusion coefficients can also give a hint on changes in temperature and pressure. In addition, one could determine the gas mixture fraction on a regular basis.

The measurements of the drift gas properties performed in this thesis are planned to be published in an open-access database. They can therefore help in the development of new gaseous detectors. For the design of a new gaseous detector the choice of the drift gas is of fundamental importance for the spatial resolution due to the longitudinal and transverse diffusion. An accurate knowledge of them leads to the required pad size of the readout, keeping in mind that the charge of an electron cloud should be received on several pads to improve the reconstruction. The diffusion also sets the separation between tracks and limits the shaping of the signal. Therefore, the diffusion needs to be as low as required for the specifications of the experiment.

For this purpose, the open-access database can be used to find a gas mixture which fits the requirements. On the other hand, it is possible to use the established methods from this thesis to measure gas mixtures that are not available in the database. For that, the measurement concept is flexible enough to use it in most kinds of gaseous detector with a segmented readout. When operating a new TPC, the methods used for the analysis with the TPCs of ND280 can be applied. With these measurements the drift gas properties chosen for the operation can be validated. This is particularly important when testing a prototype of a TPC.

For future projects in neutrino physics high-pressure gaseous detectors are good candidates as part of a near detector. The advantages of using high-pressure instead of atmospheric pressure are higher cross-sections for neutrino interactions while keeping the good resolution for energy loss and track reconstruction. For constructing such a high-pressure TPC, studies on drift gas properties have to be done using higher pressures. For example, it needs to be confirmed, that these properties still scale with the reduced electric field ET/p under these pressures. Equipping the high-pressure GMC, which was constructed in Aachen, with a segmented readout, it is possible to use the measurement concepts established in this thesis to perform those measurements.

For the near detector of DUNE some designs are proposed using such a high-pressure TPC. The measurement concepts of this thesis can be used to perform measurements of the drift gas properties with these TPCs. As mentioned before, these measurements can help to verify the performance of TPCs and their results can be used as input parameters for detector simulations. They can also be used to select the appropriate drift gas mixture for such high-pressure TPCs.

In summary, this thesis presents precision measurements of drift gas properties with the TPCs of the T2K near detector and with a dedicated gas monitoring chamber in the laboratory. These measurements confirm the Monte Carlo simulations used for the neutrino oscillation analysis of T2K. Furthermore, the established methods can be of use for the design, development and commissioning of TPCs in future long baseline experiments.

Appendix A

Independence of magnetic field for drift velocity and longitudinal diffusion

In case of a magnetic field which is applied parallel to the electric field the drift velocity and the longitudinal diffusion coefficient should remain the same. This is explained in chapter 2.1.5.

Simulations with `MAGBOLTZ` are performed to verify the impact of a magnetic field to the drift velocity and the longitudinal diffusion.

Figure A.1 shows the simulations for the drift velocity. The blue line shows the fit to the simulation without and the red doted line the one with magnetic field. As assumed both lines are almost identical and no relevant difference can be noticed.

In figure A.2 the simulations for the longitudinal diffusion coefficient are shown, with the blue line representing the simulation without magnetic field and the red line the simulation with magnetic field. Again no relevant differences between the simulations can be noticed since both fits have a similar result. Minor deviations are negligible and due to statistical fluctuations of the simulations.

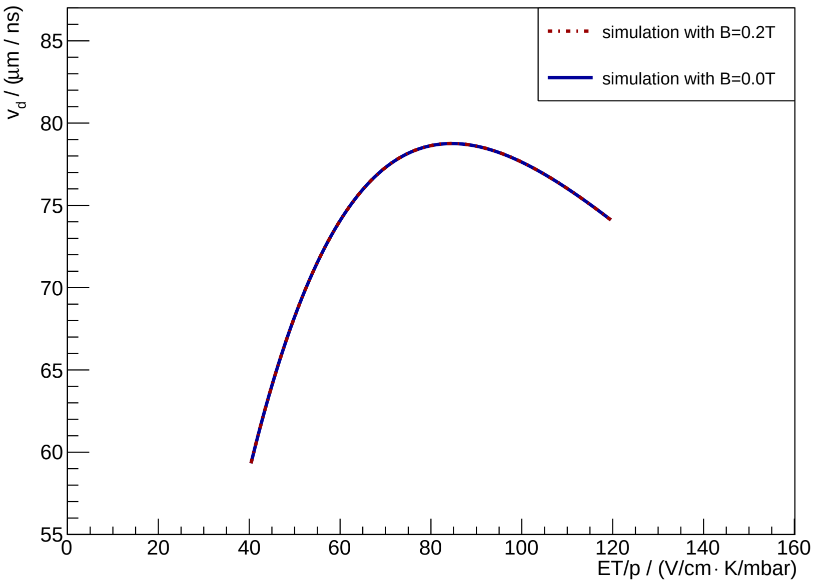

Figure A.1.: `MAGBOLTZ` simulation of the drift velocity with different magnetic fields for T2K-gas.

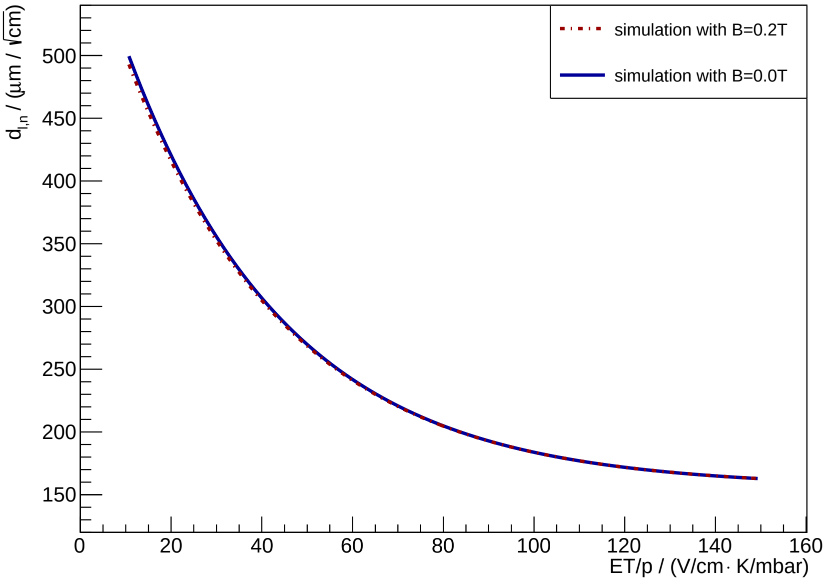

Figure A.2.: `MAGBOLTZ` simulation of the longitudinal diffusion coefficient with different magnetic fields for T2K-gas.

Appendix B

Additional to ND280 Measurements

B.1. Temperatures of single TPCS

In figure B.1 the temperature distributions of each individual TPC separated by readout plane are shown. It is visible, that the temperatures in TPC 2 are slightly higher compared to the other TPCs. This enhancement is about $\Delta T = 1\,\mathrm{K}$ and, therefore, in the order of precision of typical temperature sensors.

The shapes of the distribution all look very similar. In all of them two peaks are visible. The difference of the means again is in the order of $\Delta T = 1\,\mathrm{K}$.

The impact of 1 K to the scaling of the diffusion coefficients as depicted by equation 3.1 is less than 2 ‰ and is already taken into account by the spread of the distribution. However, an effect due to temperature fluctuations is not noticed in the analyses of the longitudinal and transverse diffusion coefficient.

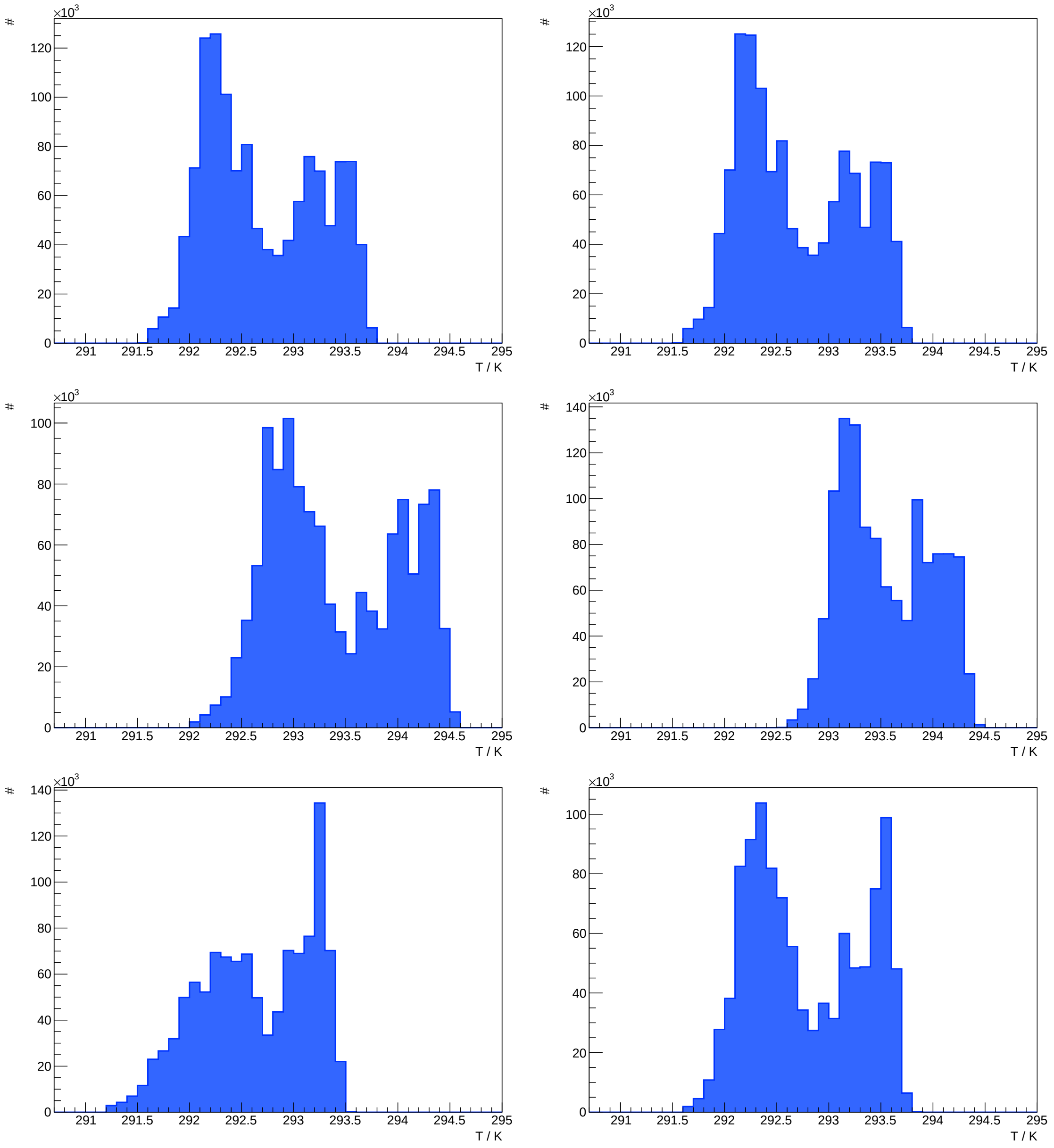

Figure B.1.: Temperature distributions for individual TPCs for the diffusion analyses in ND280. Starting from the top with TPC1, in the middle TPC2 and at the bottom TPC3. On the left side readout plane 0 is shown, on the right readout plane 1.

B.2. Longitudinal Diffusion Result without β-correction

Figure B.2 shows the result for the longitudinal diffusion coefficient without the β-correction factor measured with the TPCs of the ND280 detector.

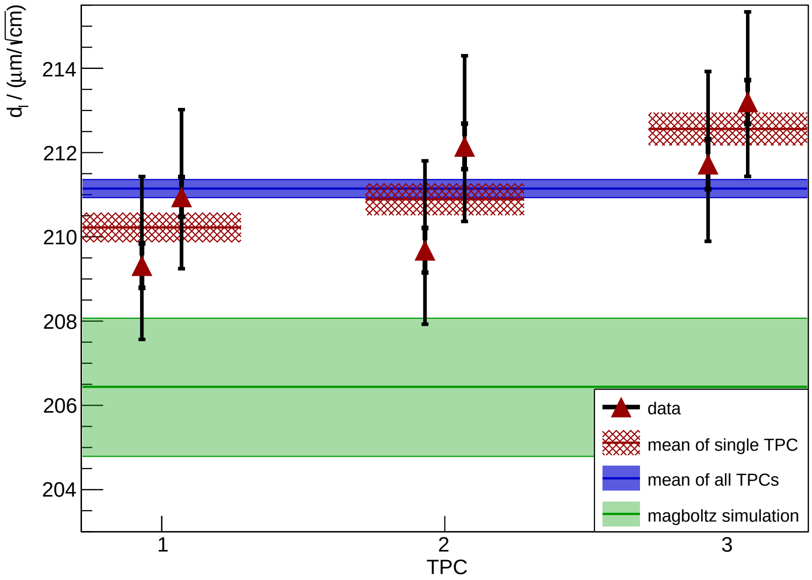

Figure B.2.: Result for the longitudinal diffusion coefficient analysed in the ND280 TPCs without applied β-correction factor.

References

---

[1] J. Beringer et al. „Review of Particle Physics“. In: *Physical Review D* 86.1 (2012). DOI: `10.1103/physrevd.86.010001`.

[2] C. Weinheimer. „KATRIN, a next generation tritium β decay experiment in search for the absolute neutrino mass scale“. In: *Progress in Particle and Nuclear Physics* 48.1 (Jan. 2002), pages 141–150. DOI: `10.1016/s0146-6410(02)00120-5`.

[3] O. Mena and S. Parke. „Unified graphical summary of neutrino mixing parameters“. In: *Physical Review D* 69.11 (June 2004). DOI: `10.1103/physrevd.69.117301`.

[4] K. Abe et al. „Combined Analysis of Neutrino and Antineutrino Oscillations at T2K“. In: *Physical Review Letters* 118.15 (Apr. 2017). DOI: `10.1103/physrevlett.118.151801`.

[5] M. G. T. Lasserre. *Double Chooz, A Search for the Neutrino Mixing Angle theta-13*. June 12, 2006. arXiv: `http://arxiv.org/abs/hep-ex/0606025v4 [hep-ex]`.

[6] K. Abe et al. „The T2K experiment“. In: *Nuclear Instruments and Methods in Physics Research Section A: Accelerators, Spectrometers, Detectors and Associated Equipment* 659.1 (Dec. 2011), pages 106–135. DOI: `10.1016/j.nima.2011.06.067`.

[7] S. Nagamiya. „Introduction to J-PARC“. In: *Progress of Theoretical and Experimental Physics* 2012.1 (2012). DOI: `10.1093/ptep/pts025`.

[8] *T2K-experiment*. 2019. URL: `http://t2k-experiment.org`.

[9] K. Abe et al. *Proposal for an Extended Run of T2K to* 20×10^{21} *POT*. Sept. 14, 2016. arXiv: `http://arxiv.org/abs/1609.04111v1 [hep-ex]`.

[10] A. Blondel, M. Yokoyama, and M. Zito. *The T2K-ND280 upgrade proposal*. Technical report CERN-SPSC-2018-001. SPSC-P-357. This proposal is the follow-up of the Expression of Interest EOI-15 submitted to SPSC in January 2017. Geneva: CERN, Jan. 2018. URL: `http://cds.cern.ch/record/2299599`.

[11] K. Abe et al. *T2K ND280 Upgrade - Technical Design Report*. Jan. 11, 2019. arXiv: `http://arxiv.org/abs/1901.03750v1 [physics.ins-det]`.

[12] *DUNE experiment*. 2019. URL: `www.dunescience.org`.

[13] W. Blum, W. Riegler, and L. Rolandi. *Particle Detection with Drift Chambers*. 2nd. Springer, 2010.

[14] Y. Giomataris et al. „MICROMEGAS: a high-granularity position-sensitive gaseous detector for high particle-flux environments“. In: *Nuclear Instruments and Methods in Physics Research Section A: Accelerators, Spectrometers, Detectors and Associated Equipment* 376.1 (June 1996), pages 29–35. DOI: 10.1016/0168-9002(96)00175-1.

[15] F. Sauli. „The gas electron multiplier (GEM): Operating principles and applications“. In: *Nuclear Instruments and Methods in Physics Research Section A: Accelerators, Spectrometers, Detectors and Associated Equipment* 805 (Jan. 2016), pages 2–24. DOI: 10.1016/j.nima.2015.07.060.

[16] Deutsches Elektron Syncrotron. *LCTPC - A Time Projection Chamber for a Future Linear Collider*. 2019. URL: https://www.lctpc.org.

[17] N. Abgrall et al. „Time projection chambers for the T2K near detectors“. In: *Nuclear Instruments and Methods in Physics Research Section A: Accelerators, Spectrometers, Detectors and Associated Equipment* 637.1 (May 2011), pages 25–46. DOI: 10.1016/j.nima.2011.02.036.

[18] P. Baron et al. „AFTER, an ASIC for the readout of the large T2K time projection chambers.“ In: *2007 IEEE Nuclear Science Symposium Conference Record*. IEEE, 2007. DOI: 10.1109/nssmic.2007.4436521.

[19] J. Steinmann. „Inbetriebnahme der Monitorkammern für die TPC des T2K-Experiments“. Diplomarbeit. III. Physikalisches Institut B, RWTH Aachen University, 2010.

[20] L. Koch. „Cross-section measurement of neutrino interactions in the TPC gas of the T2K off-axis near detector“. PhD thesis. RWTH Aachen University, 2018.

[21] C. Andreopoulos et al. *Proposal to Measure Hadron Scattering with a Gaseous High Pressure TPC for Neutrino Oscillation Measurements*. Technical report CERN-SPSC-2017-030. SPSC-P-355. Geneva: CERN, Sept. 2017. URL: http://cds.cern.ch/record/2284748.

[22] P. Hamacher-Baumann. „Design of a Gas Monitoring Chamber for High Pressure Applications“. Master’s thesis. III. Physikalisches Institut B, RWTH Aachen University, 2017.

[23] S. Biagi and R. Veenhof. *Magboltz - transport of electrons in gas mixtures*. Apr. 2013. URL: http://magboltz.web.cern.ch/magboltz/.

[24] R. Veenhof and H. Schindler. *Garfield++*. URL: http://garfieldpp.web.cern.ch/garfieldpp/.

[25] L. Koch. „Systematic measurement and simulation of drift gas properties“. Master’s thesis. III. Physikalisches Institut B, RWTH Aachen University, 2013.

[26] I. Aleshin. „Simulation der Diffusion von Elektronen in Driftkammern“. Bachelorarbeit. III. Physikalisches Institut B, RWTH Aachen University, 2017.

[27] E. Belau et al. „Charge collection in silicon strip detectors“. In: *Nuclear Instruments and Methods in Physics Research* 214.2-3 (Sept. 1983), pages 253–260. DOI: `10.1016/0167-5087(83)90591-4`.

[28] C. Andreopoulos et al. „The GENIE Neutrino Monte Carlo Generator“. In: *Nucl. Instrum. Meth. A* 614 (2010), pages 87–104. DOI: `10.1016/j.nima.2009.12.009`.

[29] A. J. L. Gaudin. „Drift Speed and Gain Measurements in the T2K Time Projection Chambers“. Master's thesis. University of Victoria, 2009.

[30] L. Jones and M. Raymond. *RD20 PreShape32 User Manual*. Version 1.1. 1995.

[31] W. Ma. „Development of an FPGA-based multi-chamber readout system for measuring drift properties of electrons in gases“. Master's thesis. III. Physikalisches Institut B, RWTH Aachen University, 2018.

[32] C. Hasler. „Messung der longitudinalen Diffusion mit den T2K-Monitorkammern“. Bachelorarbeit. III. Physikalisches Institut B, RWTH Aachen University, 2015.

[33] Concurrent Technologies Inc. *Technical Reference Manual for VP E2x/msd VME® Intel™ Atom Processor E3800 Product Family, Single or Dual PMC/XMC Sites*. Concurrent Technologies Inc. Aug. 2016.

[34] CAEN. *User Manual 3051: V1720 / VX1720*. CAEN S.pA. May 2017.

[35] Elektroniklaboratorien Bonn UG. *ELB-VME-VFB6*.

[36] iseg Spezialelektronik GmbH. *VHS Standard HV modules with Common-GND and VME Interface - Operator's Manual*. 2012.

[37] J. Steinmann. „Design, construction and commissioning of a gas-mixing-system for gaseous particle detectors“. PhD thesis. RWTH Aachen University, 2014.

[38] P. Hamacher-Baumann. „Charakterisierung von Vorverstärkern für die Auslese der T2K-Monitorkammern“. Bachelorarbeit. III. Physikalisches Institut B, RWTH Aachen University, 2015.

[39] P. Kinz. „Inbetriebnahme und Charakterisierung eines Vorverstärkers für die T2K-Monitorkammern“. Bachelorarbeit. III. Physikalisches Institut B, RWTH Aachen University, 2016.

[40] The Center for X-Ray Optics, Lawrence Berkeley National Laboratory. *X-Ray Attenuation Length*. 2019. URL: `http://henke.lbl.gov/optical_constants/atten2.html`.

[41] H. Schindler. *Garfield++ User Guide*. CERN. 2019.

List of Figures

List of Tables

Acknowledgements

An dieser Stelle möchte ich mich ganz herzlich bei all denen bedanken, die diese Arbeit möglich gemacht. Ein großes Dankeschön geht an:

- meinen Doktorvater, Prof. Dr. Stefan Roth, für die Betreuung und Begutachtung meiner Arbeit. Er ermöglichte mir die Mitarbeit im T2K Experiment und dadurch auch mehrere Reisen nach Japan. Die Arbeit an diesem Thema war für mich sehr spannend und hat mir viel Spaß gemacht. Auch die Lehraufgaben, die ich zusammen mit Stefan durchgeführt habe, waren für mich sehr interessant, auch wenn diese oft viel Arbeit bereitet haben.
- Prof. Dr. Alexander Schmidt, der sich bereit erklärt hat das Zweitgutachten meiner Arbeit zu übernehmen.
- Dr. Jochen Steinmann, der mir immer mit Rat und Tat zur Seite stand. Die Diskussionen mit ihm und seine Erklärungen waren mir stets eine große Hilfestellung. Auch seine Korrekturvorschläge an dieser Arbeit waren für mich sehr wertvoll.
- Dr. Lukas Koch, der mir gerade am Anfang meiner Arbeit den Einstieg in das Experiment erleichtert hat und mir auf meiner ersten Reise half, mich in Japan zurecht zu finden. Seine Ideen haben mich sehr unterstützt beim Aufbau meiner Analyse.
- Philip Hamacher-Baumann für die Diskussionen in Meetings und im Büro sowie das Korrekturlesen eines Teils der Arbeit.
- alle sonstigen (ehemaligen) Mitglieder unserer T2K-Arbeitsgruppe, die durch ihre Untersuchungen, diese Arbeit unterstützt haben.
- unsere mechanische Werkstatt, Dieter Jahn, Carsten Westhofen, Benjamin Walla und die Auszubildenden, für das Anfertigen neuer Teile für die Gasmonitorkammern.
- unsere elektronische Werkstatt, Wolfgang Feldhäuser und Eric Bock, für die Hilfe bei Problemen mit elektrischen Komponenten jeglicher Art.

- unser Sekretariat und unsere Verwaltung, Claudia Cüster-Weiger, Ruth Jansen, Melanie Roder und Iris Rosewick, für das Buchen von Flügen, Bestellungen, Hilfe bei Abrechungen und einfach, weil ihr für uns da seid.

- die Hallenbewohner, angeführt von Dr. Karl, für die tolle Atmosphäre und die manchmal doch so nutzvolle Ablenkung von der Arbeit. Die zahlreichen Diskussionen über die Arbeit und über diese hinaus sind eine große Bereicherung.

- alle Mitarbeiterinnen und Mitarbeiter der III. Physikalischen Institute (A+B) für das freundliche Arbeitsklima und den kollegialen Wissensaustausch.

- die T2K-Collaboration, T2K-young und vor allem die *Gaijin-Gang* für das Experiment an sich, die Meetings, das Karaoke und die Abende bei Pono-Pono.

- meinen gesamten Freundeskreis, die nicht nur für Erholung von der Arbeit sorgten, sondern auch durch zahllose Diskussion, meine Fähigkeit zu Hinterfragen und zu Argumentieren förderte.

- meine Band, *Memories on Polaroids*. Nach anstrengenden Tagen, konnten wir beim Krachmachen immer gut abschalten.

- meine Eltern und meine Geschwister mit ihren Partnern, die mich auch schon während meines gesamten Studiums unterstützt haben. Ohne euch, wäre ich nie soweit gekommen.

- meine Partnerin Christine, die mich immer unterstützt und mir täglich neuen Antrieb gibt, weiter meine Ziele zu verfolgen. Du gibst mir stehts die Kraft weiter zu machen, vor allem auf der Zielgeraden dieser Arbeit. Deine Korrekturvorschläge waren für mich eine große Hilfe.